

2013

Thermophysical properties study of graphene

Jingchao Zhang
Iowa State University

Follow this and additional works at: <https://lib.dr.iastate.edu/etd>

 Part of the [Atomic, Molecular and Optical Physics Commons](#), and the [Mechanical Engineering Commons](#)

Recommended Citation

Zhang, Jingchao, "Thermophysical properties study of graphene" (2013). *Graduate Theses and Dissertations*. 13333.
<https://lib.dr.iastate.edu/etd/13333>

This Dissertation is brought to you for free and open access by the Iowa State University Capstones, Theses and Dissertations at Iowa State University Digital Repository. It has been accepted for inclusion in Graduate Theses and Dissertations by an authorized administrator of Iowa State University Digital Repository. For more information, please contact digirep@iastate.edu.

Thermophysical properties study of graphene nanoribbons

by

Jingchao Zhang

A dissertation submitted to the graduate faculty
in partial fulfillment of the requirements for the degree of
DOCTOR OF PHILOSOPHY

Major: Mechanical Engineering

Program of Study Committee:
Xinwei Wang, Major Professor
Gap-Yong Kim
Hui Hu
Shankar Subramaniam
Ganesh Balasubramanian

Iowa State University

Ames, Iowa

2013

Copyright © Jingchao Zhang, 2013. All rights reserved.

TABLE OF CONTENTS

	Page
LIST OF FIGURES	v
ACKNOWLEDGEMENTS	xv
ABSTRACT	xvi
CHAPTER 1. Introduction	1
1.1. Extremely high thermal conductivity of graphene	1
1.2. Phonon thermal transport in graphene	2
1.3. Scope of present work.....	4
CHAPTER 2. Dynamic response of graphene to thermal impulse	5
2.1. Physics of the dynamic response	5
2.1.1. Dynamic method and mathematical model.....	7
2.1.2. Atomic potential and MD domain construction	10
2.1.3. Quantum correction.....	12
2.2. Results and Discussion	14
2.2.1. Fitting results of GNR and specific heat	14
2.2.2. Thermal transport in GNRs	17
2.2.3. Size effect on thermal conductivity.....	19
2.2.4. Ballistic and non-Fourier effect in dynamic response.....	23
CHAPTER 3. THERMAL TRANSPORT IN BENDED GRAPHENE NANORIBBONS	33
3.1. Methodology and results	33
3.1.1. Phonon energy transport in right-angle bended GNR.....	34
3.1.2. Energy separation in flat GNR.....	41
3.1.3. Phonon mode-conservation.....	44
3.1.4. Energy barrier across the bending region.....	49
3.2. Discussion	52

CHAPTER 4. PHONON ENERGY INVERSION IN GRAPHENE DURING TRANSIENT THERMAL TRANSPORT	59
4.1. Results and discussion	59
4.1.1. Phonon energy inversion after localized phonon excitation	59
4.1.2. Phonon package propagation and phonon coupling	64
4.2. Energy inversion with a static heat source	70
4.3. Energy inversion in multi-layer graphene	74
 CHAPTER 5. CO-EXISTING HEAT CURRENTS IN OPPOSITE DIRECTIONS IN GRAPHENE NANORIBBONS	 78
5.1. Basis of physical problem and modeling	79
5.2. Results and discussion	82
5.2.1. Negative apparent thermal conductivity in GNR	82
5.2.2. Comparison study in solid argon system	89
5.2.3. κ_{app} topology for graphene	93
5.2.4. Single-end bi-directional heat conduction and the length effect	97
 CHAPTER 6. THERMAL TRANSPORT ACROSS GRAPHENE-SILICON INTERFACE	 104
6.1. Methodology	105
6.1.1. Molecular dynamics simulation design	105
6.1.2. Physics of the pump-probe method	106
6.2. Results and discussion	107
6.2.1. Thermal resistance evaluation	107
6.2.2. Phonon mode energy decay and thermal rectification discussion	111
6.2.3. Effects of graphene dimension on interface energy transport	114
6.2.4. Effects of surface roughness	118
 CHAPTER 7. CONCLUSIONS AND FUTURE WORK	 124
7.1. Conclusions for dynamic response of graphene to thermal impulse	124
7.2. Conclusions for thermal transport in bended graphene nanoribbons	125
7.3. Conclusions for phonon energy inversion in graphene	126
7.4. Conclusions for co-existing heat currents in opposite directions in GNRs	127

7.5. Conclusions for thermal transport across graphene-silicon interface128

REFERENCES129

LIST OF FIGURES

	Page
<p>Figure 2.1. Schematic of experiment and MD simulation methods for PLTR. (a) A sample is suspended over two electrodes in experiment. The temperature of the two bases is kept at T_0 (RT). (b) Changes of sample temperature after pulsed laser heating. The sample temperature is T_0 at initial state, and then rises to T_1 quickly because of the induced heating by laser pulse. Cooling relaxation continues until sample's temperature reaches T_0 again. (c) Numerical principles derived from the PLTR technique. Temperature of the system is set at T_1 initially. Then one end of the GNR is kept at a low temperature (T_0) to represent the sample base contact point.</p>	7
<p>Figure 2.2. Structure of LJ walls in the x direction. The GNR is placed in the middle of upper and lower LJ walls. The distance between the wall and GNR plane is 3.35 Å.</p>	10
<p>Figure 2.3. Global fitting results of different lengths GNRs at 692.3 K. The lengths of GNRs from top to bottom are 14.9 nm, 29.6 nm, 59.4 nm, 124.6 nm, 249.6 nm, and 499.6 nm.</p>	15
<p>Figure 2.4. Spatial temperature evolution in GNRs at different times. The solid squares stand for MD simulation results and the curves represent theoretical results derived from diffusive heat conduction equation. The GNR length is 14.9 nm, 59.4 nm, and 499.6 nm for figures (a), (b), and (c), respectively.</p>	18

- Figure 2.5. Thermal diffusivity (α) and thermal conductivity (k) variation against the GNR length.....20
- Figure 2.6. Comparison of non-Fourier fitting and diffusive fitting to MD data. MD results are above diffusive fitting curve in the first 6 ps due to a decreased effective thermal conductivity induced by the non-Fourier effect. The non-Fourier fitting curve matches MD results soundly by using two relaxation times τ_q and τ_θ25
- Figure 2.7. Spatiotemporal isotherms of 14.9 nm GNR with a cooling area located at the lower boundary. (a) MD results, (b) numerical results calculated from Fourier diffusive heat conduction equation. The initial system temperatures for both cases are 700 K, and then a cooling impulse of 200 K is added below the origin area.27
- Figure 2.8. Spatiotemporal isotherms of 14.9 nm GNR with a thermal impulse imposed at the lower boundary for 0.4 ps: (a) overall temperature, (b) temperature of transverse phonons, (c) temperature of longitudinal phonons, (d) temperature of flexural phonons. Solid lines represent thermal wave front.28
- Figure 2.9. Phonon dispersion relations of graphene based on *ab initio* calculation [58]. The three phonon dispersion branches, which originate from the Γ point of the first Brillouin zone, correspond to acoustic modes and the rest three branches are for optical modes. The regions that correspond to different group velocities in Fig. 2.8 are denoted by dashed lines. (with permission from Elsevier for use in this paper).....31
- Figure 3.1. Thermal transport in a $2.0 \times 25.0 \text{ nm}^2$ right-angle bended GNR system. The E_y and E_z exchange their values upon crossing the bending structure, indicating

phonon mode-conservation in GNR systems. Bending resistance is observed around the bending area. Thermal conductivities of two flat GNR regions are calculated by linear fitting. The calculated κ and R values denoted in Fig. 3.1(b) are before quantum corrections.	35
Figure 3.2. Nominal temperature distributions in different length 50.1 nm, 75.0 nm and 100.0 nm right-angle GNR systems. Each GNR structure has a fixed width of 2.0 nm. The bending resistance values denoted in the figures are without quantum corrections.	39
Figure 3.3. Atomic structure of the flat GNR system studied for energy separation. The Lennard-Johns (LJ) potential walls are applied in all dimensions. To make a clear schematic description, only the top and bottom LJ walls are shown. Distance between each LJ wall and the GNR plane is set as 3.5 Å initially. A thermal energy of 5.9×10^{-8} W is added/subtracted from the red and yellow areas respectively.	42
Figure 3.4. Nominal temperature distributions in flat GNR systems of different length (a) 25.0 nm, (b) 50.1 nm, (c) 75.0 nm and (d) 100.0 nm. Each GNR structure has a fixed width of 2.0 nm. A thermal energy of the same value 5.9×10^{-8} W is added/subtracted in the selected regions for all systems. It is observed that energy separation happens at short distances in the heat flux flow direction and disappears at around 50 nm. (e) A schematic explanation of the thermal transport mechanism in short GNRs. The ZM branch has higher thermal transport ability than the in-plane TM and LM branches. Therefore E_z is lower than the E_x and E_y and the latter will keep transferring energies to E_z until they reach the same level.	44

- Figure 3.5. Spatio-temporal iso-energy contours for the right-angle GNR structure. (a) and (b) represent E_y and E_z evolution after the LM phonon excitation (E_y) at the left end. (c) and (d) are for E_z and E_y evolution after the ZM phonon excitation (E_z) at the left end. Phonon mode-conservation is observed for the LM and ZM phonon branches. Phonon package reflections are also observed in the middle-plane at the bending region.47
- Figure 3.6. Radial distribution function (RDF) of the flat and bending areas in the $2.0 \times 50.1 \text{ nm}^2$ right-angle bended GNR system. The black and red lines represent the RDF at the bending area and flat area. The RDF for the bending area shows a smaller atomic distance than that in the flat area, indicating a compressive strain in the bending structure.49
- Figure 3.7. Nominal temperature distributions for the 135° bended GNR with dimensions of $2.0 \times 50.1 \text{ nm}^2$. Atomic structure of the system is shown in the inset. Energy separation is observed in this structure, yet no obvious bending resistance or energy jump has been found.52
- Figure 3.8. Thermal resistance and thermal conductivity comparison with ε and σ reduced to half separately. It is observed that when σ is reduced to half, the R values are suppressed to zero for the 25.0 nm, 50.1 nm and 75.0 nm cases. While when ε is reduced to half, the R values just change slightly. The thermal conductivities vary in a small range when different ε or σ are used and increase with the GNR length. All the results are without quantum corrections.55

Figure 4.1. Atomic configuration and energy inversion characterization in the 2.0×25.0 ($x \times y$) nm^2 GNR system. (a) Periodic boundary condition is applied to the y direction and free boundary conditions are applied to the x and z directions. The two outermost layers of atoms in the x direction (marked as pink) are grouped to apply the stretching force ($F = 1.0 \text{ eV/\AA}$). This coordinate system is used for all the discussions in this work. (b) The $E_{k,x}$, $E_{k,y}$ and $E_{k,z}$ profiles of the GNR after 25 fs phonon excitation at the boundary. (c) The $E_{k,x}$ and $E_{k,z}$ energy exchange after the GNR is stretched in the width direction. The red area represents phonon package propagations induced by the stretch.61

Figure 4.2. Phonon package propagations in the width direction of the 2.0×25.0 ($x \times y$) nm^2 GNR system. (a), (b) and (c) are for the spatial-energy contours of $E_{k,x}$, $E_{k,y}$ and $E_{k,z}$ respectively.....64

Figure 4.3. Calculation of phonon coupling time against energy. (a) Energy evolutions after $E_{k,x}$ is rescaled to $\sim 200 \text{ K}$. (b) The characteristic coupling time of the in-plane phonons and the flexural phonons at different energy levels. It is conclusive G_z increases with the local energy level, meaning if the phonon is more excited, the mode-wide coupling will be stronger.....66

Figure 4.4. Energy inversion characterization in the GNR system with phonon package excitation in the y direction. Periodic boundary condition is applied to the x direction and free boundary conditions are applied to the y and z directions. Two outermost layers of carbon atoms at the right end (marked as yellow) are grouped to apply stretching force ($F = 5.0 \text{ eV/\AA}$). An energy bump is observed in the $E_{k,y}$

profile, which is induced by the phonon package reflection on the graphene boundary.70

Figure 4.5. Energy inversion characterization with static heating source. Fix boundary condition is applied to the y direction and free boundary conditions are applied to the x and z directions. (a), (b) and (c) show energy evolutions of the whole region, regions A, and region B. (d) Schematic to show the phonon transport in the 2.0×125.1 ($x \times y$) nm^2 GNR. Heat conduction (HC) among FM phonons is much faster than those among LM and TM phonons. The red area (region B) is the 25.0 nm heating region where $E_{k,x}$ and $E_{k,y}$ transfer to $E_{k,z}$. The thermal energies will mainly be transported by $E_{k,z}$ to the low energy area (region A) where $E_{k,z}$ mostly transfers to itself in space (heat conduction) and partially to $E_{k,x}$ and $E_{k,y}$71

Figure 4.6. Damping energy inversion against growing layers. (a), (b), (c) and (d) show energy evolutions for graphene with different layer numbers. The black, red and green solid lines represent $E_{k,x}$, $E_{k,y}$ and $E_{k,z}$ respectively. (e) $\Delta E_k / \Delta E_{k,rise}$ with different layer numbers from 1 to 10. Definitions of ΔE_k and $\Delta E_{k,rise}$ are illustrated in Fig. 4.1(b).75

Figure 5.1. Atomic configuration for studying the bi-directional heat conduction in graphene nanoribbons. The outermost layer of carbon atoms at each end (denoted in black) are fixed in position. (a) Kinetic energy is added to the FM phonons on the left side (red region) and subtracted from the right side (blue region). Heat current q''_{FM} is carried by FM phonons from left to right. (b) The in-plane longitudinal and transverse phonons are heated and cooled on the right and left sides respectively.

Heat current q''_{TM+FM} is carried by TM/LM phonons from right to left. (c) By doing (a) and (b) simultaneously, a peculiar bi-directional heat conduction phenomenon in GNR is created.80

Figure 5.2. (a), (b), (c) Nominal temperature distributions for $\mu = 1.11$. q''_{total} follows the E_T increasing direction, indicating an apparent negative κ_{app} . (d), (e), (f) Nominal temperature distributions for $\mu = 0.75$. In this case, q''_{total} follows the E_T decreasing direction, and a positive κ_{app} is calculated.84

Figure 5.3. Atomic velocity distributions for individual phonon mode in the $2.0 \times 50.1 \text{ nm}^2$ GNR system at 12.5 nm location for $\mu=1.11$. Sound agreements between the MD simulation and Maxwellian velocity distribution are observed.88

Figure 5.4. Nominal temperature distributions under steady state bi-directional heat conduction in the solid argon system. (a) The net heat flux is $1.60 \times 10^8 \text{ W/m}^2$ from right to left. The thermal conductivity κ_1 is calculated at 0.637 W/m-K. The inset shows that the mode-wide energy separation only exists within the first 1 nm of the system and the bi-directional heat conduction does not penetrate deep to the system (b) No temperature gradient is observed when the net heat flux is zero. Atomic structure of the solid argon system is shown in the inset. The outermost layer of argon atoms at each end (denoted in black) are fixed and free boundary conditions are applied to the x and z directions. Then four layers of argon atoms at each end (denoted in red and blue) are grouped to add/subtract energy. (c) The net heat flux is $1.28 \times 10^8 \text{ W/m}^2$ from left to right and thermal conductivity κ_2 is calculated at 0.677 W/m-K, which is consistent with κ_191

- Figure 5.5. Atomic velocity distributions under steady state bi-directional heat conduction in solid argon system. Different locations at 12.5 nm, 25.0 nm 37.5 nm are used in the calculation and the MD results agree well with the Maxwellian distribution.....92
- Figure 5.6. Apparent thermal conductivity (κ_{app}) topology for the $2.0 \times 50.1 \text{ nm}^2$ GNR system. The upper x -axis represents the net heat flux in the GNR system and the lower x -axis stand for the corresponding μ values. Negative κ_{app} is observed when μ is within the range of 1.05-1.38.....94
- Figure 5.7. (a), (b) When the in-plane LM/TM phonon heat conduction is dominant ($\mu < 1$), an energy overlap is observed among different phonon modes. The length of the overlap region decreases with increasing μ . (c), (d) When the flexural phonon thermal transport is dominant ($\mu > 1$), there is no energy overlap among different phonon modes and the mode-wide energy separation increases with μ96
- Figure 5.8. Nominal temperature distributions for the bi-directional heat transfer in GNR and solid argon with one-end heating/cooling. The net heat flux equals zero for both cases. For the GNR system, the nominal temperature gradient is 0.0232 K/m, which indicates an apparent zero value κ_{app} according to Fourier's law of heat conduction. While for the solid argon system at temperature 20 K, the temperature gradient is calculated at zero.98
- Figure 5.9. Dispersion relations for the $2.0 \times 50.1 \text{ nm}^2$ GNR system. (a), (b), (c) represent transverse, longitudinal and flexural modes phonon, respectively.100
- Figure 5.10. Mean free path of TA, LA and ZA mode phonons in k -space.....102

Figure 6.1. (a) Atomic configuration of the GNR and silicon system. Periodic boundary conditions are applied to the x and y directions and free boundary condition to the z direction. A thermal impulse q_{in} is imposed on the supported GNR after thermal equilibrium calculation and the top three layers of silicon atoms are grouped to calculate the surface temperature of the silicon substrate. (b) Temperature evolutions (left y axis) of GNR and Si for 50 fs pulsed thermal excitation and 150 ps thermal relaxation. The overall energy and fitting for the supported GNR system are shown in the right y axis. The calculated thermal resistance from this overall fitting method equals $3.72 \times 10^{-8} \text{ K}\cdot\text{m}^2/\text{W}$. The fitting profile calculated from a single R value soundly matches the MD simulation results...108

Figure 6.2. Comparisons of the overall fitting result and instant R calculation results. Size of the GNR is $4.1 \times 18.3 \text{ nm}^2$ ($x \times y$). By integrating the temperature differences between T_{GNR} and T_{Si} , the energy relaxation profile of GNR can be correlated to $\Delta T dt$ directly and slope of the profile can be linearly fitted to calculate the segment interfacial thermal resistance values, which is around the overall fitting results.....110

Figure 6.3. Phonon energy evolutions in the supported GNR system. It is observed that E_z decreases faster than E_x and E_y in the early stage, indicating a much stronger exchange between kinetic and potential energies for ZA phonons in graphene than the LA and TA phonons.112

Figure 6.4. Effect of graphene dimension on the interfacial thermal resistance between GNR and Si. (a) When the length of the supported GNR becomes longer,

the interfacial thermal resistance becomes larger due to the reduced edge. (b) Square shaped GNR has larger thermal resistance values than the rectangle shaped GNR ones.	115
Figure 6.5. Interfacial thermal resistance variations with surface roughness. Atomic configuration is depicted in the insets for the case of $\delta=2.0$ nm.	119
Figure 6.6. (a) Interatomic forces between supported GNR and $\delta = 0.54$ nm dented silicon substrate. The blue and red shaded areas indicate the supported and suspended GNR regions respectively. (b) Radial distribution functions for the supported GNRs. The peaks are sharper for the dented Si cases, indicating stretching forces in graphene. (c) Radial distribution functions between graphene and Si-substrate. The $g(r)$ values drop to significant lower levels when the groove depth δ becomes larger than 0.81 nm, which explains the thermal resistance increase observed in Fig. 6.5.	122

ACKNOWLEDGEMENTS

I would like to show my deepest appreciations and gratefulness to my major professor, Prof. Xinwei Wang. This work could not be accomplished without his guidance and help. Professor Wang teaches me to be dedicated to our work, to have a positive attitude towards life and above all, to stay in love with our family and friends.

In addition, I would also like to thank my research committee members, Prof. Hui Hu, Prof. Gap-Yong Kim, Prof. Shankar Subramaniam and Prof. Ganesh Balasubramanian, for their guidance and suggestions. I thank Dr. Xiaopeng Huang, Prof. Yanan Yue for their useful discussions.

Also, I would like to thank my parents for their great love and support. I would like to offer my appreciation to my friends and colleagues who have made my life so colorful.

Support of this work from Office of Naval Research (N000141210603), the Army Research Office (W911NF1010381) and the National Science Foundation (CBET-0931290, CBET-0932573, CMMI-1029072, and CMMI-0926704) is gratefully acknowledged.

ABSTRACT

Graphene is a two-dimensional (2D) material that exhibits exceptional electric and optical properties. The high electron mobility and thermal conductivity of graphene are of great interest for interconnects, electronic devices and radio frequency devices. In spite of the extensive experimental and theoretical studies on single layer graphene (SLG), its thermal properties have not yet been fully addressed and vast work need to be done to reveal the phonon transport mechanism within this micro/nanoscale material.

A transient molecular dynamics technique is developed to characterize the thermophysical properties of two-dimensional graphene nanoribbons (GNRs). By directly tracking the thermal relaxation history of GNR that is heated by a thermal impulse, we are able to determine its thermal diffusivity fast and accurate. In the right-angle bended GNR system, three peculiar features about the phonon energy transport have been observed for the first time. An energy inversion phenomenon has been observed during the transient thermal transport in GNR system. Phonon energy coupling among different phonon modes are investigated and it is found that both dynamic and static heat sources can evoke the energy inversion in GNR. The unique thermal properties of GNR enable it to support a bi-directional heat transfer in the system. And when the bi-directional heat conduction reaches steady state, a single thermal conductivity cannot be used to reflect the relation between the heat flux and the temperature gradient. The calculated thermal conductivities are dependent on the net

heat fluxes and the κ_{app} of graphene are calculated at positive, negative, zero and infinite values, depending on the proportions of each phonon mode energy added/subtracted to/from the heating/cooling areas. The dynamic response of graphene to a thermal impulse is investigated and the interfacial thermal resistance between graphene and Si is evaluated. A transient pump-probe method is designed for interfacial thermal resistance characterization.

CHAPTER 1. INTRODUCTION

1.1. Extremely high thermal conductivity of graphene

Graphene is a monolayer of graphite arranged in a honeycomb lattice of sp^2 bonded carbon atoms [1] and it has attracted much attention due to its extraordinary electronic and thermal properties [2-5] over the past decade. Graphene nanoribbon (GNR), which is a narrow strip (typically < 20 nm) of graphene, also becomes the subject of significant research because of extraordinary electrical, thermal, and mechanical properties with significant application potential in future nanoelectronic and mechanical devices. The distinguished properties of GNRs have been extensively studied both theoretically and experimentally [2, 6-9], which indicate that GNRs are a promising material for nanoelectronic applications. Owing to the edge effect and quantum confinement, GNRs are expected to exhibit outstanding thermal properties [10].

Both experimental and numerical methods have been conducted to study the thermal properties of GNR and ultra-high thermal conductivity has been observed [11, 12]. Recent measurements of the thermal conductivity (k) of a partially suspended graphene sheet revealed a thermal conductivity as high as 5300 W/m·K at room temperature (RT) [11]. Other experiments [12] suggest graphene has thermal conductivity of 3000–5000 W/m·K for a length l of ~ 10 μm . This high thermal conductivity exceeds that of graphite and is partly attributed to the long phonon mean

free path (MFP) in carbon nanostructures. Several research groups [10, 13] using the Brenner potential and non-equilibrium molecular dynamics (NEMD) simulations found much lower values of k in the order of several hundreds of W/m·K depending on the width, edge type (armchair or zigzag), and roughness. First principle calculations by Nika *et al.* [14] and Kong *et al.* [15] obtained k values of graphene in the range of 2000–6000 W/m·K. In several previous MD simulation investigations, however, the results turned out to be contradictory to that study. Hu *et al.* [16] calculated the thermal conductivity of GNRs (up to ~4 nm wide and ~10 nm long) around $2000 \text{ W m}^{-1} \text{ K}^{-1}$. The size of GNRs explored by Hu *et al.* is much smaller than graphene's phonon mean free path (MFP), which is about 775 nm at RT [12]. Therefore the thermal conductivity result in Hu's work is much higher than expected since the value is beyond the upper ballistic bounds [17]. It has been pointed out that quantum ballistic transport could not be fully described by MD simulation and violation of the ballistic upper bounds may be observed when calculating thermal conductance [18].

1.2. Phonon thermal transport in graphene

The exceptional thermal properties of graphene are partially due to its unique phonon transport mechanism in the 2-D system. The challenge of accounting for these phonon features gives the starting impetus to the study of graphene. There are three acoustic phonon branches, i.e. the in-plane longitudinal (LA) and transverse (TA) branches and the out-of-plane flexural (ZA) branch, which contribute to the thermal conductivity in graphene. Although for a long time it has been tacitly accepted that the

in-plane acoustic phonons are dominant in the thermal transport of graphene [19-22], recent studies have proven that the fact is quite different. Saito *et al.* [23] calculated the ballistic thermal conductance of graphene by investigating the dispersion relation of phonons and electrons. They proved that the ballistic phonon conductance of graphene below about 20 K is mainly determined by the out-of-plane acoustic mode (ZA branch) and the in-plane acoustic modes (LA and TA branches) cannot be ignored above 20 K. By measuring the thermal transport of SLG supported on amorphous SiO₂, Seol *et al.* [24, 25] performed a revised calculation and they showed that the ZA branch can contribute as much as 77% at 300 K and 86% at 100 K of the calculated thermal conductivity for suspended graphene due to the high specific heat and long mean scattering time of ZA phonons. Based on the exact numerical solution of the linear Boltzmann transport equation (BTE), Lindsay *et al.* [26, 27] calculated the lattice thermal conductivity (κ_L) of graphene at 300 K and it turned out that the dominant contribution to κ_L comes from the ZA branch, which is greater than the combined TA and LA contributions. A symmetry-based selection rule and the anomalously large density of states of flexural phonons are used to explain their results. Our study revealed the fact that in a GNR system, the ZA branch has peculiarly higher thermal conductivity than the LA and TA branches [28]. Also, ZA \leftrightarrow ZA energy transfer is much faster than the ZA \leftrightarrow LA/TA phonon energy transfer. We have proved that under the influence of a moving or static localized heat source, the flexural mode (FM) phonons dissipate heat much faster than the longitudinal mode (LM) and transverse mode (TM) phonons, which gives rise to an energy inversion phenomenon at the system level.

1.3. Scope of present work

In this work, dynamic response of graphene to thermal impulse is studied and non-Fourier heat transfer is found during ultrafast heat transfer in graphene. Phonon thermal transport is studied in three-dimensional (3D) bent graphene nanoribbons and three peculiar phenomena are reported. An energy inversion phenomenon at the system level is reported for the first time in the graphene system. Co-existing heat currents in opposite directions are observed in the graphene system. At last, thermal transport across graphene-substrate interface is studied.

The Debye model discussed in Chapter 2 is derived by Dr. Xiaopeng Huang. The diffusive heat transfer simulation in Chapter 2 is performed by Prof. Yanan Yue.

CHAPTER 2. DYNAMIC RESPONSE OF GRAPHENE TO THERMAL IMPULSE

In this chapter, MD simulation is performed to study the dynamic response of GNR to thermal impulse based on the second generation of Brenner potential [29]. A transient technique is developed to numerically measure the thermal diffusivity of GNR based on its thermal response. This technique features comparable fast MD simulation implementation and low data uncertainty. To study the size effect on dynamic thermal conductivity of GNR, different lengths (from 14.9 nm to 999.9 nm) GNR structures of 1.99 nm width are used. Quantum correction is applied to both GNR's thermal conductivity (k) and specific heat (c_p) calculation. In Section 2.1, we first introduce the pulsed laser-assisted thermal relaxation (PLTR) technique, from which our numerical method is derived. Details of this numerical method are then discussed with its application to numerically measure GNR's dynamic thermal conductivity. Section 2.2 provides MD simulation results and our analysis of size effect on GNR's thermal conductivity. Non-Fourier heat conduction is analyzed in details and thermal wave propagation in GNR's in-plane direction is studied.

2.1. Physics of the dynamic response

In MD simulations to determine the thermal conductivity of materials, non-equilibrium and equilibrium techniques can be applied. Traditional numerical methods like non-equilibrium molecular dynamic (NEMD) simulation employs heat sources and sinks to generate temperature gradient for thermal conductivity calculation. Based on the

Fourier's law of heat conduction, the thermal conductivity can be calculated from the temperature gradient and heat flux. An alternative approach to determine the thermal conductivity is equilibrium molecular dynamic (EMD) simulation based on the Green-Kubo expression that relates k to the integral over time t of the heat flux autocorrelation function by

$$\lambda = \frac{1}{3Vk_B T^2} \int_0^{\infty} \langle J(t) \cdot J(0) \rangle dt, \quad (2-1)$$

where k_B is the Boltzmann constant, V the volume, T temperature of the sample, and the angular brackets denote an ensemble average. The thermal conductivity can be calculated using Eq. (2-1) once the heat flux vector $J(t)$ is known. A detailed comparison of the MD techniques for computing thermal conductivity was conducted by Schelling *et al.* [30] Generally speaking, the NEMD approach requires large temperature gradients which takes relatively long simulation time and has significant boundary condition issues at interfaces. Results calculated by using the EMD method depend sensitively on the initial conditions of each simulation, thus necessitating a large ensemble of simulations. The slow convergence of the autocorrelation function further increases the computational demand, requiring long integration time periods [31]. Therefore in present study, a transient cooling method is developed to evaluate the dynamic thermal conductivity of GNR with much less computational time requirement while bears higher accuracy [32].

2.1.1. Dynamic method and mathematical model

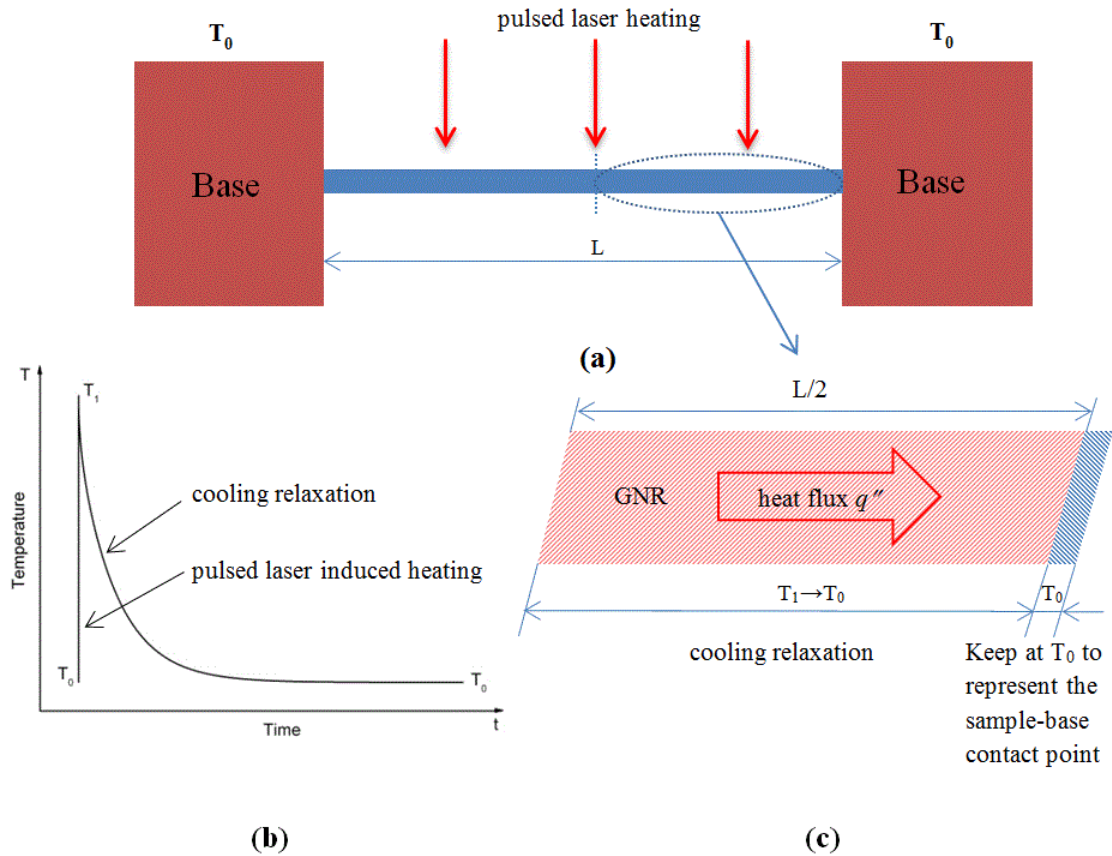


Figure 2.1. Schematic of experiment and MD simulation methods for PLTR. (a) A sample is suspended over two electrodes in experiment. The temperature of the two bases is kept at T_0 (RT). (b) Changes of sample temperature after pulsed laser heating. The sample temperature is T_0 at initial state, and then rises to T_1 quickly because of the induced heating by laser pulse. Cooling relaxation continues until sample's temperature reaches T_0 again. (c) Numerical principles derived from the PLTR technique. Temperature of the system is set at T_1 initially. Then one end of the GNR is kept at a low temperature (T_0) to represent the sample base contact point.

The numerical method used in our MD simulation process is derived from the pulsed laser-assisted thermal relaxation (PLTR) technique, which is developed by our

group to measure the thermal diffusivity of one-dimensional micro/nanoscale structures in experiment [32, 33]. In the PLTR technique, the to-be-measured sample is suspended over two copper electrodes. When running the experiment, a nanosecond laser pulse is used to irradiate the sample wire uniformly to induce a temperature increase (ΔT). Configuration of this experiment is shown in Fig. 2.1(a). Right after the pulsed laser heating, temperature of the sample will gradually go down. Temperature evolution of the sample is shown in Fig. 2.1(b). Such temperature relaxation is strongly determined by the samples' thermal diffusivity and length. From this temperature relaxation history, the thermal diffusivity of the wire can be determined with sound accuracy. In experiment, the length of the wire is significantly greater than its diameter, which will simplify the physical model to one-dimensional. The thermal conductivity is determined via 1-D heat transfer equation

$$\frac{\partial \rho c_p T}{\partial t} = k \frac{\partial^2 T}{\partial x^2} + \dot{q}, \quad (2-2)$$

with homogeneous boundary conditions and initial conditions, $T(x=0, t) = T(x=L, t) = 0$ and $T(x, t=0) = 0$. Here T only represents the temperature variation induced by the thermal impulse and \dot{q} the rate of thermal energy generation induced by the laser pulse (pulse width: Δt) heating. The solution to the partial differential equation described by Eq. (2-2) can be obtained from the integral of the Green's function,

$$G_{x_{11}}(x, t | x', \tau) = \frac{2}{L} \sum_{m=1}^{\infty} \exp[-m^2 \pi^2 \alpha (t - \tau) / L^2] \times \sin(m\pi \frac{x}{L}) \sin(m\pi \frac{x'}{L}). \quad (2-3)$$

The average temperature of the wire $T(t)$ for $0 < t \leq \Delta t$ is expressed as

$$T(t) = \frac{1}{L} \int_{x=0}^L T(x,t) dx = \frac{8\dot{q}L^2}{k\pi^4} \sum_{m=1}^{\infty} \frac{1 - \exp[-(2m-1)^2 \pi^2 \alpha t / L^2]}{(2m-1)^4}. \quad (2-4)$$

For time t larger than Δt , we have,

$$T(t) = \frac{8\dot{q}L^2}{k\pi^4} \sum_{m=1}^{\infty} \frac{\exp[-(2m-1)^2 \pi^2 \alpha t / L^2] \{ \exp[(2m-1)^2 \pi^2 \alpha \Delta t / L^2] - 1 \}}{(2m-1)^4}. \quad (2-5)$$

After normalizing as $T^* = [T(t) - T_{\min}] / (T_{\max} - T_{\min})$ (T_{\min} is 0 and T_{\max} is the maximum temperature increase of the sample calculated as $\dot{q}\Delta t / \rho c_p$), and using the relation $k = \rho c_p \alpha$, where ρ is mass density, c_p specific heat and α thermal diffusivity, the normalized temperature relaxation simplified using Taylor expansions can be written as

$$T^* = \frac{8}{\pi^2} \sum_{m=1}^{\infty} \frac{\exp[-(2m-1)^2 \pi^2 \alpha t / L^2]}{(2m-1)^2}. \quad (2-6)$$

Equation (2-6) shows that for any kind of material of arbitrary length, the normalized temperature relaxation follows the same shape with respect to the Fourier number F_o ($= \alpha t / L^2$) [32, 33]. Further convergence study shows that to make the summation in Eq. (2-6) converge, the value of the term related to m should be less than 10^{-3} of the summation from terms 1 to $m-1$. When $m = 15$, the summation in Eq. (2-6) will converge to a stable value with negligible error. The thermal diffusivity of the sample is determined by global data fitting of the temperature relaxation curve. In this method, the normalized temperature decrease is calculated using Eq. (2-6) by using different trial values of thermal diffusivity. The trial value giving the best fit (least squares) of the experimental data is taken as the sample's thermal diffusivity.

2.1.2. Atomic potential and MD domain construction

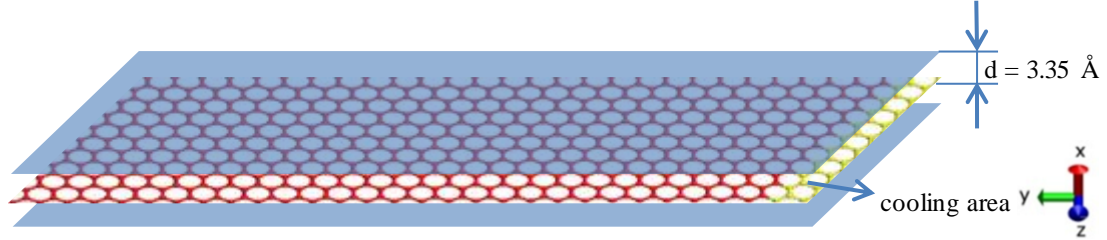


Figure 2.2. Structure of LJ walls in the x direction. The GNR is placed in the middle of upper and lower LJ walls. The distance between the wall and GNR plane is 3.35 Å.

In our MD simulation, the second generation Brenner potential [29] (REBO) based on the Tersoff potential [34, 35] with interactions between C-C bonds is used. The time step is 0.5 fs for all calculations. To avoid any stretching or compressing stress on the GNR structure, free boundary conditions are applied to the y and z directions. The simulation domain is bounded with two Lennard-Jones (LJ) walls in the x direction that enclose all the atoms. By applying LJ walls to the system, the GNR structure could be fully relaxed during the thermal equilibrium calculation and will not have folding effect. The energy E of wall-particle interactions is given by the 9-3 LJ potential

$$E = \varepsilon \left[\frac{2}{15} \left(\frac{\sigma}{r} \right)^9 - \left(\frac{\sigma}{r} \right)^3 \right] \quad r < r_c, \quad (2-7)$$

where r is the distance from particle to the wall, and ε and σ are the usual LJ parameters, which are set to be 0.00284 eV and 3.4 Å respectively. r_c represents the cutoff distance specified in simulation. The distance from each LJ wall to the GNR plane is set to be 0.335 nm, which is the distance between two neighboring carbon layers in graphite

structure. Configuration of the LJ walls is shown in Fig. 2.2.

Based on the PLTR technique, a numerical method is constructed to investigate the dynamic response of GNR and its thermophysical properties. In MD simulation, a two-dimensional GNR with free boundary conditions is initially created. The GNR used in MD simulation is of half-length compared to that used in PLTR experiment, since MD simulation only applies the transient cooling process to one end of the GNR, while in experiment, both ends of the sample is maintained at RT. In numerical method [Fig. 2.1(c)], the cooling area of GNR stands for one of the sample-base contact point in the PLTR experiment and the rest part represents half length of the sample which has been irradiated by a pulsed laser. For example, if the sample used in the PLTR experiment has a length of L , then only a $L/2$ GNR structure needs to be built in the simulation, which significantly reduces the computational time. The system is first heated to a higher temperature (325 K in our work) and reaches thermal equilibrium state before a cold impulse is added to one end of the GNR. The cooling area [shown in Fig. 2.1(c)] will maintain at a lower temperature (275 K) so the system will have thermal relaxation and reach thermal equilibrium again. To reach a steady state at 325 K before cooling relaxation starts, a canonical ensemble (NVT) is applied to the system for 500 ps. In the following 100 ps, a microcanonical ensemble (NVE) is performed to assure the system's stability. After thermal equilibrium calculation, four layers of carbon atoms at one end of GNR structure are chosen to form a "cooling group", whose temperature is "rescaled" to a value of 275 K and remains at this value through the relaxation process. The cooling

procedure is accomplished by a velocity rescaling approach. The “rescaling” process is only applied to the translational degrees of freedom for all atoms. This is an important consideration since extended spherical or aspherical particles which have rotational degrees of freedom may also reach equilibrium state with this method. To assure total momentum of the system is conserved during this rescaling process, a net velocity from the cooling group atoms is removed from the translational degrees of freedom before thermal rescaling takes place. The relaxation time used to reach a uniform temperature for the system is dependent on the length of GNR and its thermal diffusivity. The data analysis method used in the PLTR technique could also be applied to this numerical approach. From the temperature relaxation history, the thermal diffusivity of GNR can be calculated by global data fitting.

Compared with the NEMD and EMD approaches, this dynamic method takes much less time to measure the thermal diffusivity and has significantly reduced data uncertainty since more data points are used in calculation (the average temperature of the whole system is used).

2.1.3. Quantum correction

In MD simulations, the temperature can be easily calculated from the time average kinetic energy of atoms in the sample section within the simulation time using the energy equipartition theorem:

$$\langle E \rangle = \sum_1^N \frac{1}{2} m v_i^2 = \frac{3}{2} N k_B T_{MD}, \quad (2-8)$$

where $\langle E \rangle$ is the mean kinetic energy, v_i the velocity of atoms, m the atomic mass, N the number of atoms in the system and k_B the Boltzmann constant [36, 37]. However, it is worth pointing out that this method is valid only at high temperatures ($T \gg T_D$, T_D is the Debye temperature). When the system temperature is lower than the Debye temperature, it is necessary to apply quantum correction to both the MD temperature and thermal conductivity calculation. In present work, we derived the quantum correction equation for two-dimensional GNR model as

$$T_{MD} = \frac{2}{3} T_{LA} x_{LA}^{-3} \int_0^{x_{LA}} \frac{x^2}{e^x - 1} dx + \frac{2}{3} T_{TA} x_{TA}^{-3} \int_0^{x_{TA}} \frac{x^2}{e^x - 1} dx + \frac{1}{3} T_{ZA} x_{ZA}^{-2} \int_0^{x_{ZA}} \frac{x}{e^x - 1} dx, \quad (2-9)$$

where T_{MD} is the temperature in MD simulation, T_{LA} , T_{TA} , T_{ZA} are the Debye temperatures of three different acoustic modes in GNR, which are 2840 K, 1775 K, and 1120 K respectively, x_{LA} , x_{TA} , x_{ZA} are the ratios of corrected temperatures (temperatures after quantum correction, denoted as T) and Debye temperatures. Given the values of T_{MD} , which are generated in the MD simulation process, x_{LA} , x_{TA} and x_{ZA} values can be determined by the inverse form of Eq. (2-9). In our work, first of all, a wide range of T values are substituted into Eq. (2-9) to get x_{LA} , x_{TA} , x_{ZA} , and calculate the corresponding T_{MD} . After we obtain the relations (a curve) between T_{MD} and T , the corrected temperatures can be calculated by interpolation based on a specified T_{MD} . Corresponding temperatures are then used to calculate GNR's thermal conductivity and specific heat. Large differences between T_{MD} and T are observed in our work. For example, when T_{MD}

decreases from 325 K to 275K in MD simulation, corrected temperatures range from 725.8 K to 658.8 K. It concludes that quantum correction is of great importance in GNR's thermal property calculation.

2.2. Results and Discussion

To calculate GNR's thermal diffusivity, initial and final temperatures of the system need to be provided. Therefore, NVE conditions are applied to the system both before and after cooling relaxation. The average temperature values in two NVE calculations are then used as the upper and lower limits in global data fitting. During cooling relaxation, the temperature of GNR's cooling area is kept at 275 K constantly, and temperatures of the rest part are recorded for each time step. Several millions of data sets will be recorded before the system reaches thermal equilibrium. The huge amount of temperature results not only makes it difficult for data analysis, but also induces significant noises to the results. To reduce the impact of this problem, the recorded temperature data are averaged each 100 time steps before global fitting, and so as in the thermal diffusivity and specific heat calculations.

2.2.1. Fitting results of GNR and specific heat

In this work, GNRs of different lengths 14.9, 29.6, 59.4, 124.6, 249.6, 499.6, and 999.9 nm are calculated for their thermal diffusivity. The thermal conductivities of all GNRs are calculated with the same MD parameters except the cooling relaxation time.

Take 124.6 nm long GNR as an example, after the system reaches thermal equilibrium at temperature 325 K, a cold impulse is applied and it takes 650 ps for the cooling relaxation process to finish. The quantum-corrected temperature results are then used in global data fitting to determine its thermal diffusivity, which is $2.9 \times 10^{-5} \text{ m}^2 \cdot \text{s}^{-1}$. After obtaining the thermal diffusivity, the thermal conductivity can be calculated by $k = \rho c_p \alpha$. The thermal conductivity is 95.8 W/mK for 124.6 nm long GNR.

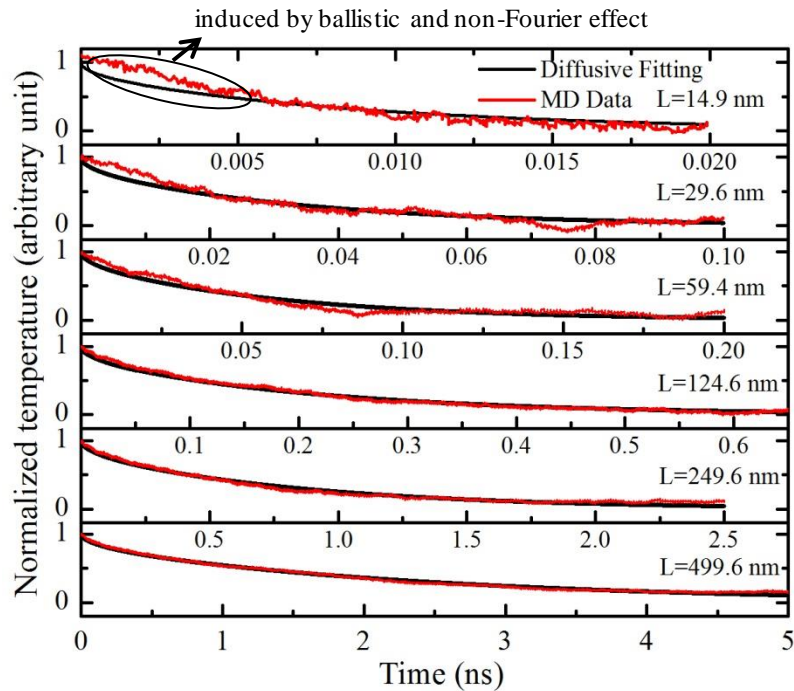


Figure 2.3. Global fitting results of different lengths GNRs at 692.3 K. The lengths of GNRs from top to bottom are 14.9 nm, 29.6 nm, 59.4 nm, 124.6 nm, 249.6 nm, and 499.6 nm.

Figure 2.3 shows global fitting curves for GNRs of different lengths. As we can see from Fig. 2.3, with the length of GNR increasing, the MD simulation results will be

more identical to theoretical results since more carbon atoms are used in the temperature calculation. Take a closer look at the fitting results in Fig. 2.3, it is found that the diffusive heat transfer model has a lower temperature than the MD data at the beginning. Then as time goes on, the agreement between them becomes better. Such early stage large difference could be induced by the non-Fourier effect heat conduction and the ballistic effect of phonon thermal transport, which will be discussed later in this paper.

To obtain the dynamic thermal conductivity of GNR, graphene's specific heat needs to be calculated first. Since c_p values are the same for GNR structures around $T_{MD} = 300$ K, we choose the 59.4 nm GNR model for our study. After 500 ps NVT and 50 ps NVE calculation, the system reaches steady state at 295.5 K. Then a heat flux of 3.3×10^7 W/m² is added to the system continuously for 500 ps. After the heating process, the system reaches steady state at 305.5 K. The temperature rise by this heating is 13.2 K after quantum correction. The specific heat is calculated by $Q = c_p m \Delta T$, where Q is the total energy added to the system, m the total mass of atoms and ΔT the temperature difference with quantum correction. Q is expressed as $Q = q'' A t$, where A stands for the heating area and t the heating time. The specific heat is calculated at 1.528×10^3 J/kg·K (at 692.3 K after quantum correction), which is nearly the same as graphite's specific heat of 1.519×10^3 J/kg·K (at 700 K) [38].

2.2.2. Thermal transport in GNRs

Ballistic transport has been observed when the phonon mean free path (MFP) is much larger than the size of GNR that contains the medium through which the phonon travels, such that the phonon alters its motion only by hitting against the walls. Recent experiments suggest that thermal transport at the nanoscale is dominated by a ballistic rather than a diffusive mechanism [12]. The power law relationship also implies that graphene conducts heat mainly through ballistic transport mode in a low temperature region [39].

In this work, however, by comparing the spatial temperature distribution of GNR in MD simulation with the theoretical results calculated from solving diffusive heat conduction equation, we could not see strong ballistic thermal transport in GNR's in-plane direction. It is probably due to the statistical oscillation of the temperature that overshadows the ballistic thermal transport. Based on the diffusive mechanism along the in-plane direction of graphene, the transient heat conduction equation $\partial T/\partial t = \alpha \cdot \partial^2 T/\partial x^2$ (α is thermal diffusivity) is solved by using the explicit method. Since the cooling relaxation curve is dependent on GNR's length and thermal diffusivity, to keep the consistency, initial and boundary conditions used in this calculation are identical with those in the MD simulations, including the α values. A short time step ($\Delta t = 10$ fs) and high spatial resolution ($\Delta x = 1$ nm) are employed in three different cases (14.9 nm, 59.4 nm and 499.6 nm).

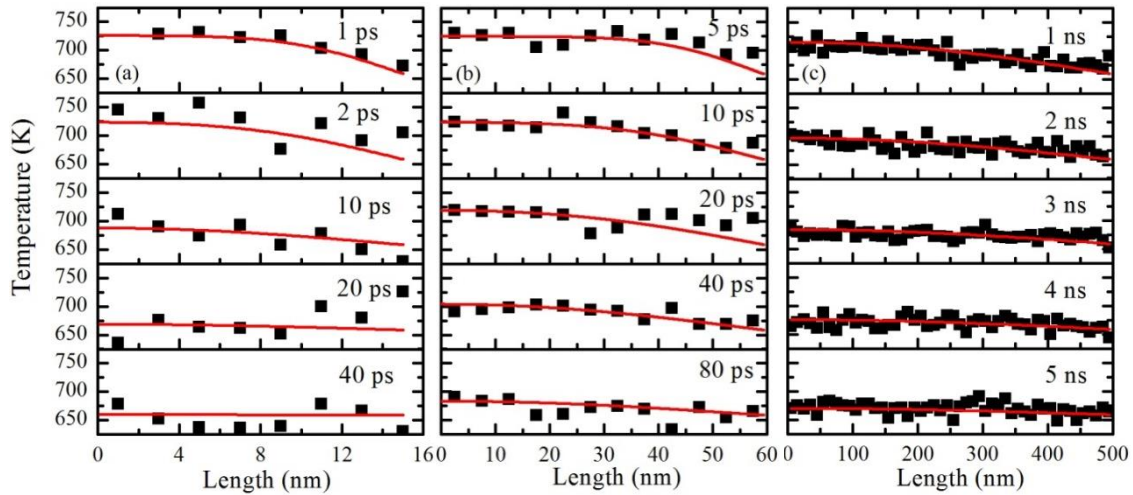


Figure 2.4. Spatial temperature evolution in GNRs at different times. The solid squares stand for MD simulation results and the curves represent theoretical results derived from diffusive heat conduction equation. The GNR length is 14.9 nm, 59.4 nm, and 499.6 nm for figures (a), (b), and (c), respectively.

The MD simulation results agree well with the theoretical curves derived from diffusive heat conduction equation. It suggests that the thermal transport mechanism in GNR's in-plane direction is quite close to diffusive situation. The temperature evolutions of GNRs are shown in Fig. 2.4. Among the three GNR structures, the case for 14.9 nm requires the shortest time to reach the steady state, while the agreement is not as good as the other two due to the lack of sufficient temperature data points in space. GNRs of 59.4 nm and 499.6 nm lengths show a sound agreement between the MD simulation results and theoretical curves. This confirms the point that longer sample length could give more accurate evaluation of the thermal conductivity. Meanwhile, high accuracy for the values of thermal diffusivity derived from the PLTR physical model in MD simulation is assured. Given the fact that the thermal transport inside GNR could mainly

be diffusive, Eq. (2-6), which is used for global fitting of thermal diffusivity, is still within the diffusive limit. However, ballistic effect is still important when GNR length is small. From Fig. 2.3, it is shown that for short GNR structures, the beginning part of MD simulation results and fitting curves do not match as well as the longer ones, which are mainly induced by ballistic effect.

2.2.3. Size effect on thermal conductivity

To better compare our MD simulation results with previous experimental and numerical data, we also calculated GNRs' dynamic thermal conductivity and specific heat at 300.6 K (after quantum correction). During the cooling relaxation process, the MD temperature decreases from 70 K to 50 K, corresponding 324.8 K to 276.6 K after quantum correction. Take the 124.6 nm GNR as an example, its thermal diffusivity and thermal conductivity values are $4.1 \times 10^{-5} \text{ m}^2/\text{s}$ and 72.6 W/m·K respectively. The specific heat of the GNR at 300.6 K is calculated at 827 J/kg·K, which is close to graphite's value of 709 J/kg·K at the same temperature [38]. Although the thermal diffusivity of GNR is higher at 300.6 K than that at 692.3 K ($2.9 \times 10^{-5} \text{ m}^2/\text{s}$), its thermal conductivity decreases due to a smaller specific heat. The calculated high values of the thermal conductivity suggest that the MFP in GNR is long even at RT. The latter may result in strong dependence of the thermal conductivity on the length l of the GNR and roughness of its edges since the phonon boundary scattering starts to play a prominent role when l is comparable to MFP. Therefore, the traditional defined thermal conductivity is no longer an intrinsic property of materials. Instead, it changes with the length of materials.

There are substantial experimental observations showing the thermal conductivity of thin films is significantly lower than that of bulk materials [40-42]. Figure 5 depicts GNR's thermal diffusivity and conductivity at different length. It can be concluded that dynamic thermal conductivity of GNR increases with its length significantly.

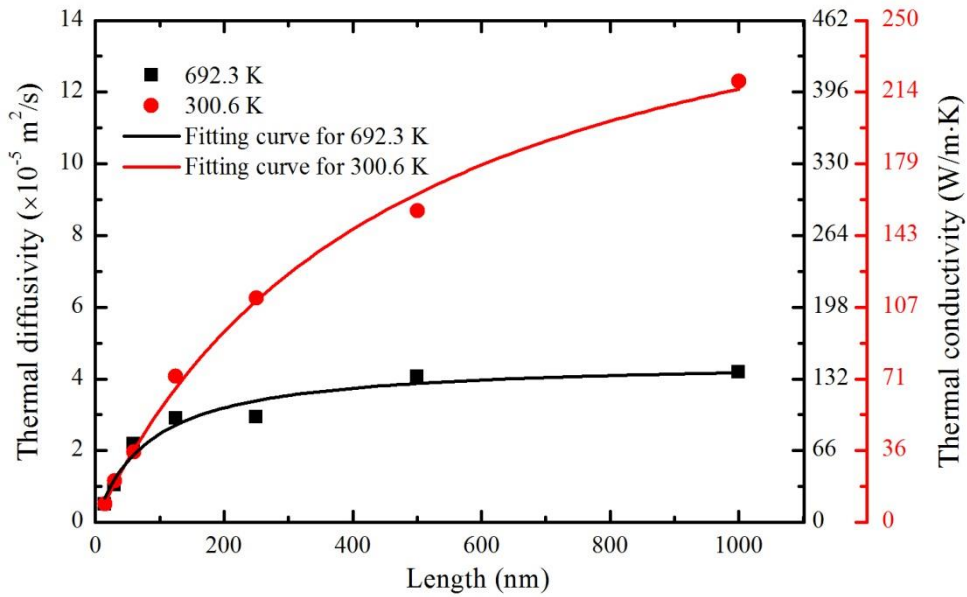


Figure 2.5. Thermal diffusivity (α) and thermal conductivity (k) variation against the GNR length.

For bulk materials, the kinetic theory gives the relationship between the macroscopic thermal conductivity and microscopic motions [43, 44] as

$$k = \frac{1}{3} \rho c_p v l, \quad (2-10)$$

where k is the thermal conductivity, ρ the mass density, c_p the specific heat, v the average phonon velocity and l the phonon mean free path, representing the average

distance a phonon travels between successive collisions. In this sense, k is the one used in Fourier's law of heat conduction

$$q'' = -k \cdot \nabla T, \quad (2-11)$$

where q'' is heat flux and T is temperature. Equation (2-10) is derived with the assumption that the space of particle motion is unbounded and is valid only if phonons can travel very long distance before they hit boundary. Equation (2-11) is simply a derivative of the more fundamental rule, the Boltzmann Transport Equation, under steady state and quasi-equilibrium conditions.

Given the calculated thermal conductivity results for different GNRs at 692.3 K and 300.6 K, we could derive k values for infinite length GNRs using data fitting. Although it is no longer meaningful to refer to thermal conductivity as a basic physical concept at micro/nanoscales, its effective value is still of great importance from the engineering perspective and is expressed for a film structure as $k_{eff} = q''L / \Delta T$, where q'' is heat flux at steady state in the length direction, L the film length and ΔT the temperature difference across the film. A material-independent relation is proposed as $k_{eff} / k = (1 + P \cdot l / L)^{-1}$, where k is the theoretical thermal conductivity of infinite length GNR, l the average phonon MFP, L the length of GNR sample, P the correlation related to boundary conditions and GNR shape. This equation is a universal relationship applicable in both ballistic and diffusive regimes of heat conduction. Since l is only related to internal scattering, its value for bulk materials can still be used and is calculated using the kinetic theory described by Eq. (2-10). It is worth noting that Eq. (2-

10) is for three-dimensional and must be adapted as $k = \rho c_p v l / 2$ for two-dimensional situations for GNR, in which the movement and scattering of phonons are confined in a plane. From the above equation, we can get the relationship between l and k for two-dimensional systems as $l = 2k / (\rho c_p v)$. Thus k_{eff} could be expressed as

$$k_{eff} = \frac{k}{1 + 2P \cdot k / (\rho c_p v L)}. \quad (2-12)$$

To carry out this calculation, only phonon velocity v needs to be specified. According to Holland [45], the following formula is a good approximation of the average phonon velocity within a wide temperature range

$$\frac{1}{v} = \frac{1}{3} \left(\frac{1}{v_L} + \frac{2}{v_T} \right), \quad (2-13)$$

where v_L and v_T are the longitudinal and transverse sound speeds. Recent research by Nika *et al.* [14] indicates that the measured longitudinal and transverse velocities in graphene are $v_L = 21.3$ km/s and $v_T = 13.6$ km/s respectively. Using Eq. (2-13), the calculated average phonon velocity for GNR is 15.5 km/s. Fitting the calculated thermal conductivity values by using Eq. (2-12), P and k values are 14 and 149 W/m·K respectively at 692.3 K while at 300.6 K, P and k are 20 and 317 W/m·K respectively. The fitting results are shown in Fig. 2.5, and sound agreement is obtained the fitting results and MD data. Majumdar *et al.* [46] derived the relationship between k_{eff}/k and L/l as $k_{eff}/k = (1 + 4l/3L)^{-1}$ for 2-dimensional heat conduction situation. This equation is also based on the Boltzmann Transport theory and indicated that P equals 4/3 for diffusive scattering boundary. Our calculated P values of 20 and 14 exceed the upper

bound of diffusive scattering. Therefore, the thermal conductivity of GNR has been greatly reduced from the theoretical values and the reduction is not only attributed to boundary scattering, but also other changes induced by phonon frequency, phonon wave length, group velocity of phonons and interactions among phonon branches.

As mentioned above, quantum correction is of great significance in the calculation of GNR's thermal conductivity. Evans *et al.* [47] applied the EMD method to calculate the thermal conductivity of graphene ribbons with dimensions of $2 \times 10 \text{ nm}^2$ at around 2000 W/m-K. The temperature they used is 300 K, which corresponds to 692.3 K after quantum correction. From Eq. (2-1) we see that their calculated thermal conductivity would be more than 5 times smaller than their current results if quantum correction is applied. The non-Fourier effect is also observed at the beginning part of GNR's thermal relaxation process, which reduces GNR's thermal conductivity to some extent. From the above discussion, we can conclude that our calculated thermal conductivity of GNR is within acceptable range compared with previous studies.

2.2.4. Ballistic and non-Fourier effect in dynamic response

Most heat conduction problems are described and analyzed using Fourier's law of heat conduction. However, it is well known that for transient problems in an extremely short period of time and very high heat flux, this classical diffusion theory may break down. The dynamic temperature responses under ultra-high speed heating have shown some behavior which could not be predicted by the thermal diffusion theory

and many models have been developed to interpret these experiments [48, 49]. Cattaneo and Vernotte formulated a well-known macroscopic description of thermal wave propagation [50, 51], which is a conventional hyperbolic energy equation expressed as

$$\tau \frac{\partial^2 T}{\partial t^2} + \frac{\partial T}{\partial t} = \alpha \nabla^2 T, \quad (2-14)$$

where τ is the relaxation time of thermal wave, T and α the temperature and thermal diffusivity. Joseph and Preziosi [48] described the microstructural effects by a relaxation function and decompose it into two relaxation times, which lead to a description of a transient heat conduction equation in the following generalized form,

$$\frac{1}{\alpha} \frac{\partial T}{\partial t} + \frac{\tau_q}{\alpha} \frac{\partial^2 T}{\partial t^2} = \nabla^2 T + \tau_\theta \frac{\partial}{\partial t} (\nabla^2 T). \quad (2-15)$$

For dielectric crystals, τ_q and τ_θ represent the relaxation times for momentum-nonconserving and momentum-conserving processes in the phonon system. Comparing Eq. (2-15) with microscopic models suggest that if τ_q and τ_θ are formulated properly by some microscopic quantities, this macroscopic model could fully describe the same heat conduction equation as those in microscopic models. Cattaneo-Vernotte's thermal wave law and Fourier's thermal diffusion law are two special cases of this generalized model for $\tau_\theta = 0$ and $\tau_\theta = \tau_q = 0$.

In this work, four layers of carbon atoms at one end of GNR are cooled to a low temperature in several time steps by a velocity rescaling method. The use of this rapid cooling technique leads to an extremely high heat flux adjacent to cooling area and non-Fourier effects have been found to exist at the beginning part of thermal relaxation

period (Fig. 2.3). To explore this non-Fourier mechanism, numerical simulation based on the implicit finite-difference method is employed to study the temperature evolution of GNR and make comparison with the MD result.

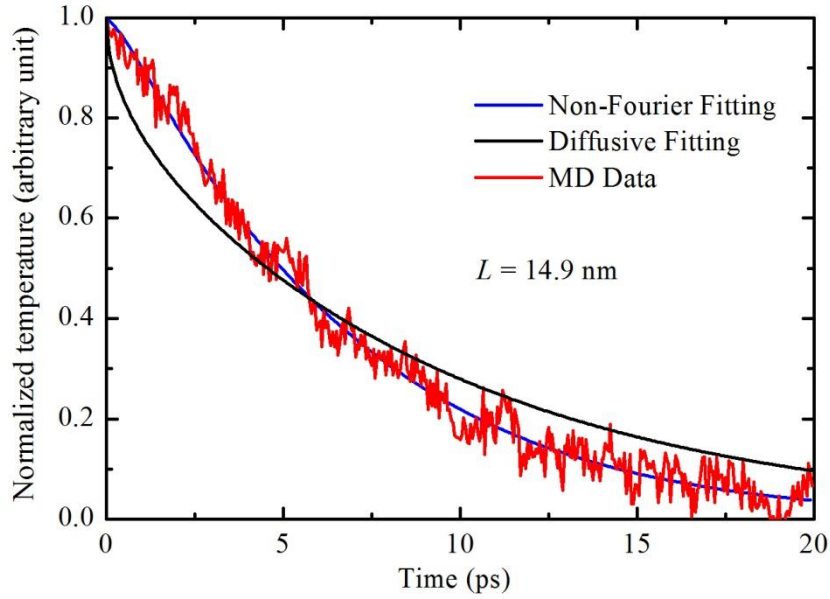


Figure 2.6. Comparison of non-Fourier fitting and diffusive fitting to MD data. MD results are above diffusive fitting curve in the first 6 ps due to a decreased effective thermal conductivity induced by the non-Fourier effect. The non-Fourier fitting curve matches MD results soundly by using two relaxation times τ_q and τ_θ .

One-dimensional discretization along the in-plane direction of GNR with spacing $\Delta x = 1 \times 10^{-2}$ nm is conducted and a small time step with $\Delta t = 5 \times 10^{-2}$ ps is used. By fitting the MD results of 14.9 nm GNR using Eq. (2-15), we give the values of τ_q and τ_θ as 1.85 and 1.01 ps respectively. The large value of τ_θ indicates that diffusive heat transfer is significant in GNR's thermal conductivity. The fitting curves are shown in Fig. 2.6. The thermal diffusivity of 14.9 nm GNR given by this fitting is 1.44×10^{-5} m²/s, which is

larger than the value of $9.55 \times 10^{-6} \text{ m}^2/\text{s}$ calculated by the previous pure diffusion model. Tang *et al.* [52] proved that a larger τ_θ will produce a higher rate thermal diffusion effect and results in rapid temperature response in early time. Since our calculated values of τ_q and τ_θ are in the same order, we could conclude that both diffusion conduction and thermal wave conduction are affecting GNR's thermal conductivity strongly at the beginning part. In Fig. 2.6, it could be seen that the MD temperatures decrease much slower than the diffusive fitting curve at the beginning, which could be explained by the thermal wave effects in non-Fourier thermal conduction.

To better understand the effects induced by the ballistic thermal transport and non-Fourier heat conduction, we plot out the spatiotemporal isothermals of 14.9 nm GNR for both the MD results and numerical results that are calculated from Fourier's diffusive heat equation. The results are shown in Fig. 2.7. As mentioned above, the GNR system has a cooling impulse of 275 K imposed on a 325 K thermal equilibrium system to calculate the GNR's thermal diffusivity. However, the temperature difference (50 K) is very small compared with the data noise, which makes it difficult to justify the temperature change in isotherms. Therefore, we initially set the GNR system at 700 K to reach thermal equilibrium, and then a cooling impulse of 200 K is added to the cooling area. For the full diffusion calculation, we use the thermal diffusivity at 300 K. The temperature of the cooling area, which is kept at 200 K, is not included in the contours. Figure 2.7(a) depicts the temperature evolution of MD results from 700 K to 200 K within the first 10 ps. Comparing the low temperature areas (violet and blue regions) in

Figs. 2.7(a) and (b), we notice that at the beginning of the heat conduction, the MD temperature diffuses slower than the numerical results, whereas after around 6 ps, the MD temperature diffuses faster than the numerical results. The temperature differences between the MD and numerical results can be explained by the non-Fourier effect. Figure 2.6 shows that the diffusive fitting curve decreases faster than the MD data at the beginning, and become flattened after around 6 ps. This is in sound agreement with the results shown in Fig. 2.7.

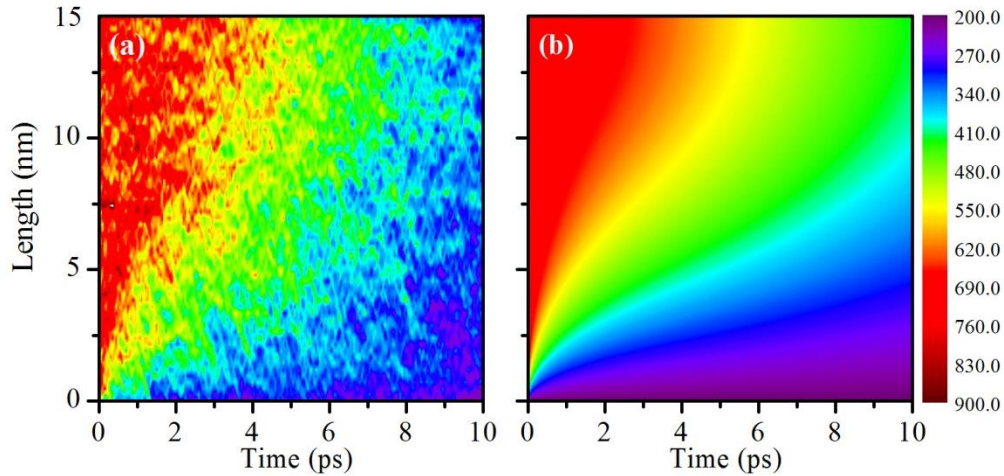


Figure 2.7. Spatiotemporal isotherms of 14.9 nm GNR with a cooling area located at the lower boundary. (a) MD results, (b) numerical results calculated from Fourier diffusive heat conduction equation. The initial system temperatures for both cases are 700 K, and then a cooling impulse of 200 K is added below the origin area.

To take a further look at GNR's thermal wave propagations, a thermal impulse is imposed upon one end of 14.9 nm GNR. The system is initially kept at 50 K to reach thermal equilibrium. Then four layers of carbon atoms at one end are connected to a

Nose-Hoover thermostat kept at 1000 K for 0.4 ps.

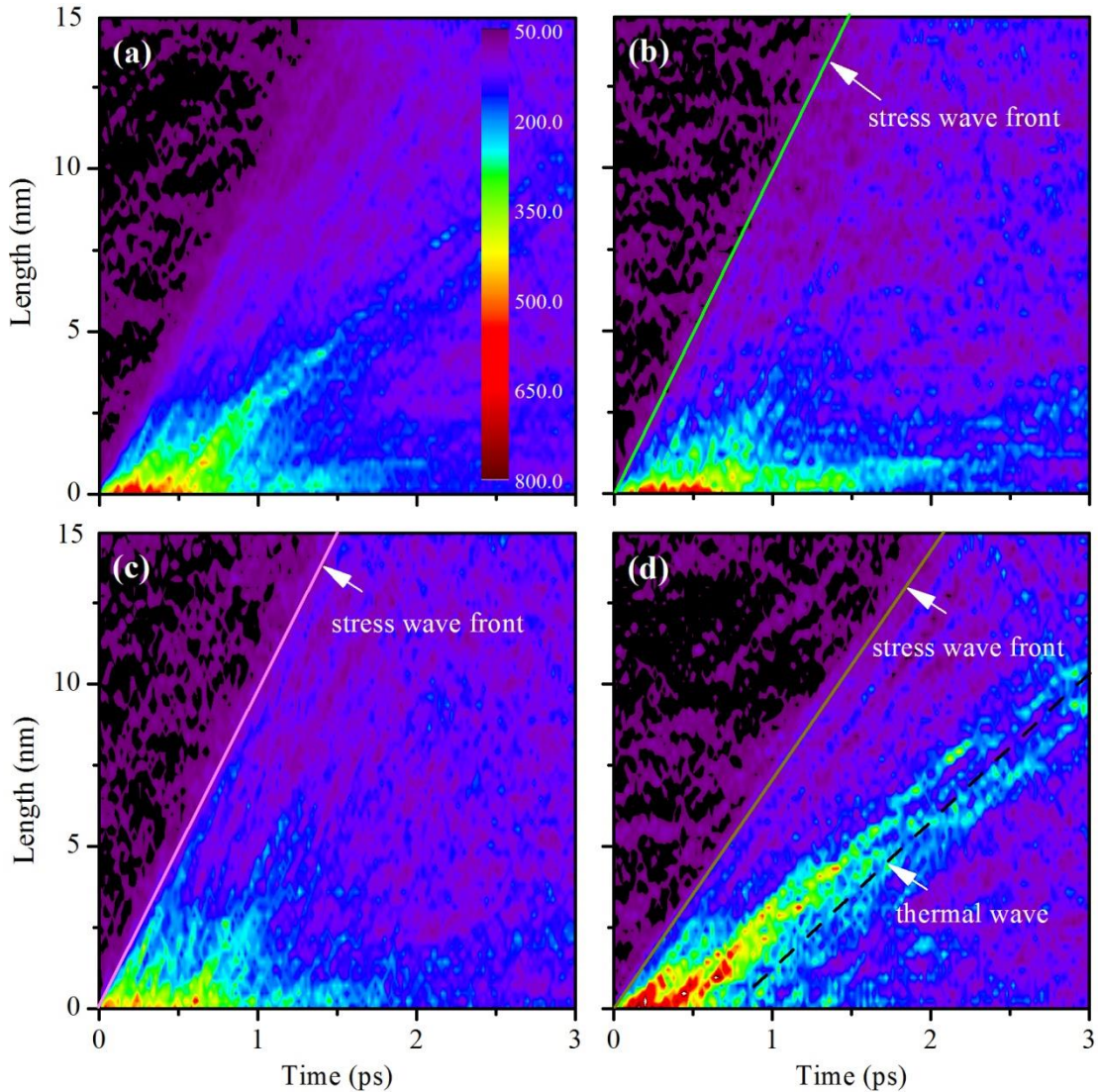


Figure 2.8. Spatiotemporal isotherms of 14.9 nm GNR with a thermal impulse imposed at the lower boundary for 0.4 ps: (a) overall temperature, (b) temperature of transverse phonons, (c) temperature of longitudinal phonons, (d) temperature of flexural phonons. Solid lines represent thermal wave front.

The rest part of GNR is divided into 64 unit cells along the length direction, each

containing about 20 atoms. The average energy of each unit cell is then used to calculate its temperature. The isotherm contours are shown in Fig. 2.8. The pictures depict how heat diffuses from the origin through the entire field. In the GNR system, heat is mainly transported by acoustic phonons, while the contribution from high-lying optic branches is small and negligible. Figure 2.8(b), (c) and (d) show the transverse, longitudinal and flexural component of GNR's thermal waves respectively. Balandin *et al.* [53] calculated lattice thermal conductivity of GNR and conclude that flexural acoustic phonons (ZA) do not make substantial contributions to heat conduction due to their low group velocity. However, recent experiments and theoretical analysis have proved that ZA phonons provide the dominant contribution to GNR's thermal conduction [54-56]. Seol *et al.* [57] carried out full quantum mechanical calculations of the three-phonon scattering processes to obtain the phonon relaxation time for each phonon mode. They calculated the substrate-phonon scattering rate for LA, TA and ZA phonon modes and found that due to the large specific heat value of the ZA mode and large mean phonon scattering time, the ZA mode contribute as high as 77% and 86% at 300 K and 100 K respectively for suspended GNR's thermal conductivity. By formulating the ballistic thermal conductance of phonons in a two-dimensional system and using phonon's dispersion relation, Nakamura *et al.* [23] calculated the contributions of the LA, TA and ZA phonons to graphene's thermal conductance. They conclude that the ballistic phonon conductance is determined by the ZA phonon modes below about 20 K and contributions of the TA and LA phonon modes cannot be neglected above 20 K while the ZA phonon modes are still in dominant. Although much work has been done to analyze ZA mode's

effect on GNR's thermal conductivity, however, to our best knowledge, there are no MD simulations have been done to prove this valuable theorem. In present work, we can clearly see in Fig. 2.8(d) that a strong thermal wave propagates through the spatiotemporal isotherms (ZA mode), while in Figs. 2.8(b) and (c) no evident thermal waves are observed. When the thermal relaxation time of phonons is large, the thermal wave effect will be more prominent. Therefore, we conclude that the ZA mode is more significant than LA and TA modes in respect for GNR's thermal conductivity. Also we can conclude that during thermal transport by the ZA phonons, the energy transfer among ZA phonons is much faster than that between ZA and LA/TA phonons. This is because if the $ZA \leftrightarrow LA/TA$ phonon energy exchange is comparable to $ZA \leftrightarrow ZA$ energy exchange, thermal wave could also be observed in the LA and TA temperature evolution. However, no thermal wave is observed in the spatiotemporal isotherms of LA and TA phonon temperatures.

In these spatiotemporal isotherms, group velocities for TA, LA and ZA mode are identified. When the 1000 K thermal impulse is imposed on one end of GNR, a local stress will be generated and will propagate in the in-plane directions. The local temperatures of GNR will remain unchanged until this stress wave arrives and its propagation speed could be measured in Fig. 2.8. Stress wave fronts are denoted by solid lines in Fig. 2.8. Since these velocities represent the energy transmission speed in GNR, they are also known as group velocities (v_g). From Fig. 2.8, the group velocities of TA, LA and ZA modes are calculated at 9.8 km/s, 9.8 km/s and 7.0 km/s respectively. Group

velocities could be calculated from GNR's dispersion relation by the expression $v_g = d\omega / dk$, where ω is the angular frequency and k the wave number. Wirtz *et al.* [58] compared GNR's phonon dispersion relations calculated by Dubay *et al.* [59] and Maultzsch *et al.* [60].

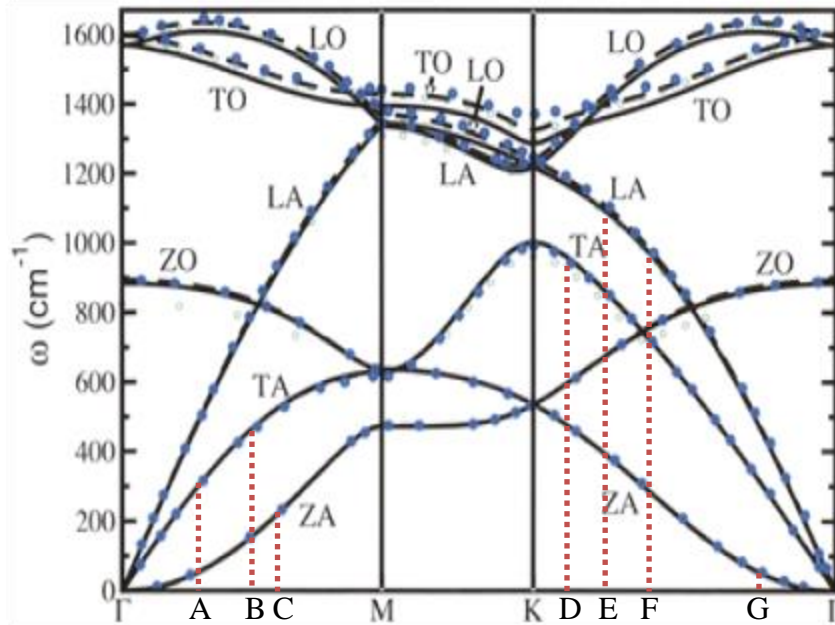


Figure 2.9. Phonon dispersion relations of graphene based on *ab initio* calculation [58]. The three phonon dispersion branches, which originate from the Γ point of the first Brillouin zone, correspond to acoustic modes and the rest three branches are for optical modes. The regions that correspond to different group velocities in Fig. 2.8 are denoted by dashed lines. (with permission from Elsevier for use in this paper)

The result is shown in Fig. 2.9. From the TA, LA and ZA dispersion relation curves in Fig. 2.9, different group velocities for each phonon branch can be calculated. On the TA curve from GNR's dispersion relation, the average group velocities

calculated in AB and DF regions are 9.7 km/s and 9.8 km/s respectively. For LA mode, EF region contributes to group velocity measured in Fig. 2.8(c) and the average group velocity in this region is 9.7 km/s. For the ZA mode, regions AC and FG have average group velocities at 6.8 km/s and 7.0 km/s and contribute to the group velocity in Fig. 2.8(d). Theoretical study of the second sound wave under linear approximation for three-dimensional materials shows that thermal wave propagation velocity is $c = v_g / \sqrt{3}$ [61], where v_g is the group velocity. For two-dimensional GNR, this relation should be modified as $c = v_g / \sqrt{2}$ [62]. In Fig. 2.8(d), the thermal wave propagation velocity is calculated at 4.6 km/s for the ZA mode, as denoted by the dashed line in Fig. 2.8(d). Based on the group velocity in Fig. 2.8(d), the thermal wave speed is predicted at $c = v_g / \sqrt{2} = 7.0 / \sqrt{2} = 4.9$ km/s. This value agrees well with the thermal wave speed 4.6 km/s observed in Fig. 2.8(d).

CHAPTER 3. THERMAL TRANSPORT IN BENDED GRAPHENE NANORIBBONS

This chapter reports on a study of the phonon behavior and thermal transport in bended graphene nanoribbons (GNRs). Three peculiar phenomena are observed in bended GNRs during thermal transport. First, due to the high thermal conductivity of flexural mode (ZM) phonons in GNRs, energy separation is observed between the in-plane and out-of-plane phonon modes after a steady state heat flux is imposed on the system. Such energy separation can hold for about 50 nm from the heating region. Second, a thermal resistance is observed in the bending region of a 90° bended GNR system. This phenomenon is explained by the phonon energy scattering/reflection and the compressive stain in the bending structure. Different bending angles are investigated and it is proved that the bending resistance decreases with an increasing bending angle. Finally, upon crossing the bending structure in GNR, phonon packages preserve their vibrating mode instead of vibrating directions.

3.1. Methodology and results

The second generation of Brenner potential [29]: reactive empirical bond-order (REBO), based on the Tersoff potential [34, 63] with interactions between C-C bonds is applied in our MD simulation. To prevent the free-standing GNR from curling and ensure full structure relaxation during the thermal-equilibrium calculation, the GNR systems are bounded within Lennard-Johns (LJ) walls in all directions that enclose all the atoms. In this work, the GNR systems have zigzag boundaries in the width direction

and armchair boundaries in the length direction. The edge carbon atoms are not hydrogen-passivated. The walls interact with the GNR atoms via the 9/3 LJ potential $E_p = \varepsilon[2/15(\sigma/r)^9 - (\sigma/r)^3]$, when $r < r_c$. r is the distance from the atom to the wall, and ε and σ are the LJ parameters, which are set to be 0.00284 eV and 3.4 Å respectively. Since the distance between adjacent carbon layers in graphite is 0.335 nm, we set this value as the initial distance between the LJ walls and the GNR boundaries.

3.1.1. Phonon energy transport in right-angle bended GNR

To ensure effective heat transfer and stable performance of graphene in future microelectronics, interconnects and thermal management structure, thermal properties of bended graphene systems should be further studied. To our best knowledge, little research has been done on this subject. In this section, bended GNR systems of length 25.0 nm, 50.1 nm, 75.0 nm and 100.0 nm with a fixed width 2.0 nm are built. Each structure is warped at the middle plane in the length direction to form a right-angle structure. Construction of the GNR system is shown in the inset of Fig. 3.1(b). To keep the formation of the GNR system, LJ walls are applied in each direction of the system. Along its length direction the GNR is divided into sections each containing about 20 carbon atoms for later temperature distribution study. The canonical ensemble (NVT) and microcanonical ensemble (NVE) conditions are applied to the system in succession at temperature 50 K to equilibrate the system. A time step of 0.5 fs is used for all calculations.

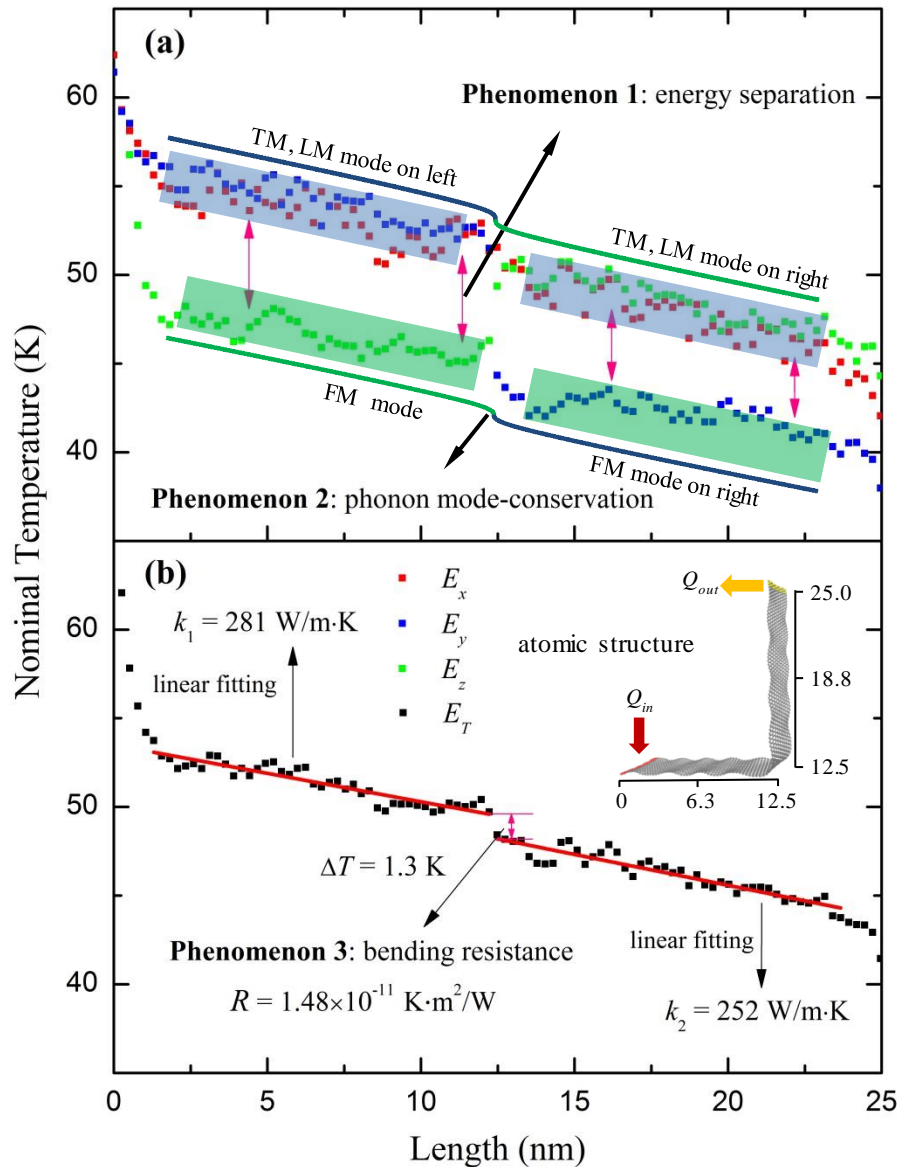


Figure 3.1. Thermal transport in a $2.0 \times 25.0 \text{ nm}^2$ right-angle bended GNR system.

The E_y and E_z exchange their values upon crossing the bending structure, indicating phonon mode-conservation in GNR systems. Bending resistance is observed around the bending area. Thermal conductivities of two flat GNR regions are calculated by linear fitting. The calculated κ and R values denoted in Fig. 3.1(b) are before quantum corrections.

Hot and cold regions are then created in the simulation domain by adding kinetic energy ΔE_k in the hot region and removing the same amount from the cold one while preserving linear momentum at each time step. Four layers of carbon atoms at each end of the GNR system are chosen to add and subtract thermal energies respectively by scaling the velocity of each atom by the same factor χ . Given enough time, the system will reach thermal equilibrium state again with a steady state heat flux flow (q'') in the length direction. Thermal energies of different phonon modes and the system are then post-processed to obtain the energy distribution along the length direction of the GNR system.

Thermal energy (Q) added/subtracted equals 5.9×10^{-8} W for all structures. Since the layer distance in graphite is 0.335 nm, we use this value as the thickness for single layer graphene [11, 28, 64-66]. The cross-sectional area (A_c) can then be calculated at 6.7×10^{-19} m². Therefore the heat flux in the length direction can be calculated from the equation $q'' = Q/A_c$, which equals 8.81×10^{10} W/m². To compare the energy evolution of different phonon modes and the whole system, a nominal temperature defined as $E_i/(1/2)k_B$ with unit K is used to represent the energy values in each direction and a value $E_T/(3/2)k_B$ with unit K stands for the system's total energy. Here E_i is the kinetic energy of carbon atoms in direction i ($i=x, y, \text{ or } z$), and E_T is the total kinetic energy of carbon atoms.

The nominal temperature results of the 2.0×25.0 nm² right-angle bended GNR

are shown in Figs. 3.1(a) and (b). Since the GNR is warped at the middle plane, the bending structure is located at 12.5 nm position in the length direction. The black, red, blue and green data points are for the kinetic energy of the system (E_T), x , y , and z direction components: E_x , E_y , and E_z , respectively. Three crucial phenomena are observed in these two figures. The first one is the phonon energy separation among different phonon modes, which happens all the way along the length direction. The second one is that upon the phonon energies crossing the bending structure, an energy jump between E_y and E_z is observed. After the phonon energies go across the bending region at 12.5 nm, E_y and E_z exchange their positions and E_y becomes the lowest energy value in the system. Consequently, the phonon energy will flow from E_x and E_z to E_y after they pass through the right-angle region until they reach the same level. Based on this result, it concludes that when the phonons pass through a bending area, the phonon modes are preserved, i.e. the flexural phonon branch remains vibrating in the out-of-plane direction after it passes through the bending structure and the in-plane TM and LM branches keep vibrating perpendicular and along the phonon propagating direction. Detailed proofs are given in later sections using separated phonon mode excitation. Phenomena 1 and 2 are denoted in Fig. 3.1(a).

Last but not least, the third phenomenon is that an energy drop across the bending area is observed for each energy mode, indicating an energy barrier exists in the bending region which causes a local thermal resistance (R) between the horizontal and vertical parts of the GNR system. R can be calculated as $R = \Delta T/q''$, where ΔT is the

temperature drop (K) and q'' the heat flux along the path of heat flow (W/m^2). ΔT is evaluated at 1.3 K in the $2.0 \times 25.0 \text{ nm}^2$ GNR system and the corresponding bending resistance is $1.48 \times 10^{-11} \text{ K}\cdot\text{m}^2/\text{W}$ before quantum correction. Phenomenon 3 is shown in Fig. 3.1(b). The thermal conductivity values of the horizontal and vertical parts of the GNR are calculated using Fourier's Law: $q'' = -\kappa \nabla T$, where ∇T is the temperature gradient. It is worth noting that in general both electrons and phonons contribute to the thermal transport in graphene. In this work the MD temperatures for all GNR systems are around 50 K, which correspond to ~ 300 K after quantum correction. And at this temperature, the phonon's contribution to graphene's thermal conductivity is nearly 100 times greater than that of electrons [23]. Besides, according to the Wiedemann-Franz law, the estimated contribution of electrons to graphene's thermal conductivity is less than 1% at room temperature [67]. This is also consistent with the observation for the thermal conductivity of individual carbon nanotubes (CNT) [68, 69]. From these prospects, previous MD simulation studies about the edge and length effect on graphene's thermal conductivity also just consider the phonon contributions and electrons contributions are neglected [16, 66, 70-72]. Therefore, in this work we only consider the phonon contribution to GNR's thermal conductivity. By linear fitting the data from these two parts, the κ values are calculated at 281 $\text{W}/\text{m}\cdot\text{K}$ and 252 $\text{W}/\text{m}\cdot\text{K}$ for the horizontal and vertical parts before quantum correction. It is observed that the thermal conductivities for the horizontal and vertical parts are different, which is mainly caused by two reasons. First, since the horizontal part has the heat source and vertical part has the heat sink, the phonon energy distributions are different in these two parts, as

is shown in Fig. 3.1(a). Also, the total temperatures for these two parts are different, and the thermal conductivity of graphene is temperature dependent. Second, the calculation uncertainty also contributes to the differences. In the linear fitting process, we have to manually choose the fitting region to calculate the thermal conductivities and the results will be slightly different even if we change the fitting range by several points. We tried our best to choose the most reasonable fitting region, yet the calculation uncertainty is inevitable. Thus, we think the 10% thermal conductivity difference for these two parts is acceptable.

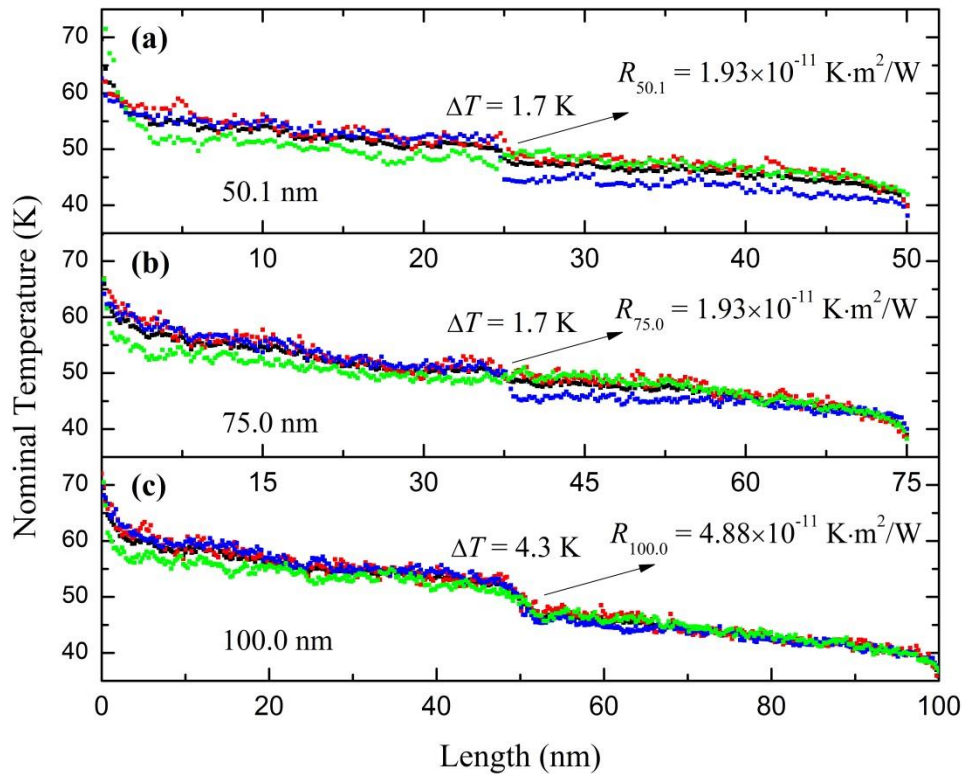


Figure 3.2. Nominal temperature distributions in different length 50.1 nm, 75.0 nm and 100.0 nm right-angle GNR systems. Each GNR structure has a fixed width of 2.0 nm. The bending resistance values denoted in the figures are without quantum corrections.

Nominal temperature results for right-angle GNR of length 50.1 nm, 75.0 nm and 100.0 nm are shown in Fig. 3.2. The temperature drop in the bending structure of each system is 1.7 K, 1.7 K, 4.3 K respectively and the corresponding thermal resistances are 1.93×10^{-11} , 1.93×10^{-11} , 4.88×10^{-11} K·m²/W before quantum correction. Thermal resistance is also calculated for the 200.0 nm right-angle GNR and the results is 4.2×10^{-11} K·m²/W. Both energy separation and energy drop phenomena are observed in all cases. Since the Debye temperature of graphene is around 2300 K [73], while in our calculations, the MD temperature for the GNR system is around 50 K. The huge difference between them makes it a must in this work to apply quantum corrections to the MD temperatures. In chapter 2, we derived the quantum correction equation for two-dimensional GNR model. After applying quantum correction to previous results of thermal conductivity and bending resistance, we get the revised κ values at 109 W/m·K and 92.7 W/m·K for the horizontal and vertical parts and revised R values at 3.93×10^{-11} K·m²/W for the 2.0×25.0 nm² GNR. The thermal conductivity results are higher than our previous calculated κ values [28], which could be caused by the difference between dynamic and steady state thermal transport processes involved in thermal conductivity definition. For low-dimensional systems such as GNR, the definition of cross-sectional area has certain arbitrariness. In previous experimental studies of graphene's thermal conductivity, Balandin *et al.* [11, 64] used the value of 0.35 ± 0.01 nm as the thickness of single layer graphene. Lee *et al.* [74] and Cai *et al.* [65] used the SLG thickness of 0.335 nm in their calculations. Most of the numerical work studying the thermal conductivity

of graphene chose the value 0.335 nm as the thickness [16, 28, 66, 72, 75], yet only the study by Guo *et al.* [71] used the value of 0.144 nm in graphene's thermal conductivity calculations. Therefore, our calculations of GNR's thermal conductivity uses the same thickness value (0.335 nm) as most of the experimental and numerical work chose. This provides a common base when comparing our results with those by other researchers. As for the 50.1 nm, 75.0 nm and 100.0 nm length GNRs, the corrected bending resistance values are 5.04×10^{-11} K·m²/W, 5.04×10^{-11} K·m²/W, 1.29×10^{-10} K·m²/W respectively. Yue *et al.* [76] calculated the interfacial thermal resistance between graphene layer and 4H-SiC substrate at 7.01×10^{-10} and 8.47×10^{-10} K·m²/W for surface heat fluxes of 3.0×10^9 and 1.0×10^{10} W/m² respectively. Other groups using the 3ω method measured contact resistance between graphene and silicon dioxide in the range of 5.6×10^{-9} to 1.2×10^{-8} K·m²/W [77]. It could be seen that our calculated R values are much lower than the interfacial thermal resistance between graphene layer and other materials, which is as expected since there is no flexural phonon coupling and scattering at those interfaces [21, 22].

3.1.2. Energy separation in flat GNR

To further explore the phonon energy separation observed in the bended GNR systems, different lengths (25.0, 50.1, 75.0 and 100.0 nm) flat GNRs with a fixed width of 2.0 nm are built and studied. Schematic construction of a flat GNR is shown in Fig. 3.3. Following the same routines used in the bended GNR systems, the NVT and NVE

conditions are performed to equilibrate each structure at 50 K and a time step of 0.5 fs is used for all calculations. Hot and cold regions are then created to induce a steady state heat flux flow (q'') in the length direction and nominal temperature data are extracted and averaged for each unit cell.

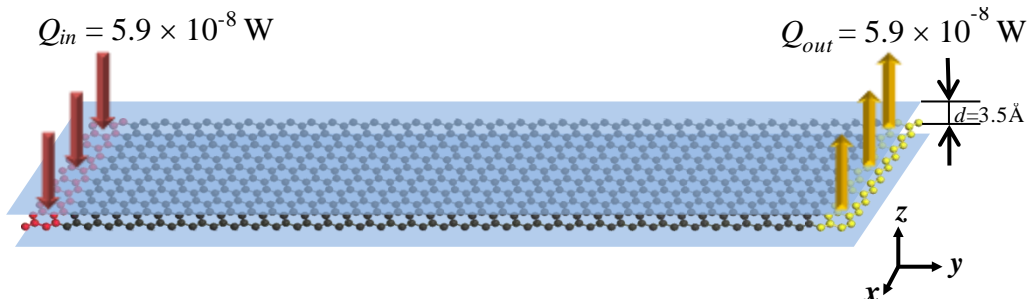


Figure 3.3. Atomic structure of the flat GNR system studied for energy separation. The Lennard-Johns (LJ) potential walls are applied in all dimensions. To make a clear schematic description, only the top and bottom LJ walls are shown. Distance between each LJ wall and the GNR plane is set as 3.5 Å initially. A thermal energy of 5.9×10^{-8} W is added/subtracted from the red and yellow areas respectively.

Take the 2.0×25.0 nm² flat GNR as an example, after 200 ps NVT and 50 ps NVE thermal equilibrium calculations, the system reaches steady state at 50 K. Then another 100 ps is calculated after heat flux is applied to the system. After the system reaches steady state, energy data are collected and averaged for the next 50 ps. The nominal temperature distribution of the system and its decomposition are shown in Fig. 3.4(a). It is seen from this figure that E_x and E_y values are almost the same along the length direction. However, E_z values are much lower than them. The energy differences are decreasing from the heating to cooling region, indicating energy transfer from E_x and

E_y to E_z along the flat GNR until the three energy components reach the same level. To verify our speculation, nominal temperature distributions of 50.1 nm, 75.0 nm and 100.0 nm length GNRs are calculated and the results are shown in Figs. 3.4(b), (c) and (d). Energy separation is observed in all cases and the three energy components reach the same level at around 50 nm.

For this first-time observed phonon energy behavior in graphene, our understanding of the driving force behind it is the much higher thermal transport capability by the flexural mode phonons. Mechanism of the phonon energy transfer is depicted in Fig. 3.4(e). In the hot region, local phonon energies of the GNR will increase dramatically when the heat flux is added to the area. This high local energy will then be transmitted to the low nominal temperature regions by E_x , E_y and E_z . As mentioned above, despite the fact that the ZA phonons have vanishing group velocities for wave vector $q \rightarrow 0$, its high specific heat and long phonon mean scattering time make the ZA branch dominant in graphene's thermal conductivity. The large density of states and phonon scattering selection rule for the ZA branch also contribute to its anomalously large thermal conductivity [24, 26]. Therefore, the local flexural mode phonons in the hot region will transfer heat much faster than the in-plane modes phonons, giving rise to the lower E_z values along the length direction in which heat is conducted. Consequently thermal energies keep transferring from the in-plane phonons to the flexural phonons until they reach the same level.

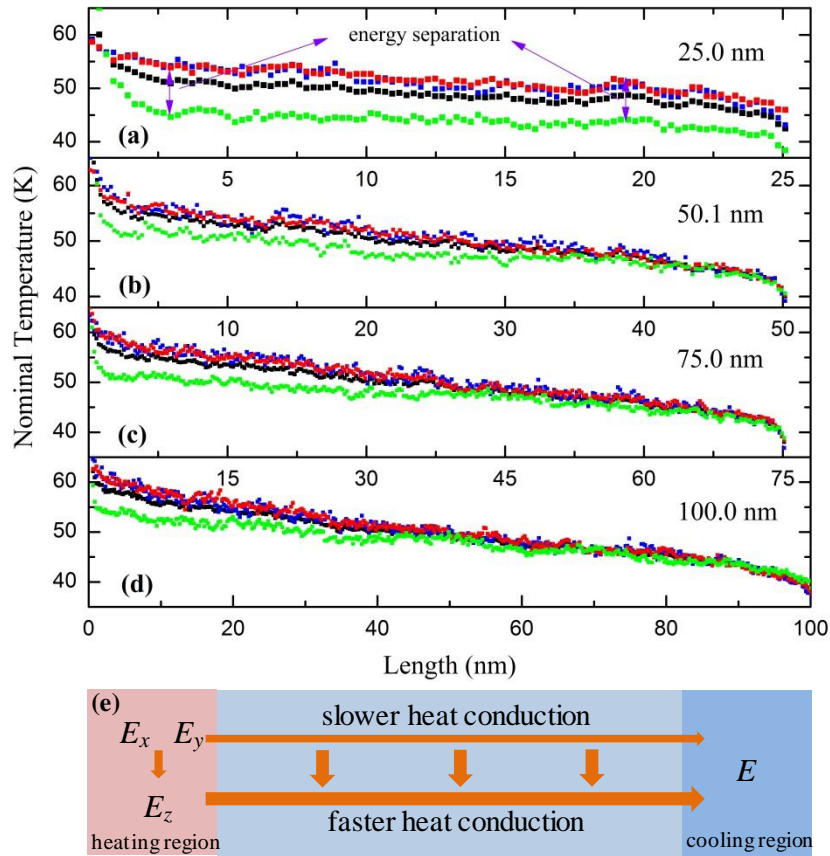


Figure 3.4. Nominal temperature distributions in flat GNR systems of different length (a) 25.0 nm, (b) 50.1 nm, (c) 75.0 nm and (d) 100.0 nm. Each GNR structure has a fixed width of 2.0 nm. A thermal energy of the same value 5.9×10^{-8} W is added/subtracted in the selected regions for all systems. It is observed that energy separation happens at short distances in the heat flux flow direction and disappears at around 50 nm. (e) A schematic explanation of the thermal transport mechanism in short GNRs. The ZM branch has higher thermal transport ability than the in-plane TM and LM branches. Therefore E_z is lower than the E_x and E_y and the latters will keep transferring energies to E_z until they reach the same level.

3.1.3. Phonon mode-conservation

In general, the thermal conductivity of a solid arises from two distinct contributions: one from phonons and the other one from electrons. In this work, only

lattice thermal conductivity is considered. Consequently, phonon package propagations determine the thermal transport properties in the GNR system. To explain the bending resistance in the right-angle bended GNR system, it requires further investigation of phonon transport in the bending region. For this purpose, a $2.0 \times 50.1 \text{ nm}^2$ right-angle GNR system is built. Construction of the GNR is the same as the inset of Fig. 3.1(b). The system is equilibrated at 50 K after 300 ps NVT and 50 ps NVE calculations. Then four layers of carbon atoms at one end of the GNR system are grouped to apply a stretching force (F), which is added to each atom in the group and has a value of 1.0 eV/Å. The time step is 0.5 fs in the thermal equilibrium calculations and 0.05 fs for the stretching. A short period of time 25 fs is used for the stretching process (phonon excitation). By applying the stretching force in the x , y and z directions separately, TM, LM and ZM phonon packages are generated separately in the GNR system, which propagate from the excitation area to the other end along the length direction.

Spatio-temporal energy contours are plotted in Fig. 3.5 for the LM and ZM phonon packages. Figures 3.5(a) and (b) show energy contours of E_y and E_z after LM phonon excitation (E_y) at the left end. Figures 3.5(c) and (d) show energy contours of E_z and E_y results after ZM phonon excitation (E_z) at the left end. The bending position (25.0 nm) for each structure is denoted by the dashed lines. In Fig. 3.5(a), after the excitation, a phonon package wave (E_y) is generated propagating along the length direction until it confronts the bending plane. A reflection wave has been observed in the corner. The disappearing LM phonon package wave in Fig. 3.5(a) emerges in the right part of Fig.

3.5(b) and these two waves are continuous since they share the same starting/ending point and have the same slope. This proves the fact that after the LM phonons pass through the bending area, their vibrating path changes from the y direction (E_y) on the left side to the z direction (E_z) on the right side. The phonon mode is preserved instead of the absolute vibrating direction. Reflection waves are also found in the bending plane in Fig. 3.5(b). Despite the fact that the phonon package waves in Figs. 3.5(a) and (b) are continuous, the phonon package energies are dramatically reduced upon crossing the bending corner since the wave fronts in Fig. 3.5(b) are much weaker and thinner than those in Fig. 3.5(a). Similar phenomenon is observed for the ZM phonon excitation case in Figs. 3.5(c) and (d). After the excitation is applied in the z direction, ZM phonon package waves are generated in the left part of Fig. 3.5(c) and propagate to the right of the system. As mentioned above, since the ZM branch is dominant in GNR's thermal conductivity, the ZM phonon packages in Figs. 3.5(c) and (d) are much stronger than the LM phonon packages. This confirms the point that energy separation in GNR is caused by the strong thermal transport capability of the ZM branch.

From the above discussions, we can safely draw a conclusion that after the phonon packages pass through the bending structure in GNR, instead of remaining their absolute vibrating directions, they preserve their vibrating modes. To sum up, the spatio-temporal iso-energy contours indicate that the flexural phonons will always vibrate in the out-of-plane direction of the GNR while the longitudinal phonons will always vibrate along the thermal conduction direction. Also, phonon scattering and reflections are

observed in the bended structure.

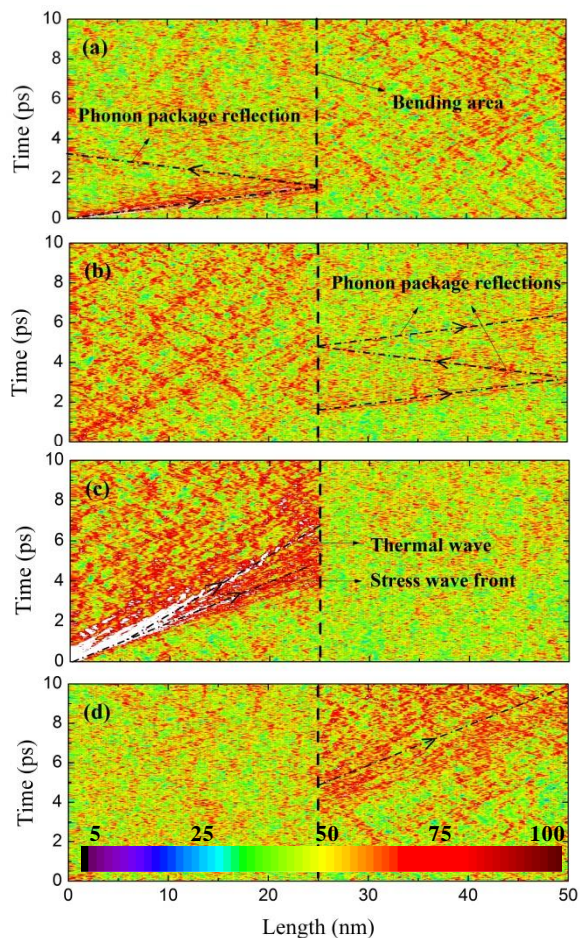


Figure 3.5. Spatio-temporal iso-energy contours for the right-angle GNR structure. (a) and (b) represent E_y and E_z evolution after the LM phonon excitation (E_y) at the left end. (c) and (d) are for E_z and E_y evolution after the ZM phonon excitation (E_z) at the left end. Phonon mode-conservation is observed for the LM and ZM phonon branches. Phonon package reflections are also observed in the middle-plane at the bending region.

Aside from the phonon packages propagation and reflection phenomena mentioned above, phonon coupling between in-plane and out-of-plane phonons is also

observed. It could also be seen that E_z values in the left part of Fig. 3.5(b) become higher than the E_y in the left part of Fig. 3.5(a) as the LM phonon package propagates. E_z in the left part of Fig. 3.5(c) remains higher than E_y in the left part of Fig. 3.5(d). This confirms our previous research results that the in-plane TM and LM phonons have a higher energy transfer rate to the out-of-plane ZM phonons and the latter are inclined to transport thermal energies to themselves rather than to other phonon modes. In the left part of Fig. 3.5(c), we can clearly see a thermal wave is generated in the length direction as the ZM package propagates. When the thermal-relaxation time of the phonons is large, the thermal-wave effect will be more prominent. Therefore, the ZM mode is more significant than the TM and LM modes with respect to GNR's thermal conductivity. From Figs. 3.5(a) and (c), the group velocities for the LM and ZM phonons are calculated at 15.34 km/s and 5.05 km/s respectively. A theoretical study of the second sound wave under the linear approximation for three-dimensional materials shows that thermal wave propagation velocity is $c = v_g / \sqrt{3}$ [61], where v_g is the group velocity. For two-dimensional GNR, this relation should be modified as $c = v_g / \sqrt{2}$ [62]. In Fig. 3.5(c), the thermal wave propagation velocity is calculated at 3.43 km/s for the ZM mode, as denoted by the dashed line. Based on the group velocity in Fig. 3.5(c), the thermal wave speed is predicted at $c = v_g / \sqrt{2} = 5.05 / \sqrt{2} = 3.57$ km/s. This value agrees well with the thermal wave speed 3.43 km/s observed in Fig. 3.5(c).

3.1.4. Energy barrier across the bending region

Two distinct types of parameters control the effective thermal conductivity of GNR: thermodynamic parameters such as temperature and pressure/strain, and extrinsic parameters such as impurities, defects and bounding surfaces.

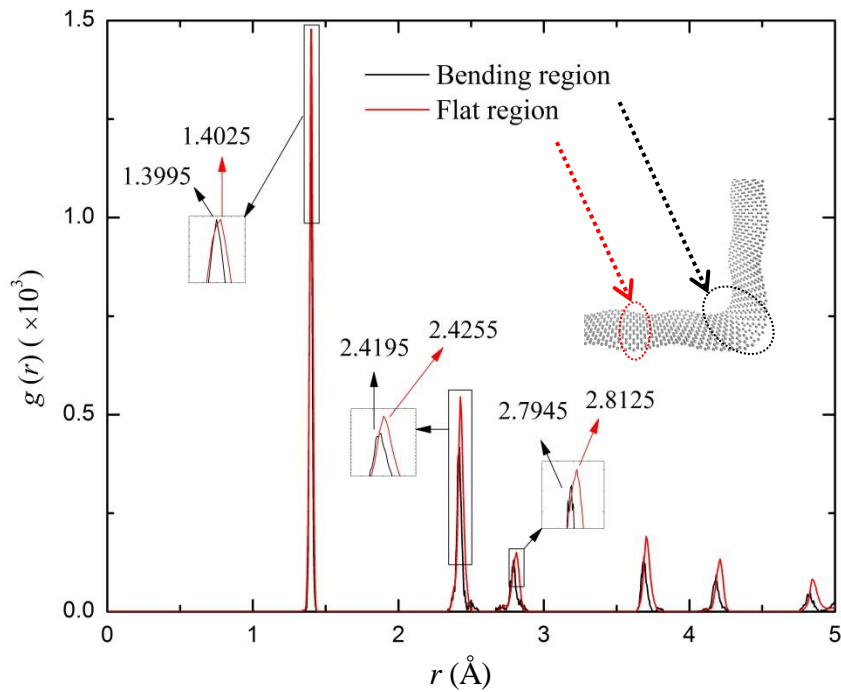


Figure 3.6. Radial distribution function (RDF) of the flat and bending areas in the $2.0 \times 50.1 \text{ nm}^2$ right-angle bended GNR system. The black and red lines represent the RDF at the bending area and flat area. The RDF for the bending area shows a smaller atomic distance than that in the flat area, indicating a compressive strain in the bending structure.

In this work, all GNR models are pristine without the influence of the latter parameters, thus only temperature and strain/stress effects should be considered. An energy barrier is observed in the bending structure of the right-angle GNR and it is

necessary to investigate if there is a local strain in this area. To take a closer look at the structure deformation caused by the bending, the radial distribution function (RDF) is used to explore the atom structure change in the bending area. The RDF results for both flat and bending regions are shown in Fig. 3.6. It is seen that the nearest neighboring distance in the bending area of GNR is shorter than that in the flat area, indicating that a local compressive strain is generated in this area. By comparing the positions of the first peaks in Fig. 3.6, the compressive strain (ε) in the bending area is calculated at -2.14×10^{-3} . Given the nearest neighboring distance in an exact hexagonal structure, the second and third nearest neighboring distances could be calculated accurately. In Fig. 3.6, the nearest neighboring distance in the bending region is 1.3995 Å, which corresponding to the theoretical second and third nearest neighboring distances of 2.424 Å and 2.799 Å respectively. In the RDF results, the second and third nearest neighboring distances in the bending region are 2.4195 Å and 2.7945 Å. The slight differences between the theoretical and calculated values indicate the hexagonal structure still holds good in the bending area. Unlike bulk materials such as silicon and diamond whose thermal conductivity will increase due to a compressive strain in the system, the single layer nature of GNR makes it have a decreased thermal conductivity under either compressive or stretch strains [78, 79]. Because when a compressive strain is applied to the GNR structure, buckling in the out-of-plane direction will occur, resulting in an increasing phonon scattering rate and thus a reduced thermal conductivity. Therefore, it is conclusive that a free-standing GNR system will have a higher thermal conductivity than those with stains. In our case, since there is a compressive strain in the bending area of

the GNR, the local thermal conductivity will drop, which constitute one of the reasons for the bending resistance in this region.

The RDF for the 25.0 nm, 75.0 nm and 100.0 nm bended GNRs is also calculated. It is worth noting that the local strain in the bended structures cannot only be calculated from the position of the first peaks, the second and third peak differences can also be used to evaluate the local strain. By comparing the first peak positions, the local strain values are calculated at 0, -2.14×10^{-3} , 0 and -6.77×10^{-3} respectively for the 25.0 nm, 50.1 nm, 75.0 nm and 100.0 nm right-angle bended GNRs. From the second peak positions, the strains are calculated at -4.74×10^{-3} , -2.47×10^{-3} , -1.44×10^{-3} and -6.18×10^{-3} respectively. At last, the third peak positions give strain results of -4.27×10^{-3} , -6.4×10^{-3} , -9.6×10^{-3} and -6.22×10^{-3} respectively. The zero strain based on the first-peak position means the nearest atomic distance is not altered in the bending area. Instead, the structure is twisted, and the extent of twisting is reflected by the strains calculated from the second and third RDF peaks. From the above results, it is ready to see that the local strain of the 100.0 nm case is much larger than the others with respect to the first and second peaks. This much larger strain will give much stronger phonon scattering than other cases, and lead to a larger thermal resistance. And according to Li *et al.* [78], the thermal conductivity of graphene decreases with an increasing local strain and the phonon scattering becomes stronger as the local strain increases. Therefore, the thermal resistance in the bending structure will also increase with the local strain. This explains the highest thermal resistance for 100.0 nm bended GNR shown in Fig. 3.2(c) in our four

calculated cases.

In the end, the bending resistance in the right-angle bended GNR is mainly caused by two factors: one is the phonon wave package scattering and reflections at the bending area; and the other one is the compressive strain in the bending structure which increases the phonon scattering and causes a thermal conductivity decrease.

3.2. Discussion

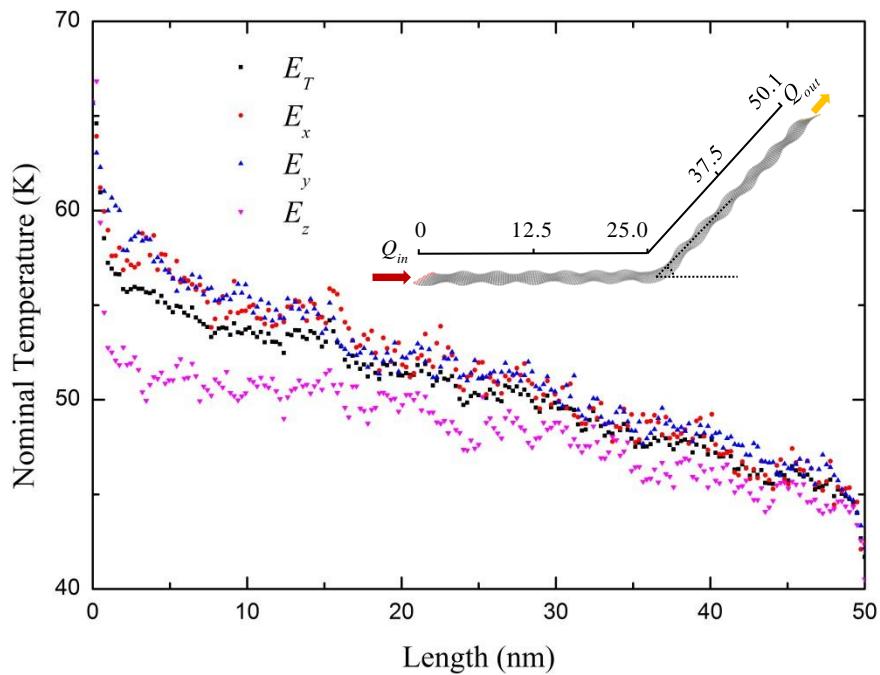


Figure 3.7. Nominal temperature distributions for the 135° bended GNR with dimensions of $2.0 \times 50.1 \text{ nm}^2$. Atomic structure of the system is shown in the inset. Energy separation is observed in this structure, yet no obvious bending resistance or energy jump has been found.

To further investigate the effect of bending angles on the thermal transport in GNRs, a 135° bended GNR system with dimensions of $2.0 \times 50.1 \text{ nm}^2$ is built. After thermal equilibrium calculations at 50 K, thermal energy of $5.9 \times 10^{-8} \text{ W}$ is added/subtracted at each end of the system separately and the nominal temperature distribution results are shown in Fig. 3.7. The atomic structure is depicted in the inset of Fig. 3.7. No obvious bending resistance or thermal conductivity changes are observed in this figure, yet energy separation still exists until the phonon energies reach the same level at $\sim 50 \text{ nm}$ position, similar to the flat GNR cases shown in Fig. 3.4. From above cases, it summarizes that the energy barrier decreases with an increasing bending angle. Actually, we also consider including the bended graphene structures for the range 0° to 90° . For example, we tried to build a 45° bended GNR structure to compare with previous cases but at the beginning stage of our calculations, we found that the initial distance between the carbon atoms around the bending corner is too close that they bounced away instantly when the thermal equilibration starts. We try to solve this problem by reducing the time step from 0.5 fs to 0.05 fs and adjusting the LJ potential wall distance, but still the bended structure could not hold. Therefore we did not report 0° to 90° bending cases in this work and our conclusions just apply to 90° to 180° bended GNRs. In our future work, effort will be taken to obtain 0° to 90° bended GNR structures by increasing either the GNR length or the strength of the GNR-wall interaction potential.

In the end, we discuss the 9-3 LJ potential walls' effect on the thermal transport

in GNR. It is true that the LJ potential walls will affect the out-of-plane form of the GNR and also the radius of curvature in the bending structure, which makes above reported thermal conductivity and thermal resistance results dependent on the 9-3 LJ potential parameters chosen in this work. Intuitively, the strength of the LJ potential controls the degree of bending for a GNR and its effective curvature in the bent region. The stronger the potential is, the larger the curvature and thermal resistance will be. This logic is supported by the results calculated above for different GNR lengths. A decrease in the GNR length would decrease the torque from GNR-wall interaction forces that counterbalance the internal straightening forces in the GNR due to bent deformations and, thus, should decrease the radius of curvature and the thermal resistance of the bent region. Since the bended GNR are enclosed by potential walls in all directions, the bending position is fixed for a specific GNR system, which also contributes to the variation of thermal resistance values since the bending position will also affect the R results for bended GNRs. The LJ parameters used in this work are balanced results that are able to keep the formation of the bended GNR while ensuring the system is not over suppressed by the LJ walls. In other words, the LJ potential we applied is not an extreme case but properly adjusted. This could be seen from the fact that the atomic configurations for the obtuse angle (90° - 180°) bended GNRs are well maintained while the LJ potential is not so strong to be able to hold an acute angle (0° - 90°) bended structure. To study the thermal properties of a bended GNR, it is necessary to apply the L-J walls to the system. Otherwise the system will have spurious global rotation in the simulation. The LJ potential walls are intrinsically different from a substrate used in a

supported graphene [80]. The 9-3 LJ potential is commonly used to model the interaction between atoms with a flat structureless solid wall or *vice versa*. This soft repulsive potential wall will generate a force on the atoms in the direction perpendicular to the wall. The Van der Waals force between the GNR and the LJ wall is much weaker than the covalent bond force between the carbon atoms in graphene.

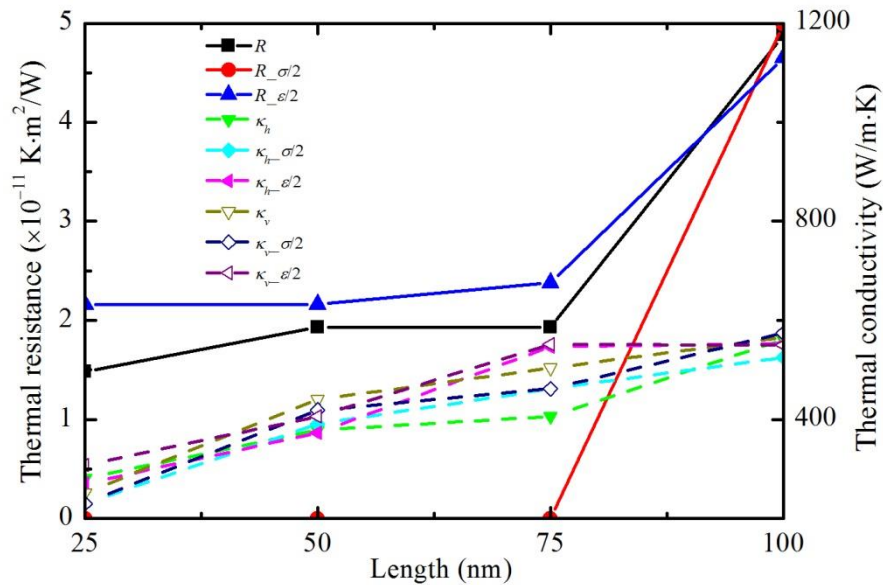


Figure 3.8. Thermal resistance and thermal conductivity comparison with ε and σ reduced to half separately. It is observed that when σ is reduced to half, the R values are suppressed to zero for the 25.0 nm, 50.1 nm and 75.0 nm cases. While when ε is reduced to half, the R values just change slightly. The thermal conductivities vary in a small range when different ε or σ are used and increase with the GNR length. All the results are without quantum corrections.

Since the potential walls are fixed in position (motionless), no external work will be done to the walls or to the GNR system, i.e., there are no energy exchange between the GNR and the LJ walls. And this is the most important difference between the LJ wall

and a substrate. The thermal conductivity of a supported graphene will decrease due to the out-of-plane (ZA) phonon scattering and energy coupling with the substrate. However, when the graphene is sandwiched between structureless LJ potentials, the phonons will have specular reflections on the walls. This specular reflection of phonons will not affect the thermal conductivity and thermal resistance of graphene. Nevertheless, the application of the LJ walls will affect the phonon dispersion relations of graphene and different choices of ε and σ could lead to different phonon energy distributions in the sandwiched GNRs. Under such scenario, the existence of potential walls will affect the calculated thermal conductivities and thermal resistances. From above discussions, it is conclusive that the LJ walls used in this work affect the calculated thermal properties of bended GNR to a very limited extent.

Extra calculations have been done to elaborate on the above explanations. The ε and σ values of the 9-3 LJ potential are reduced to half ($\varepsilon=0.00142$ eV, $\sigma=0.17$ nm) separately to compare the thermal resistance (R) and thermal conductivity (κ_h and κ_v) change with previous cases (right-angle bended). The comparison results are shown in Fig. 3.8. Firstly, it is observed that the parameter σ plays a more important role than ε on the determination of bended GNR's thermal resistance. For example, when σ is reduced to half, thermal resistances of the 25.0, 50.1 and 75.0 cases are suppressed to zero, yet when ε is reduced to half, the R values remain almost the same. It is known that in the 9-3 LJ potential $E_p = \varepsilon[2/15(\sigma/r)^9 - (\sigma/r)^3]$, ε stands for the depth of the weakly

attractive well and σ represents the separation distance at which the LJ potential changes sign. When σ is reduced to half, the first and second parts in the bracket are reduced to 0.002 and 0.125 times their original values separately. While when ε is reduced to half, the E_p value just changes by 0.5. Therefore, it is clear to see that the strength of the LJ potential is more sensitive to σ . Thermal conductivities of the horizontal (κ_h) and vertical (κ_v) parts of the bended GNRs are also calculated with different ε and σ values. It is found that the thermal conductivities do not change much with either ε or σ reduced to half. Take the 2.0×100.0 nm² GNR as an example, by only reducing σ to 0.17 nm, the thermal conductivity for the horizontal part of the 100.0 nm bended GNR changes from 561 W/m·K to 525 W/m·K while the thermal conductivity for the vertical part changes from 565 W/m·K to 574 W/m·K. The thermal resistance in the bended region changes from 4.88×10^{-11} K·m²/W to 4.99×10^{-11} K·m²/W. By only reducing ε to 0.00142 eV, the thermal conductivity becomes 553 W/m·K and 550 W/m·K for the horizontal and vertical parts, and the thermal resistance in the bended region is 4.65×10^{-11} K·m²/W. The κ_h and κ_v values with half ε or σ values are shown in Fig. 3.8. The thermal resistance and thermal conductivity values are without quantum corrections. Therefore, it is conclusive that the change of 9-3 LJ potential parameters does not make a substantial effect on the phonon thermal transport in bended GNR, unless a very strong wall potential and very narrow wall-GNR distance is used. The LJ potential wall's effect on the thermal conductivity of flat GNRs is also investigated systematically. The 25.0 nm and 50.1 nm flat GNRs are used to calculate the phonon energy distributions with $\varepsilon=0.00142$ eV and

$\sigma=0.17$ nm. Compared with previous cases, the thermal conductivity of the 25.0 nm flat GNR changes from 355 W/m·K to 325 W/m·K after the ε and σ are reduced by 50%. As for the 50.1 nm flat GNR, the thermal conductivity just changes very little: from 399 W/m·K to 393 W/m·K. From the above comparisons, it is concluded that the 9-3 LJ potential walls applied in this work do not have substantial effect on the thermal transport in bended or flat GNRs.

CHAPTER 4. PHONON ENERGY INVERSION IN GRAPHENE DURING TRANSIENT THERMAL TRANSPORT

This work reports on the phonon energy evolution in graphene nanoribbons during transient thermal transport. Phonon energy inversion is observed: after initial localized thermal excitation, the energy of initial cold phonons (flexural mode: FM) becomes higher than that of local hot phonons in the in-plane direction (longitudinal and transverse modes: LM and TM). This energy inversion holds for about 50 picoseconds. Two physical factors combine together to give rise to this phenomenon. One is the much faster heat conduction by FM phonons than that by LM/TM phonons. This process induces a large energy difference between FM and LM/TM phonons. The other factor is that the energy exchange rate between FM and LM/TM phonons increases with their temperature: $3.7 \times 10^{10} \text{ s}^{-1}$ at 84 K to $20.3 \times 10^{10} \text{ s}^{-1}$ at around 510 K. This gives rise to a fast energy flow from LM/TM to FM phonons in the hot region and slow energy flow back from FM to LM/TM phonons in the cold region. The energy inversion becomes weaker with the increasing layer number of graphene. Our observation points out a novel way for temporal energy storage in FM phonons, energy conversion and isolation.

4.1. Results and discussion

4.1.1. Phonon energy inversion after localized phonon excitation

First of all, we study the phonon energy evolution after localized phonon excitation in a graphene nanoribbon (GNR) as shown in Fig. 4.1(a). A single layer GNR

with dimensions of $2.0 \times 25.0 \text{ nm}^2$ ($x \times y$) is constructed. The second generation of Brenner potential [29]: reactive empirical bond-order (REBO), based on the Tersoff potential [34, 63] with interactions between C-C bonds is applied in our MD simulation reported in this paper.

Periodic boundary condition is applied to the y direction and free boundary conditions are applied to the x and z directions. To compare the energy evolution of different phonon modes and the whole system, a quantity defined as $E_k/[(1/2)k_B]$, where E_k is kinetic energy and k_B is Boltzmann constant, with unit K is used to represent the energy values in each direction and a value $E_k/[(3/2)k_B]$ with unit K stands for the system's total energy. "Bias" has been removed from the atomic velocities when energies are calculated. During initial system equilibrium calculation, a time step of 0.5 fs is used. After 150 ps energy equilibrium calculation, the system reaches the expected steady state at 50 K. Then two layers of carbon atoms at each end in the x direction are grouped to apply opposite stretching forces (F) to each atom for 25 fs. The stretching force is $1.0 \text{ eV}/\text{\AA}$ per atom. Atomic structure of the system is depicted in Fig. 4.1(a). The GNR system is left to relax for the next 100 ps until it reaches energy equilibrium again. The time step is reduced to 0.05 fs in these phonon excitation and relaxation processes in anticipation to capture detailed phonon energy evolution.

Due to the displacement of the outermost carbon atoms, a phonon package is excited and propagates to the inside from each boundary in the x direction.

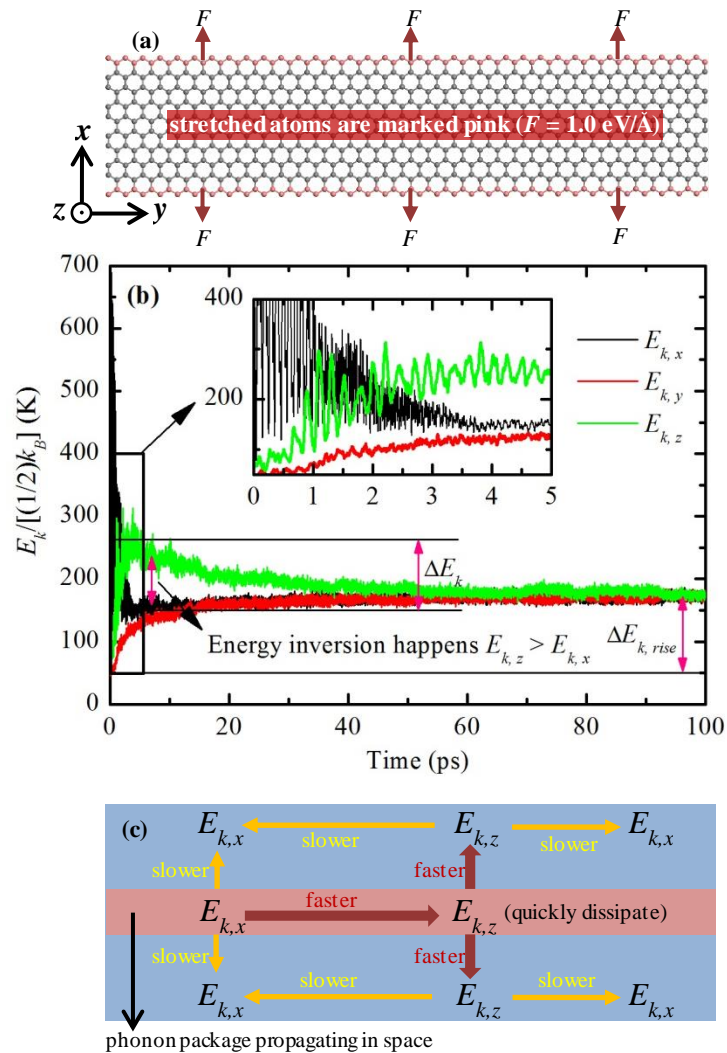


Figure 4.1. Atomic configuration and energy inversion characterization in the 2.0×25.0 ($x \times y$) nm^2 GNR system. (a) Periodic boundary condition is applied to the y direction and free boundary conditions are applied to the x and z directions. The two outermost layers of atoms in the x direction (marked as pink) are grouped to apply the stretching force ($F = 1.0 \text{ eV/\AA}$). This coordinate system is used for all the discussions in this work. (b) The $E_{k,x}$, $E_{k,y}$ and $E_{k,z}$ profiles of the GNR after 25 fs phonon excitation at the boundary. (c) The $E_{k,x}$ and $E_{k,z}$ energy exchange after the GNR is stretched in the width direction. The red area represents phonon package propagations induced by the stretch.

Temperatures of the path through which the phonon package propagates will

become higher than the rest areas, which gives rise to moving local hot regions in the GNR. Due to the phonon excitation in the x direction, the average energy of the system increases from 50 K to 194 K immediately after excitation. To take a closer look at the energy relaxation process, energies of phonons in all three directions ($E_{k,x}$, $E_{k,y}$, $E_{k,z}$) are computed and shown in Fig. 4.1(b). The results are averaged every 100 steps to suppress the data noise. At the end of excitation, $E_{k,x}$, $E_{k,y}$ and $E_{k,z}$ are 478 K, 48 K and 57 K respectively. This clearly shows that the excitation almost solely increases the energy of phonons in the x direction while the y and z mode phonons stay cold. Since the energy of the longitudinal phonons ($E_{k,x}$) is much higher than the other two modes ($E_{k,y}$, $E_{k,z}$), energy exchange among the three phonon branches will occur continuously until the GNR system reaches energy equilibrium again.

Generally, one would expect in such scenario $E_{k,y}$ and $E_{k,z}$ will increase gradually, and $E_{k,x}$ will decrease until the three phonon mode energies reach the same level. However, according to our calculated results, the longitudinal phonon energy ($E_{k,x}$) decreases dramatically at the beginning of the relaxation procedure while the flexural phonon energy ($E_{k,z}$) rises much faster than the transverse phonon energy ($E_{k,y}$) and becomes higher than $E_{k,x}$ at around 2.0 ps. It is seen that the energy exchange between $E_{k,x}$ and $E_{k,y}$ does not give rise to such inversion phenomenon, and they reach the same level after about 15 ps. On the other hand, at the moment $E_{k,z}$ reaches its peak value, $E_{k,x}$ also reaches its minimum, and the energy inversion ($E_{k,x}-E_{k,z}$) reaches the highest level. Then energy flows back from $E_{k,z}$ to $E_{k,x}$ and $E_{k,y}$, and it takes a much longer time (~50

ps) for them to reach the same level. This points out that the energy exchange between $E_{k,x}$ and $E_{k,z}$ is much slower than that between $E_{k,x}$ and $E_{k,y}$, agreeing with our previous observation in studying the temporal response of a GNR to a thermal impulse [28].

First of all, for this first-time observed surprising behavior in graphene, our speculation of the driving force behind it is the much higher thermal transport capability by the flexural (z) mode phonons. As illustrated in Fig. 4.1(c), phonon energies in the moving local hot regions of GNR will increase dramatically when the phonon package propagates in the lateral direction. This high local energy will induce a high local $E_{k,z}$. According to Lindsay *et al.* [26], for a suspended SLG, the ZA phonon mode has a large density of states and follows a selection rule for anharmonic phonon scattering, which contributes to its anomalously large thermal conductivity. Therefore, due to the large thermal conductivity of ZA phonons, the local flexural mode energy ($E_{k,z}$) will dissipate in space very fast, which allows the local $E_{k,x}$ to always remain higher than $E_{k,z}$. Consequently in the local hot regions, thermal energy keeps flowing from $E_{k,x}$ to $E_{k,z}$, while in the whole GNR system $E_{k,z}$ becomes greater than $E_{k,x}$. One argument is that in regions where $E_{k,z} > E_{k,x}$, energy will flow back from $E_{k,z}$ to $E_{k,x}$, and offset the energy flow from $E_{k,x}$ to $E_{k,z}$ in the regions of $E_{k,x} > E_{k,z}$. We will prove later that this energy flow back is much slower due the fact that the $E_{k,x}$ - $E_{k,z}$ coupling is weaker when the local temperature is lower [Fig. 4.1(c)]. Energy transfer rates among the three mode phonons will be discussed below to give detailed physical analysis of this process.

4.1.2. Phonon package propagation and phonon coupling

From the inset of Fig. 4.1(b) we clearly see that $E_{k,x}$ decreases in a sinusoidal pattern (oscillating). This is caused by the phonon package travelling and reflections at the x boundaries. To better analyze the phonon package propagation and energy exchange in the GNR, we plot its spatiotemporal contours in respect of $E_{k,x}$, $E_{k,y}$ and $E_{k,z}$ in Figs. 4.2(a), (b) and (c) respectively. The results are presented without any data average. It can be seen that the longitudinal (x) phonon packages are travelling between the two x boundaries and the wave amplitude decays with time due to the energy transfer and phonon scattering. The propagation speed of the longitudinal phonon package is calculated at 19.9 km/s.

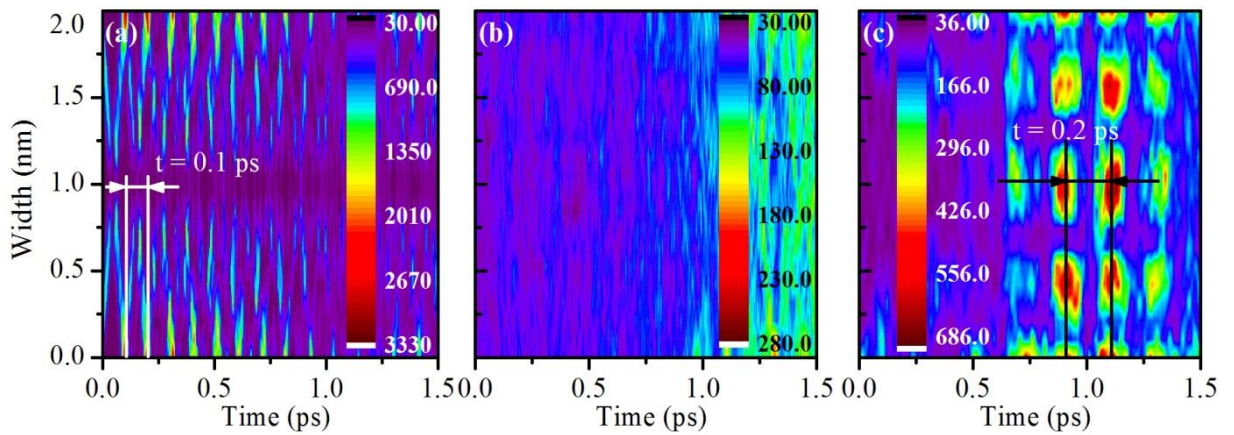


Figure 4.2. Phonon package propagations in the width direction of the 2.0×25.0 ($x \times y$) nm^2 GNR system. (a), (b) and (c) are for the spatial-energy contours of $E_{k,x}$, $E_{k,y}$ and $E_{k,z}$ respectively.

The local energies at the boundary where the phonons are reflected are higher than those at the other places due to the overlap of incident and reflection waves which

amplifies the wave amplitude. The local energies in the center are lower since the phonon packages from opposite directions cancel out and weaken the local lattice vibration. No transverse (y) phonon package propagation is observed in Fig. 4.2(b). In Fig. 4.2(c), flexural (z) phonon package propagation is observed. In Fig. 4.2(a), we calculate the period of the longitudinal phonon package to be 0.1 ps, corresponding to a phonon moving back and forth frequency of 10 THz. In Fig. 4.2(c), the period for the flexural phonon package is calculated at 0.2 ps, which corresponds to a phonon moving back and forth frequency of 5 THz.

We developed a speculation that the energy inversion in GNR is caused by phonon package propagations, which create moving hot local regions where the thermal energies keep transferring from the in-plane to out-of-plane phonons until the phonon package dies out. The key point for such energy inversion is very localized phonon excitation. Therefore if there is no phonon package generated in the GNR system, the energy inversion should not be observed among $E_{k,x}$, $E_{k,y}$ and $E_{k,z}$. To test this point, we use a $2.0 \times 25.0 \text{ nm}^2$ ($x \times y$) GNR to investigate the energy transfer among the three phonon branches without inducing any phonon propagation influence.

The GNR system is initially placed in a Nose-Hoover [81, 82] thermal bath for 200 ps until the system reaches energy equilibrium at 50 K. Then the velocity of atoms in the x direction (v_x) is rescaled to two times their original values. Therefore according to the energy equipartition theorem, the x mode phonon energy ($E_{k,x}$) will become four

times the initial value, which is around 200 K in this case. Due to the increase of $E_{k,x}$, thermal energies will be transferred to $E_{k,y}$ and $E_{k,z}$, and no phonon package is generated since the GNR is heated uniformly in the x direction.

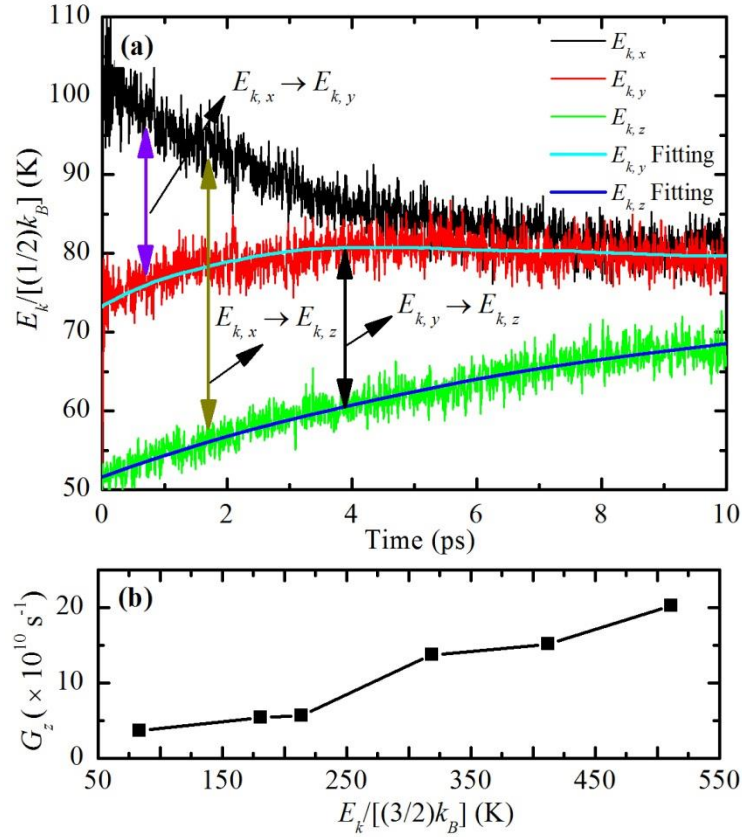


Figure 4.3. Calculation of phonon coupling time against energy. (a) Energy evolutions after $E_{k,x}$ is rescaled to ~ 200 K. (b) The characteristic coupling time of the in-plane phonons and the flexural phonons at different energy levels. It is conclusive G_z increases with the local energy level, meaning if the phonon is more excited, the mode-wide coupling will be stronger.

The energy relaxation process is shown in Fig. 4.3(a). The time step is 0.05 fs during the relaxation and the results are averaged every 100 steps to suppress the data

noise. Compared with Fig. 4.1(b), it is seen that no energy inversion happens between in-plane and out-of-plane phonon energies.

In Fig. 4.3(a), three energy transfer processes are observed, which are $E_{k,x} \rightarrow E_{k,z}$, $E_{k,y} \rightarrow E_{k,z}$ and $E_{k,x} \rightarrow E_{k,y}$ respectively. The evolution of $E_{k,z}$ can be expressed as

$$\frac{\partial E_{k,z}}{\partial t} = G_{xz} (E_{k,x} - E_{k,z}) + G_{yz} (E_{k,y} - E_{k,z}), \quad (4-1)$$

where G_{xz} , G_{yz} are the inverse values of the coupling time for $E_{k,x} \rightarrow E_{k,z}$ and $E_{k,y} \rightarrow E_{k,z}$. Since $E_{k,x}$ and $E_{k,y}$ are both in-plane phonon energies, to simplify the coupling analysis we assume their coupling times with $E_{k,z}$ are the same ($G_{xz} = G_{yz} = G_z$). The theoretical basis of Eq. (4-1) could be explained by the following. After the v_x rescaling, the total energy of the system remains constant while $E_{k,x}$, $E_{k,y}$ and $E_{k,z}$ are different, i.e., there is no spatial heat conduction in the system but energy transfer among different phonon modes. The change in certain phonon energy is only caused by its coupling with other phonon modes. The phonon energy exchange happens as long as there are energy differences among them. Take $E_{k,z}$ as an example, the change of $E_{k,z}$ is caused by its coupling with $E_{k,x}$ and $E_{k,y}$. To describe this change, coefficients of G_{xz} and G_{yz} with unit second^{-1} are introduced to characterize the coupling rate of $E_{k,z}$ with $E_{k,x}$ and $E_{k,y}$ respectively. Then the evolution of $E_{k,z}$ can be described by calculating the time integration of its coupling rate with $E_{k,x}$ and $E_{k,y}$. Since $E_{k,z}$ is already given by the MD simulation results, G_z can be determined by best fitting the MD results using Eq. (4-1). Given a proper G_z value, Eq. (4-1) could be used to fully describe the evolution of $E_{k,z}$. By fitting the MD simulation data of $E_{k,z}$ with numerical results calculated from Eq. (4-

1) using the least square method, we calculate the G_z value at $3.96 \times 10^{10} \text{ s}^{-1}$, corresponding to a coupling time (τ_z) of 25.3 ps. Similarly, the equation for the evolution of $E_{k,y}$ is

$$\frac{\partial E_{k,y}}{\partial t} = G_{xy}(E_{k,x} - E_{k,y}) + G_z(E_{k,z} - E_{k,y}), \quad (4-2)$$

where G_{xy} is the inverse of the coupling time between $E_{k,x}$ and $E_{k,y}$. Given $G_z = 3.96 \times 10^{10} \text{ s}^{-1}$, the value of G_{xy} is calculated at $1.86 \times 10^{11} \text{ s}^{-1}$ based on data fitting of the $E_{k,y}$ evolution, and the phonon relaxation time (τ_{xy}) is 5.4 ps. From the above results, we can see that τ_z is 4.7 times τ_{xy} , meaning the energy transfer for $E_{k,x} \rightarrow E_{k,z}$ and $E_{k,y} \rightarrow E_{k,z}$ are much slower than that between $E_{k,x}$ and $E_{k,y}$.

According to the previous study by Lee *et al.* [74], the thermal conductivity of graphene decreases with temperature. It is expected the characteristic coupling time between in-plane and out-of-plane phonons will decrease with time, which should lead to an increasing G_z value against temperature in graphene. Therefore we also conducted a study on how the phonon coupling constant G_z changes with the local energy level (temperature). For this study, we rescale $E_{k,x}$ and $E_{k,y}$ simultaneously to the same value and use Eq. (4-1) to calculate G_z . The G_z values at different energies are shown in Fig. 4.3(b). We can see that G_z increases with temperature, from around $3.7 \times 10^{10} \text{ s}^{-1}$ at 84 K to $20.3 \times 10^{10} \text{ s}^{-1}$ at around 510 K. This indicates that the thermal energy transport between the in-plane and out-of-plane phonons becomes faster as temperature increases, meaning the phonon coupling between $E_{k,x}/E_{k,y}$ and $E_{k,z}$ in hot local regions is stronger

than that in cold regions. From the above discussions, we conclude that the energy inversion in GNR is mainly caused by two reasons. First, the out-of-plane phonons make substantial contribution to the GNR's thermal conductivity and dissipate heat much faster than the in-plane phonons. Second, in the moving hot local regions where the phonon package passes by, the coupling time between in-plane and out-of-plane phonons is much smaller than that in the cold area. This leads to a continuous net energy transfer from $E_{k,x}/E_{k,y}$ to $E_{k,z}$.

From above work, we have learned that energy inversion will happen when a phonon package is excited in the x direction. However, since the thermal conductivity and phonon boundary scattering rate in the x and y directions are different, it is necessary to further examine the phonon energy evolution when the phonon package is excited in the y direction. A $2.0 \times 25.0 \text{ nm}^2$ ($x \times y$) flat GNR is built to reach thermal equilibrium at temperature 50 K. Periodic boundary condition is applied to the x direction and free boundary conditions are applied to the y and z directions. Then two layers of carbon atoms at one end in the y direction are grouped to apply a stretching force (F in the y direction) for 25 fs. The stretching force is 5.0 eV/\AA per atom. Atomic structure of the system is shown in the inset of Fig. 4.4. Phonon energy evolutions in each direction are shown in Fig. 4.4. The time step is 0.05 fs during the relaxation and the results are averaged every 100 steps to suppress the data noise. It is observed that right after the phonon package excitation, $E_{k,y}$ becomes higher than $E_{k,x}$ and $E_{k,z}$. Then at $\sim 18 \text{ ps}$, $E_{k,z}$ exceeds $E_{k,y}$ to become the highest, which indicates the occurrence of energy inversion.

An energy bump at ~ 1.25 ps is observed in the $E_{k,y}$ profile. The energy bump is induced by the longitudinal phonon package's reflection on the other end in the y direction, which increases the atoms' kinetic energy in the local area. Based on the appearance time of this energy bump, the longitudinal phonon package speed is calculated at 20.0 km/s, which is nearly the same with previous result of 21.3 km/s [19].

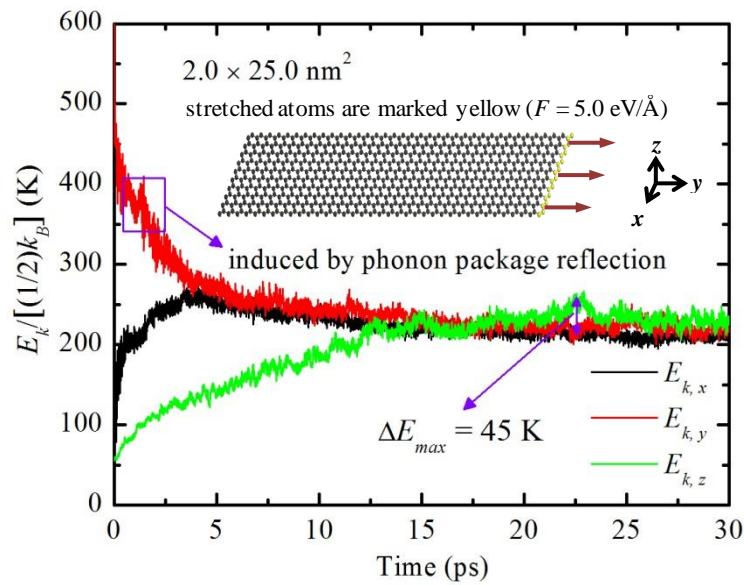


Figure 4.4. Energy inversion characterization in the GNR system with phonon package excitation in the y direction. Periodic boundary condition is applied to the x direction and free boundary conditions are applied to the y and z directions. Two outermost layers of carbon atoms at the right end (marked as yellow) are grouped to apply stretching force ($F = 5.0$ eV/Å). An energy bump is observed in the $E_{k,y}$ profile, which is induced by the phonon package reflection on the graphene boundary.

4.2. Energy inversion with a static heat source

From the above physics analysis, we predict that phonon energy transfer and

exchange caused by a static localized heating source will also induce energy inversion in a GNR system. To prove our prediction, a $2.0 \times 75.1 \text{ nm}^2$ ($x \times y$) GNR system is built [Fig. 4.5(d)]. Periodic boundary condition is applied to the y direction and free boundary conditions are applied to the x and z directions.

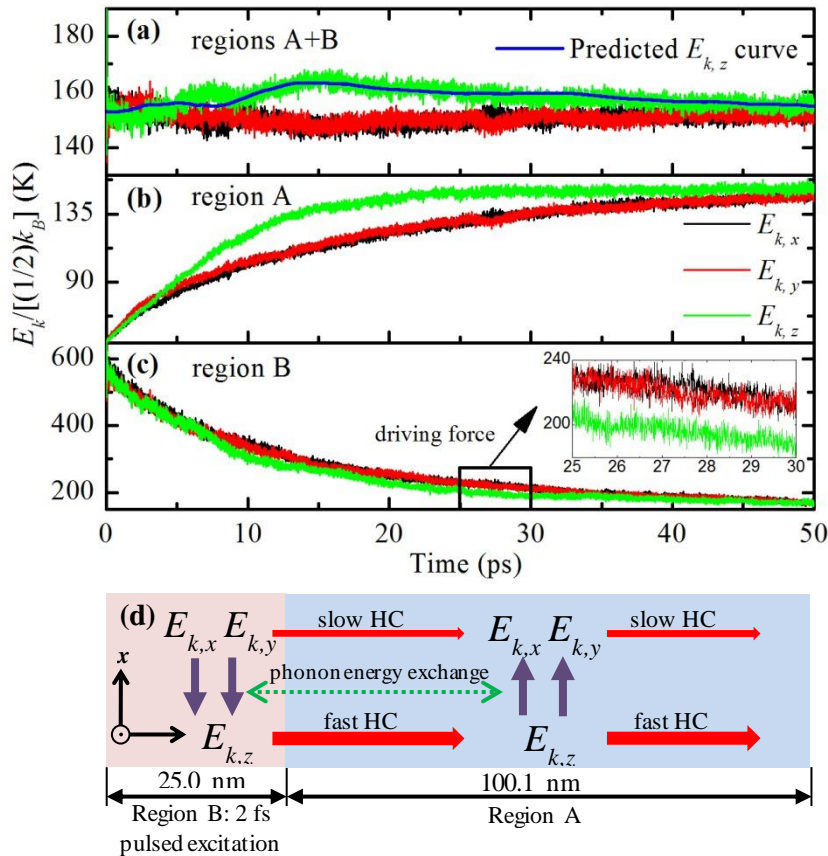


Figure 4.5. Energy inversion characterization with static heating source. Fix boundary condition is applied to the y direction and free boundary conditions are applied to the x and z directions. (a), (b) and (c) show energy evolutions of the whole region, regions A, and region B. (d) Schematic to show the phonon transport in the 2.0×125.1 ($x \times y$) nm^2 GNR. Heat conduction (HC) among FM phonons is much faster than those among LM and TM phonons. The red area (region B) is the 25.0 nm heating region where $E_{k,x}$ and $E_{k,y}$ transfer to $E_{k,z}$. The thermal energies will mainly be transported by $E_{k,z}$ to the low energy area (region A) where $E_{k,z}$ mostly transfers to itself in space (heat conduction) and partially to $E_{k,x}$ and $E_{k,y}$.

The system initially reaches thermal equilibrium at 50 K. Then a region of $2.0 \times 25.0 \text{ nm}^2$ [region B shown in Fig. 4.5(d)] in the middle of the GNR is exposed to a thermal impulse. The heating time is 2 fs and the final temperature in the heating region is 631 K. Figures 4.5(a), (b) and (c) show the energy evolutions of the whole system, regions A+C, and region B. The time step is 0.5 fs during the relaxation and the results are presented without any data average. First and most importantly, energy inversion is observed in Fig. 4.5(a). At around 1 ps, the flexural mode (FM) phonon energy ($E_{k,z}$) becomes higher than those of the transverse mode (TM) ($E_{k,x}$) and longitudinal mode (LM) ($E_{k,y}$) phonons. It can be seen from Fig. 4.5(c) that in region B, $E_{k,z}$ decreases faster than $E_{k,x}$ and $E_{k,y}$. This is because the FM phonon carries more heat to the low energy region (regions A and C) than the TM and LM phonons due to the much higher thermal conductivity sustained by FM phonons. As a result, $E_{k,z}$ regions A and C is higher than $E_{k,x}$ and $E_{k,y}$ due to the continuous heat current from region B by FM phonons, which is clearly shown in Fig. 4.5(b).

In region B, the LM and TM phonons keep transferring thermal energy to the FM phonons due to the energy difference between them, as shown in the inset of Fig. 4.5(c). This continuous heat transfer between the in-plane phonons and out-of-plane phonons eventually causes higher total energies in the z direction and induces energy inversion in GNR. During the heat conduction from region B to regions A and C, the FM phonons will largely transfer their energy to FM phonons (heat conduction), and transfer very little to the LM and TM phonons. One argument is that in regions A and C, the FM

phonons have a higher energy than the LM and TM phonons, so the energy could be transferred from FM phonons to LM and TM phonons in this region. This could prevent the energy inversion from happening. The fact is that in region B, the local energy is higher and will lead to faster LM/TM to FM phonon energy transfer (smaller coupling time). In regions A and C, the local energy is low, and the energy transfer from FM to LM and TM phonons is slow (longer coupling time). Therefore, more energy will stay in the FM phonons, leading to energy inversion.

The energy transport rate from the TM and LM phonons to the FM phonons in region B is expressed as

$$E'_{z,in} = G_{z1}(E_{k,x} - E_{k,z}) + G_{z1}(E_{k,y} - E_{k,z}), \quad (4-3)$$

where $E_{k,x}$, $E_{k,y}$, $E_{k,z}$ are the phonon energies in the 25.0 nm region. Similarly, the energy transport rate from the FM phonons to the TM and LM phonons in region A can be written as

$$E'_{z,out} = G_{z2}(E_{k,z} - E_{k,x}) + G_{z2}(E_{k,z} - E_{k,y}). \quad (4-4)$$

The differences between $E'_{z,in}$ and $E'_{z,out}$ will be the rate of energy accumulating in the flexural phonons. The FM phonon energy profile of the whole system can be predicted as

$$E_{k,z} = \frac{V_B \int E'_{z,in} dt - V_A \int E'_{z,out} dt}{V_{GNR}}, \quad (4-5)$$

where V_A , V_B and V_{GNR} represent the volume of region A, region B and the entire GNR respectively. The G_{z1} and G_{z2} values will change with energy as shown in Fig. 4.3(b),

while in this case we simplify the calculation by using $G_{z1} = 22 \times 10^{10} \text{ s}^{-1}$ and $G_{z2} = 4.15 \times 10^{10} \text{ s}^{-1}$ at the average FM energy for the time range 0-15 ps, and $G_{z1} = 14.5 \times 10^{10} \text{ s}^{-1}$ and $G_{z2} = 5.3 \times 10^{10} \text{ s}^{-1}$ for the time range 15-50 ps. By substituting $E_{k,x}$, $E_{k,y}$ and $E_{k,z}$ values into Eqs. (4-3)-(4-5), the predicted $E_{k,z}$ values is plotted in Fig. 4.5(a) (blue solid curve). It is very exciting to observe that the predicted $E_{k,z}$ curve soundly matches the MD simulation results. This strongly proves that the input energy to the FM phonons is greater than the output energy, therefore inducing energy inversion in GNR. Also this prediction quantitatively proves the physics we proposed for the energy inversion phenomenon.

4.3. Energy inversion in multi-layer graphene

Klemens [21, 22] clearly distinguished the thermal transport in SLG and in bulk graphite. In the latter case there appears strong coupling within the cross-plane phonon modes and heat propagates in all directions, which reduces the contributions to heat conduction of the low-energy modes along the basal planes to negligible. By following the spirit of Klemens [21, 22], Balandin *et al.* [20] proved that thermal conductivity of bulk graphite is much lower than that of single layer graphene. According to Lindsay *et al.* [27], the interaction between graphene layers breaks the selection rule on phonon-phonon scattering and results in a reduced thermal conductivity in the ZA phonon mode. As a result, we expect that the energy inversion in GNR will also be weakened in multilayer graphene (MLG).

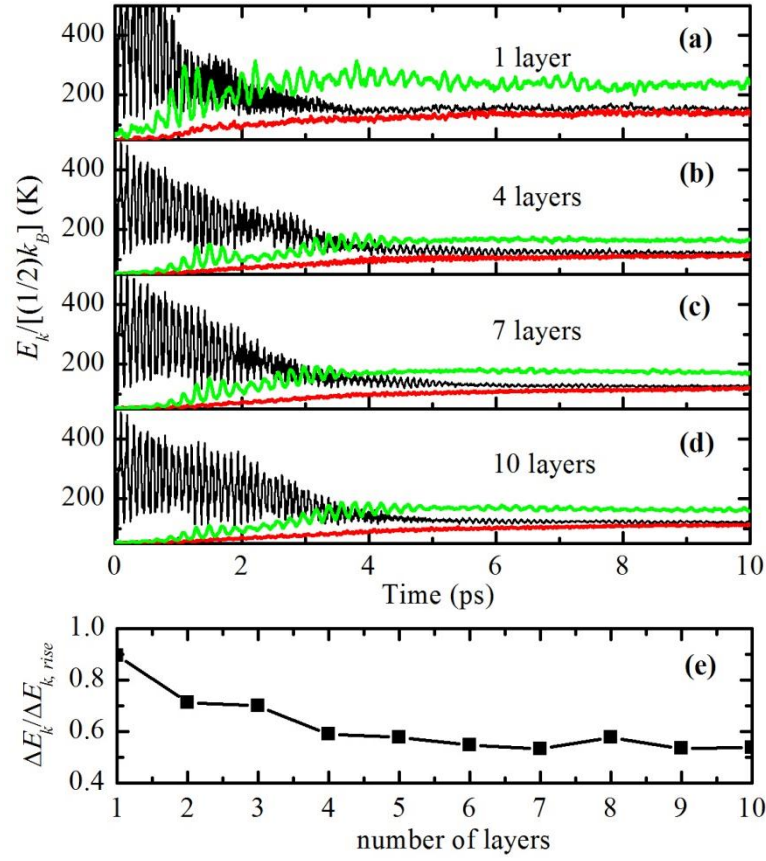


Figure 4.6. Damping energy inversion against growing layers. (a), (b), (c) and (d) show energy evolutions for graphene with different layer numbers. The black, red and green solid lines represent $E_{k,x}$, $E_{k,y}$ and $E_{k,z}$ respectively. (e) $\Delta E_k / \Delta E_{k, rise}$ with different layer numbers from 1 to 10. Definitions of ΔE_k and $\Delta E_{k, rise}$ are illustrated in Fig. 4.1(b).

For the MLG systems studied in this work, the interaction between graphene layers is described by the Lennard-Jones (LJ) potential as

$$v_{LJ}(r) = 4\epsilon \left[\left(\frac{\sigma}{r} \right)^{12} - \left(\frac{\sigma}{r} \right)^6 \right], \quad (4-6)$$

where r is the distance between carbon atoms and ϵ and σ are the common LJ parameters, which are set to be 0.0046 eV and 3.3276 Å respectively. Only the coupling

between adjacent graphene planes is included in all the systems.

Dimension of the MLG system is 2.0 nm×25.0 nm ($x \times y$), with n number of graphene layers in the z direction. Coordinates and boundary conditions of the system are the same as that displayed in Fig. 4.1(a). A time step of 0.5 fs is used along the whole calculation. After energy equilibrium calculation at 50 K, the MLG system is stretched in the x direction (2.0 nm side direction) with two opposite forces (1.0 eV/Å per atom) applied on each side for 25 fs. Only the outmost two layers of atoms at each end in the x direction are stretched, like the scenario shown in Fig. 4.1(a). After the stretching process, energy relaxation is performed for the next 100 ps. Energy changes in all three phonon modes are calculated during the relaxation process and the results for $N = 1, 4, 7, 10$ MLGs are shown in Figs. 4.6(a), (b), (c) and (d). The results are presented without any data average. We can see from these figures that as the layer number increases, the maximum $E_{k,z}$ decreases and energy inversion is weakened. To be more specific, we calculate the $E_{k,z}$ difference between the initial and the final state as the denominator ($\Delta E_{k,rise}$) and the difference between the peak $E_{k,z}$ value and the minimum $E_{k,x}$ value as the nominator (ΔE_k). The ΔE_k and $\Delta E_{k,rise}$ value definition is denoted in Fig. 4.1(b). ΔE_k is the maximum energy inversion between $E_{k,z}$ and $E_{k,x}$, and $\Delta E_{k,rise}$ is the final system energy rise induced by the initial phonon excitation. The ratio reflects the strength of the energy inversion process and their values are plotted in Fig. 4.6(e). The $\Delta E_k/\Delta E_{k,rise}$ values decrease with an increasing layer number, which further proves that the energy inversion is weakened as layer numbers increase. This weakening is most obvious when

the graphene layer number changes from 1 to 2, and is moderate with further layer number increases. We conclude from Fig. 4.6(e) that energy inversion is weakened due to a reduced FM mode thermal conductivity in the MLG. Due to the computational cost for multilayer graphene, our calculations only include layer thickness ranges from 1 to 10. However, for much thicker ones, we expect the energy inversion phenomenon will still exist but be much weaker. We believe this is an intrinsic property of graphite. However, this energy inversion phenomenon is not a 2-D effect. To observe the energy inversion at the system level, the material must have strong mode-wide non-uniform thermal conductivity and temperature-dependent inter-mode energy coupling rate.

CHAPTER 5. CO-EXISTING HEAT CURRENTS IN OPPOSITE DIRECTIONS IN GRAPHENE NANORIBBONS

The differential form of Fourier's law of heat conduction is expressed as $q'' = -\kappa \nabla T$, where q'' is the local heat flux, κ the material's thermal conductivity and ∇T the temperature gradient. The minus sign indicates the heat current flows from higher temperature regions to lower ones. For bulk materials, κ is size independent and only determined by the material's composition and structure. While for micro/nanoscale materials, κ is also affected by parameters like dimension and boundary condition. Generally, in order to define the local temperature, mode-wide thermal equilibrium among different phonon modes should be reached. However, since the thermal conductivities of different phonon modes in graphene have huge differences, it is possible that there is mode-wide energy difference during steady state heat conduction in graphene. In such scenario, the definition of temperature is no longer accurate to describe graphene's local energy level. And strictly speaking, thermal conductivity is also not well defined. Therefore, a nominal temperature (E_T) with unit K and apparent thermal conductivity (κ_{app}) with unit W/m·K are brought up to give a better description.

In this work, phonon thermal transport in GNRs is investigated by using MD simulation. A peculiar heating and cooling technique is developed to induce mode-wide energy difference during steady state heat conduction. The unique thermal properties of GNR enable it to support a bi-directional heat transfer in the system. And when the bi-directional heat conduction reaches steady state, a single thermal conductivity cannot be

used to reflect the relation between the heat flux and the temperature gradient. The calculated thermal conductivities are dependent on the net heat fluxes and the κ_{app} of graphene are calculated at positive, negative, zero and infinite values, depending on the proportions of each phonon mode energy added/subtracted to/from the heating/cooling areas.

5.1. Basis of physical problem and modeling

The second generation of Brenner potential:[29] reactive empirical bond-order (REBO), based on the Tersoff potential[34, 63] with interactions between C-C bonds is applied in our MD simulation. In this work, the GNR systems have zigzag boundaries in the width direction and armchair boundaries in the length direction. The edge carbon atoms are not hydrogen-passivated. Atomic configuration of the GNR system is depicted in Fig. 5.1. The outermost layer of carbon atoms at each end (denoted in black) are fixed to avoid the spurious global rotation of the GNRs in the simulation. [83] Free boundary conditions are applied to the x and z directions. To compare the energy evolution of different phonon modes and the whole system, a nominal temperature E_i defined as $E_{k,i}/(1/2)k_B$ with unit K is used to represent the energy values in each phonon mode and a value E_T defined as $E_{k,T}/(3/2)k_B$ with unit K stands for the system's total energy. Here $E_{k,i}$ is the kinetic energy of carbon atoms for phonon mode i ($i=TM, LM, \text{ or } FM$); $E_{k,T}$ is the total kinetic energy of carbon atoms and k_B is the Boltzmann constant. Within the linear response regime, one would expect from Fourier's law of heat conduction that q'' changes proportionally with ∇T .

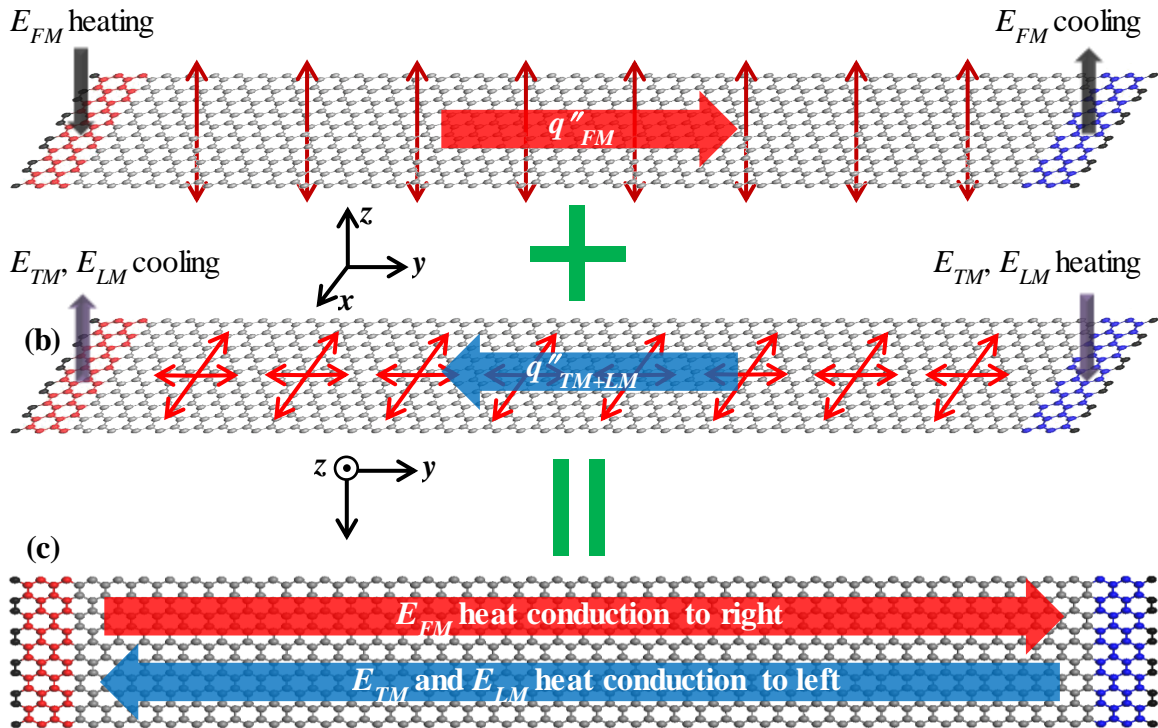


Figure 5.1. Atomic configuration for studying the bi-directional heat conduction in graphene nanoribbons. The outermost layer of carbon atoms at each end (denoted in black) are fixed in position. (a) Kinetic energy is added to the FM phonons on the left side (red region) and subtracted from the right side (blue region). Heat current q''_{FM} is carried by FM phonons from left to right. (b) The in-plane longitudinal and transverse phonons are heated and cooled on the right and left sides respectively. Heat current q''_{TM+LM} is carried by TM/LM phonons from right to left. (c) By doing (a) and (b) simultaneously, a peculiar bi-directional heat conduction phenomenon in GNR is created.

However, in many low dimensional systems,[84-88] it is found that q'' decreases with an increasing temperature bias (ΔT), which is known as negative differential thermal conductance (NDTC). Recent study by Hu *et al*[84] revealed a tunable NDTC in rectangular and triangular GNRs, which results from the competition between decreasing

κ and increasing ΔT beyond linear response regime. They proved that the NDTC in GNR is intrigued by its temperature dependent thermal conductivity. However, it is worth noting that the thermal conductivity of GNR is not only temperature dependent, but also deviates much among in-plane and out-of-plane directions.[23, 24, 26, 28]

Inspired by the strong mode-wide difference in sustaining thermal transport in GNR, bi-directional heat transfer in a rectangular GNR is explored in this work (as shown in Fig 5.1). Four layers of carbon atoms at each end of the GNR system is grouped to add/subtract kinetic energy to/from the out-of-plane phonon mode (E_{FM}) and in-plane phonon modes (E_{LM} and E_{TM}) respectively. In traditional non-equilibrium molecular dynamic methods for thermal conductivity calculation, the hot and cold regions are created in the simulation domain by adding kinetic energy ΔE_k in the hot region and removing the same amount from the cold one while preserving linear momentum at each time step. The velocity of each atom is rescaled by the same factor χ . In this work, we use a modified velocity rescaling method to control the energy variation for each phonon mode, i.e., instead of adding/subtracting kinetic energy to all phonon modes, we manage to add kinetic energy only to the specified phonon mode and subtract kinetic energy from the others in the same region. Specifically, by adding kinetic energy to E_{FM} while subtracting kinetic energy from E_{LM} and E_{TM} at the left end of GNR and doing the opposite at the right end, a bi-directional heat conduction phenomenon is observed. This physical process is demonstrated in Figs. 5.1(a), (b) and (c). The local nominal temperature along the GNR is calculated from the kinetic energy of the three

phonon modes averaged for 50 ps.

In this work, the phonon-phonon couplings among different phonon modes are considered in the graphene system naturally since the MD simulation tracks the full movement of each atom and the inter-atomic interaction. In our previous study.[89] it has been proved that the energy coupling between TM and LM phonons is much faster than that between TM/LM and FM phonons. At temperature ~ 80 K, it is calculated that the phonon relaxation time between FM and TM/LM is 4.7 times larger than that between TM and LM, meaning the energy transfer between TM/LM and FM is much slower than that between TM and LM. Also, it is concluded that the energy coupling between FM and TM/LM phonons is not constant against their energy level: the coupling becomes stronger when the phonon energy is higher.

5.2. Results and discussion

5.2.1. Negative apparent thermal conductivity in GNR

A GNR with dimensions of $2.0 \times 50.1 \text{ nm}^2$ ($x \times y$) is built. After 400 ps canonical ensemble (NVT) and 150 ps microcanonical ensemble (NVE) calculations, the system reaches thermal equilibrium at temperature 50 K. For FM phonons, kinetic energy $\Delta \dot{E}_{k,FM} = 2.17 \times 10^{-8} \text{ W}$ is added to the left end and subtracted from the right end of the GNR constantly for 400 ps, while $\Delta \dot{E}_{k,TM} + \Delta \dot{E}_{k,LM} = 1.96 \times 10^{-8} \text{ W}$ ($\Delta \dot{E}_{k,TM} = \Delta \dot{E}_{k,LM}$) is subtracted from the left TM+LM phonons and added to the right end TM+LM phonons

of the GNR respectively for the same time span. A parameter μ defined as $\Delta\dot{E}_{k,FM} / (\Delta\dot{E}_{k,TM} + \Delta\dot{E}_{k,LM})$ is used to represent the heating and cooling ratio between the out-of-plane and in-plane phonons. In this case, μ equals 1.11. For simplicity, the value $(\Delta\dot{E}_{k,TM} + \Delta\dot{E}_{k,LM}) = 1.96 \times 10^{-8}$ W ($\Delta\dot{E}_{k,TM} = \Delta\dot{E}_{k,LM}$) remains constant for all the heating and cooling cases reported in this work, and variations are made by changing $\Delta\dot{E}_{k,FM}$. Since the layer distance in graphite is 0.335 nm, we use this value as the thickness for single layer graphene for thermal conductivity evaluation.[90, 91] The cross-sectional area (A_c) is calculated at 6.7×10^{-19} m². Therefore the heat flux in the length direction can be calculated from the equation $q'' = Q/A_c$, from which the net heat flux is calculated as 3.23×10^9 W/m². The time step is 0.5 fs for all graphene calculations.

After 400 ps bi-directional heating and cooling process, the heat conduction reaches steady state. Then another 50 ps is calculated for data collection and average. Nominal temperature distributions along the GNR system are shown in Figs. 5.2(a), (b) and (c). Figure 5.2(a) shows the E_T energy distributions along the GNR while Figs. 5.2(b) and (c) are for the in-plane E_{TM}/E_{LM} and out-of-plane E_{FM} phonons respectively. First of all, we can see from Fig. 5.2(b) that E_{TM} and E_{LM} have a positive gradient, meaning heat flux is negative (from right to left) for these modes of phonon energy since the heat flux is driven by temperature/energy differentials. On the other hand, E_{FM} has a negative gradient, meaning its heat flux is going from left to right. This simultaneous bi-directional heat conduction is very unique, and proves, for the first time, that graphene as

a unique material can support two heat currents in opposite directions at the same time. The main mechanism behind this phenomenon is the weak energy coupling between E_{TM}/E_{LM} and E_{FM} , and the much higher thermal conductivity by FM phonons.

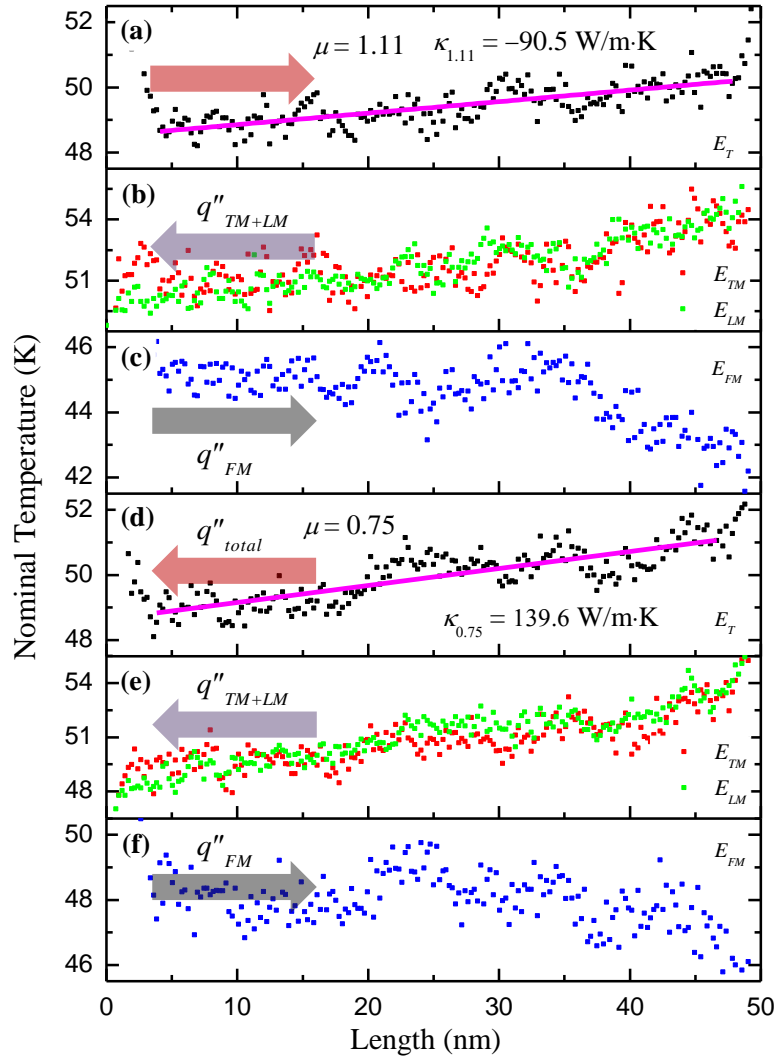


Figure 5.2. (a), (b), (c) Nominal temperature distributions for $\mu = 1.11$. q''_{total} follows the E_T increasing direction, indicating an apparent negative κ_{app} . (d), (e), (f) Nominal temperature distributions for $\mu = 0.75$. In this case, q''_{total} follows the E_T decreasing direction, and a positive κ_{app} is calculated.

Although the FM mode has an energy differential from the transverse and longitudinal modes, due to the very weak energy coupling between them, this energy differential can hold for a very long distance. Consequently, the heat current sustained by the FM phonons can be different from that sustained by the LM/TM phonons, in both magnitude and direction. Since q''_{FM} (from left to right) is larger than q''_{TM+LM} (from right to left), the net heat flux of the system q''_{total} is calculated at 3.23×10^9 W/m² in the direction from left to right. Generally speaking, under such condition one would expect that the temperature decreasing direction is in the same direction as the total heat flux. However, we clearly see in Fig 5.2(a) that the positive gradient of E_T is from right to left, which is in the opposite direction of the total heat flux. This surprising phenomenon is caused by the very different heat conduction capacity between FM and LM/TM phonons. Although q''_{FM} is larger in this case, since the FM phonon sustains a much higher thermal conductivity, the temperature/energy gradient of FM phonons is smaller. On the other hand, even q''_{LM+TM} is smaller, the low thermal conductivity sustained by LM+TM phonons requires a larger temperature/energy gradient to sustain this heat flux. Therefore, at the system level, we see the heat flux direction is opposite to the prediction based on the overall energy gradient. According to Fourier's heat conduction equation, the apparent thermal conductivity $\kappa_{1,11}$ is calculated at -90.5 W/m·K by linear fitting the E_T profile.

Here we would like to stress this negative apparent thermal conductivity does not violate the second law of thermodynamics, nor does it tell the thermal conductivity can

be negative for graphene. As discussed above, for each phonon mode, the heat current still flows from higher energy level to lower one, meaning its thermal conductivity is still positive. The negative apparent thermal conductivity originates from two factors: the very weak coupling between the FM and LM+TM phonons, and the much larger thermal conductivity sustained by FM phonons than that by LM+TM phonons. It tells one very important phenomenon in graphene: if there is phonon energy differential/separation between FM and LM+TM phonons during heat conduction, the local thermal conductivity based on Fourier's law of heat conduction will be different, depending on how much difference between the FM and LM+TM phonon energies, in both magnitude and gradient. The apparent thermal conductivity of graphene can be expressed as:

$$\kappa_{app} = (\kappa_{TM} \cdot \partial E_{TM} / \partial y + \kappa_{LM} \cdot \partial E_{LM} / \partial y + \kappa_{FM} \cdot \partial E_{FM} / \partial y) / [(\partial E_{TM} / \partial y + \partial E_{LM} / \partial y + \partial E_{FM} / \partial y) / 3].$$

Only when the three phonon modes have the same temperature gradient in space, the thermal conductivity of graphene is the sum of the three modes thermal conductivities. Otherwise, the thermal conductivity of graphene will vary, depending on the extent of energy separation among phonon modes. More elaboration on this argument will be detailed in the following sections.

For comparison, another bi-directional heat conduction case with $\mu=0.75$ is also calculated. All the calculation procedure and parameter settings are the same as the first case except for $\Delta \dot{E}_{k,FM} = 1.47 \times 10^{-8}$ W. The nominal temperature distributions of the

system are shown in Figs 5.2(d), (e) and (f). In this case, the net heat flux is calculated at -7.34×10^9 W/m² (from right to left), which is in the same direction as the negative gradient direction of E_T . The apparent thermal conductivity $\kappa_{0.75}$ is calculated at 139.6 W/m-K. In the above two cases, both positive and negative κ_{app} are observed in the GNR system. In the following discussions, more bi-directional heat conduction cases with different μ values are calculated to explore the condition under which a negative κ_{app} will appear.

As mentioned in the above discussions, after 400 ps bi-directional heating and cooling process, the heat conduction in the 2.0×50.1 nm² GNR reaches steady state and the nominal temperature gradient for E_T becomes constant. However, since there are mode-wide energy differences between E_{FM} and E_{TM} / E_{LM} , energy exchange happens among different phonon modes. Therefore, it could be argued that the system has not yet reached thermal equilibrium in respect of individual phonon mode. To prove that thermal equilibrium is established for both the GNR system and individual phonon branch, atomic velocity distribution at 12.5 nm, 25.0 nm and 37.5 nm locations in the length direction of the 2.0×50.1 nm² GNR is calculated for $\mu=1.11$. At thermal equilibrium, the atomic velocity distribution should follow the Maxwellian distribution

$$P_M = 4\pi v^2 \left(\frac{m}{2\pi k_B T} \right)^{3/2} e^{-mv^2/2k_B T}, \quad (5-1)$$

where P_M is the probability for an atom moving with a velocity v . Since E_{TM} , E_{LM} and E_{FM} have different values within each region, the velocity distributions for each

phonon mode are calculated. The v_{TM} , v_{LM} and v_{FM} distributions at 12.5 nm area are shown in Fig. 5.3, which indicates a good agreement between the velocity distribution and the Maxwellian distribution. Although mode-wide energy differences exist, each phonon mode has reached steady state heat conduction, which also proves the validity of temperature/energy use in the above calculations for each mode.

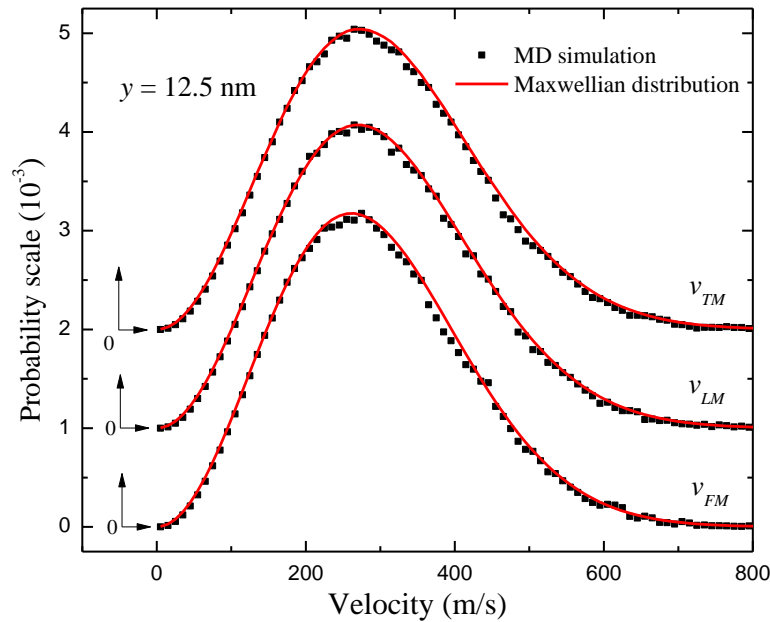


Figure 5.3. Atomic velocity distributions for individual phonon mode in the $2.0 \times 50.1 \text{ nm}^2$ GNR system at 12.5 nm location for $\mu=1.11$. Sound agreements between the MD simulation and Maxwellian velocity distribution are observed.

Error analysis is performed in our calculations. In this work, all the graphene systems reach thermal equilibrium after 400 ps canonical ensemble (NVT) and 100 ps microcanonical ensemble (NVE) calculations. In the thermal equilibrium calculations, the system temperature varies around the pre-set temperature 50.0 K. Take the $\mu = 0.75$

case as an example, after 500 ps thermal equilibrium calculation, the average temperature of the system is 50.1 K and the standard deviation (σ) of the system temperature variation is calculated at 1.2 K. Since the initial setup and calculation processes are the same for all the systems, the error bar of temporal averaging will be around the same range, which is ± 1.2 K.

5.2.2. Comparison study in solid argon system

Our interpretation of the negative κ_{app} observed in the GNR system is its much higher thermal conductivity by FM phonons, and weak energy coupling between the FM and LM/TM phonons. Therefore, for a normal material with the same thermal conductivity sustained by different phonon modes, the negative total temperature gradient should always be in the same direction as the net heat flux and its thermal conductivity should remain positive. To elaborate on this speculation, a solid argon system with dimensions of $4.3 \times 4.3 \times 50.1$ nm³ ($x \times z \times y$) is used to investigate its κ_{app} under steady state bi-directional thermal conduction. Atomic configuration of the argon system is depicted in the inset of Fig. 5.4(b). The outermost layer of argon atoms at each end is fixed (denoted in black), and free boundary conditions are applied to the x and z directions. Four layers of argon atoms at each end of the system are grouped to add/subtract phonon energies. Since the nearest neighbor distance r_s in the fcc lattice of argon depends on the temperature, we use the expression given by Broughton and Gilmer[92] to initialize the r_s value, which is calculated at 3.768 Å at temperature 20 K. The interactions between argon atoms are described by the 12-6 LJ potential

$\phi_{ij} = 4\varepsilon[(\sigma / r_{ij})^{12} - (\sigma / r_{ij})^6]$. The ε and σ are set as 0.01032 eV and 3.406 Å respectively and the cut off distance r_c is taken as 2.5σ . Time step is 5 fs for all calculations.

After 1 ns NVT and 500 ps NVE calculations, the argon system reaches thermal equilibrium at temperature 20 K. Then bi-directional heating and cooling process is performed for another 2 ns until the system reaches steady state heat conduction. Another 50 ps is calculated for the data collection and average. The nominal temperatures in the x , y and z directions are denoted as $E_{TM,x}$, E_{LM} and $E_{TM,z}$ respectively. Three different cases are calculated. Similarly, the $\Delta\dot{E}_{k,LM} + \Delta\dot{E}_{k,TMx}$ ($\Delta\dot{E}_{k,LM} = \Delta\dot{E}_{k,TMx}$) added/subtracted at each end is kept the same as 1.16×10^{-8} W for all cases, while $\Delta\dot{E}_{k,TMz}$ are set as 8.71×10^{-9} W, 1.16×10^{-8} W and 1.39×10^{-8} W. Their nominal temperature distributions are shown in Figs. 5.4(a), (b) and (c) respectively. Compared with the GNR cases above, it is observed in the solid argon system that the mode-wide energy differences only exist near the heating and cooling regions. The energy differences only exist in a very short distance (~ 1 nm) from the heating and cooling regions and the phonon energies then remain the same along the heat conduction direction, indicating strong phonon energy couplings among different phonon modes. Or we can say the bi-directional heat conduction only exists in very small regions close to the ends, then the heat conduction becomes one-directional. In Fig. 5.4(a), it is seen that the net heat flux q''_{total} and negative temperature gradient follows the same direction from right to left. And by linear fitting the E_T distribution, thermal conductivity κ_1 is

calculated at 0.637 W/m·K.

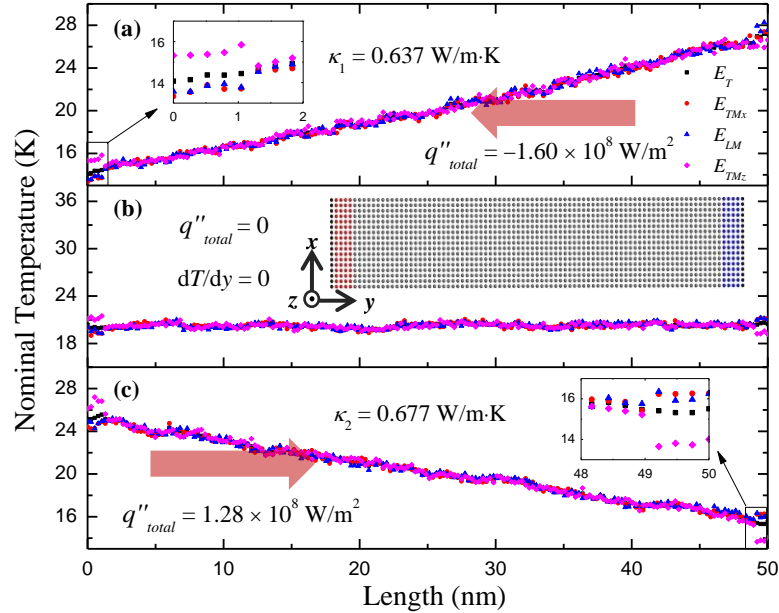


Figure 5.4. Nominal temperature distributions under steady state bi-directional heat conduction in the solid argon system. (a) The net heat flux is $1.60 \times 10^8 \text{ W/m}^2$ from right to left. The thermal conductivity κ_1 is calculated at 0.637 W/m·K. The inset shows that the mode-wide energy separation only exists within the first 1 nm of the system and the bi-directional heat conduction does not penetrate deep to the system (b) No temperature gradient is observed when the net heat flux is zero. Atomic structure of the solid argon system is shown in the inset. The outermost layer of argon atoms at each end (denoted in black) are fixed and free boundary conditions are applied to the x and z directions. Then four layers of argon atoms at each end (denoted in red and blue) are grouped to add/subtract energy. (c) The net heat flux is $1.28 \times 10^8 \text{ W/m}^2$ from left to right and thermal conductivity κ_2 is calculated at 0.677 W/m·K, which is consistent with κ_1 .

No temperature gradient is observed in Fig. 5.4(b) when q''_{total} equals zero.

Figure 5.4(c) gives similar conclusions as Fig. 5.4(a) and the thermal conductivity κ_2 is calculated at 0.677 W/m·K, which is consistent with κ_1 . Previous studies reported

thermal conductivity is around 1.4 W/m·K for solid argon at temperature 20 K.[93-97] Our calculated thermal conductivity for solid argon is lower than the experimental results.

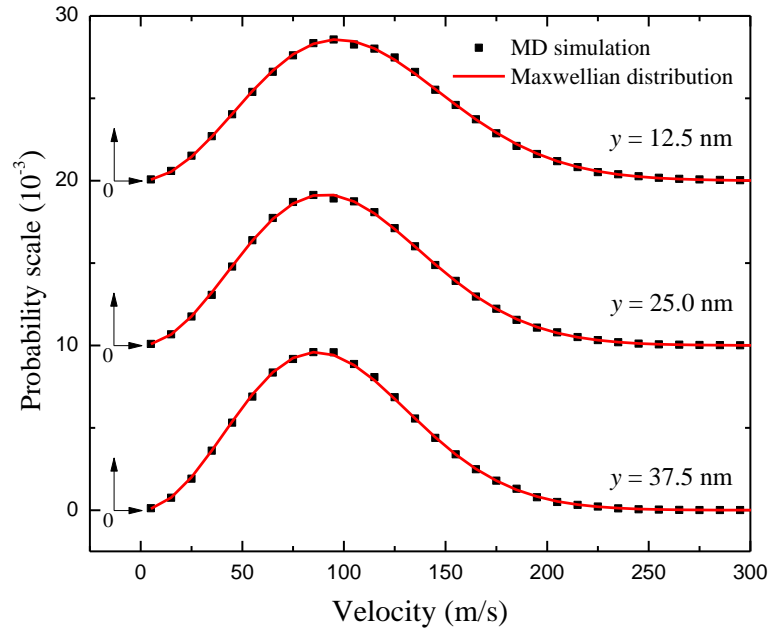


Figure 5.5. Atomic velocity distributions under steady state bi-directional heat conduction in solid argon system. Different locations at 12.5 nm, 25.0 nm 37.5 nm are used in the calculation and the MD results agree well with the Maxwellian distribution.

The small system size and the relative large surface/volume ratios contribute to the boundary phonon scattering during thermal conductance, which explains the slightly lower thermal conductivity calculated here for argon. Such effect has been confirmed by Zhong *et al*[98] in their work, the thermal conductivity of a round argon wire of 4.3 nm diameter at 30 K was calculated to be 0.28 W/m·K, much lower than the bulk value of 0.78 W/m·K. Atomic velocity distribution in the solid argon system is also calculated

and the results for the $\Delta\dot{E}_{k,TMz}=1.39\times 10^{-8}$ W case are shown in Fig. 5.5.

Three different regions at 12.5 nm, 25.0 nm and 37.5 nm in the length direction are chosen. The MD results and the Maxwellian distributions have sound matches, indicating that the argon system has reached thermal equilibrium when the data are collected. Compared with the GNR cases, no mode-wide energy differences are observed under steady state heat conduction in the argon system except a very small (1 nm) region adjacent to the heating/cooling regions, and the thermal conductivity remains positive and consistent for all calculations. This further proves the fact that the negative κ_{app} in GNR is caused by significant mode-wide deviation in thermal conductivity. To be specific, the FM phonon thermal conductivity is much higher than those of LM and TM phonons. The weak coupling between FM and LM/TM phonons is also an important factor that contributes to the negative κ_{app} in GNR.

5.2.3. κ_{app} topology for graphene

By applying bi-directional heat conduction in GNR, both positive and negative κ_{app} have been observed. To further explore this unique thermal transport phenomenon of graphene, cases with various $\Delta\dot{E}_{k,FM}$ values are calculated. Following the same calculation process and parameters in previous calculation, bi-directional heat conduction systems with μ values of 0, 0.12, 0.24, 0.45, 0.75, 1, 1.05, 1.11, 1.17, 1.26, 1.32, 1.38, 1.41, 1.44, 1.5, 1.65 and ∞ are calculated and their corresponding κ_{app} values

are plotted in Fig. 5.6. The $\mu=\infty$ case means no $\Delta\dot{E}_{k,TM}$ or $\Delta\dot{E}_{k,LM}$ are added/subtracted to/from the GNR system and only $\Delta\dot{E}_{k,FM}$ is applied, while $\mu=0$ means the opposite. Several very interesting phenomena are found in the κ_{app} calculations.

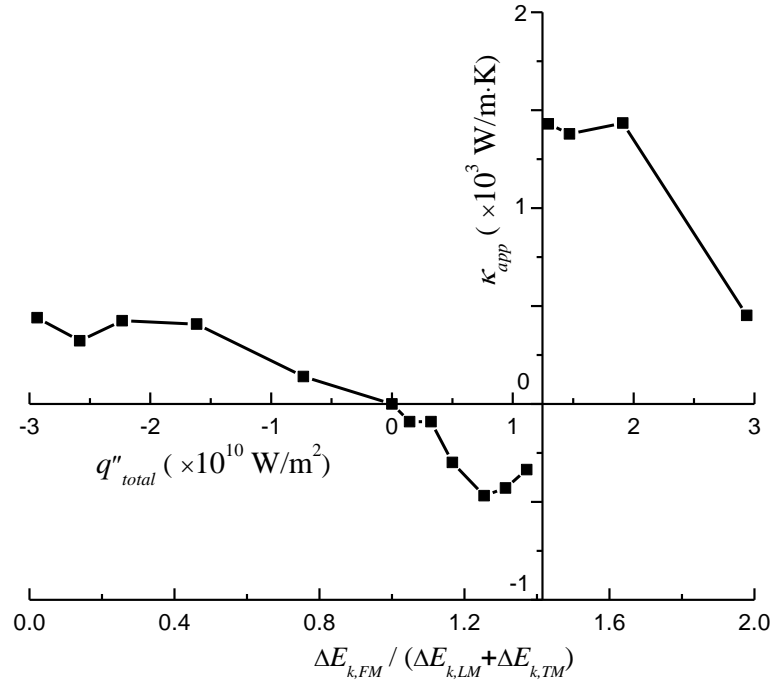


Figure 5.6. Apparent thermal conductivity (κ_{app}) topology for the $2.0 \times 50.1 \text{ nm}^2$ GNR system. The upper x -axis represents the net heat flux in the GNR system and the lower x -axis stand for the corresponding μ values. Negative κ_{app} is observed when μ is within the range of 1.05-1.38.

First of all, when μ equals 1, which means the net heat flux q''_{total} is zero, a nominal temperature gradient with a value of 0.04 K/m is observed in the E_T distribution. Therefore, the κ_{app} of GNR has to be zero to satisfy the Fourier's heat conduction equation. And when μ equals 1.41, a net heat flux of value $1.2 \times 10^{10} \text{ W/m}^2$ exists in the

system. However, after the system reaches steady state, the nominal temperature gradient is calculated at 4.2×10^{-4} K/m, which is small enough to be considered zero. In such scenario, κ_{app} is calculated to be infinite according to Fourier's law of heat conduction. Based on our calculations, it is observed that when μ changes from 0 to 0.75, κ_{app} is positive. As μ become larger within the range of 1.05-1.38, κ_{app} is negative. Yet when μ changes from 1.44 to ∞ , κ_{app} turns out positive again. It is concluded that κ_{app} of GNR is highly related with μ and the negative κ_{app} occurs only within a small range.

The physical meaning carried by the parameter μ indicates that when μ is smaller than 1, the bi-directional heat conduction in GNR is dominant by the in-plane LM and TM phonons, while when μ is larger than 1, the heat conduction is dominant by the out-of-plane FM phonons. It is observed that if the LM/TM phonon conduction is dominant, an overlap area among FM, LM and TM phonon energies exists at steady state. As μ increases, the overlap regions become smaller and when μ is larger than 1, no energy overlap is observed. To give a better description, nominal temperature distributions for μ values of 0.24, 0.75, 1.2 and 1.5 are shown in Fig. 5.7. The reasons for this phenomenon are the high thermal transport capacity of the FM phonons in GNR and the weak energy coupling between the FM and LM/TM phonons. Since the FM phonons have a much higher thermal conductivity in GNR, the thermal energies carried by the FM phonons will be transported to the heat sink much faster than those of LM and TM phonons.

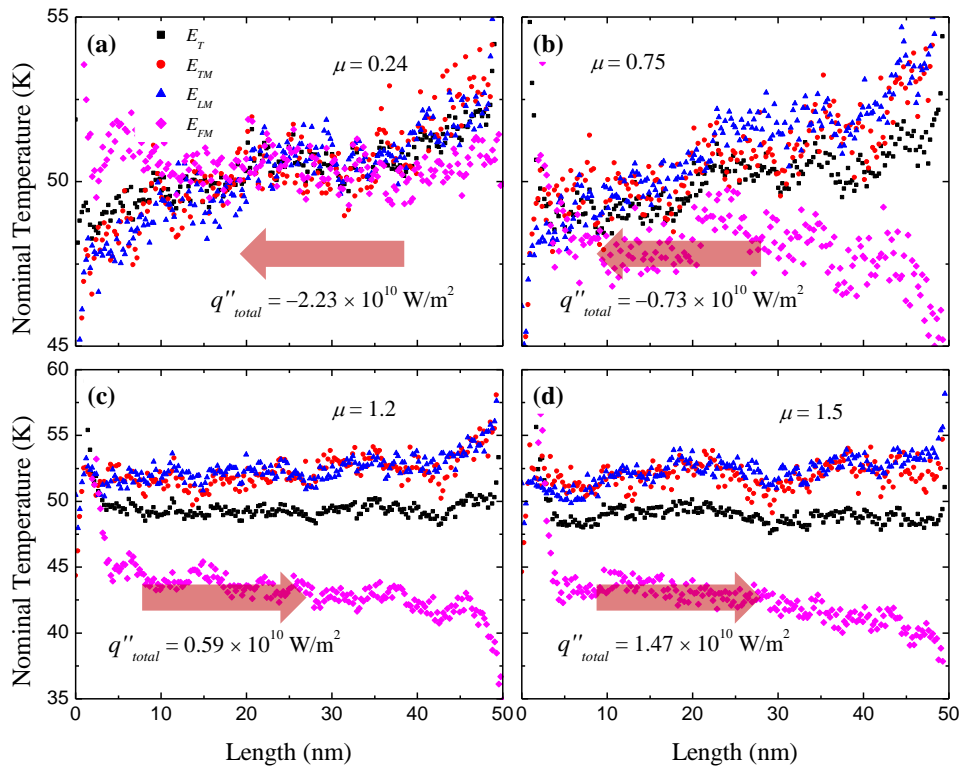


Figure 5.7. (a), (b) When the in-plane LM/TM phonon heat conduction is dominant ($\mu < 1$), an energy overlap is observed among different phonon modes. The length of the overlap region decreases with increasing μ . (c), (d) When the flexural phonon thermal transport is dominant ($\mu > 1$), there is no energy overlap among different phonon modes and the mode-wide energy separation increases with μ .

Therefore, if the same amount of thermal energy is added/subtracted to/from the FM and TM/LM phonons, the local E_{FM} values will eventually be smaller than the E_{LM}/E_{TM} along the heat conduction direction. Under this condition, the LM/TM phonons will keep transferring energy to the FM phonons as long as mode-wide energy differences exist. However, if the LM/TM phonon conduction is dominant in GNR ($\mu < 1$), the FM phonons will only be assigned with a small portion of the total heat

conduction. The temperature/energy gradient of FM phonons will be very small. Therefore a smaller energy difference emerges between FM and LM+TM phonons. This leads to an energy overlap among the three phonon mode, as is shown in Figs 5.7(a) and (b). Figures 5.7(c) and (d) demonstrate that when the FM phonon heat conduction is dominant ($\mu > 1$), the overlap will be suppressed. As the μ value increases, more heat will be carried by the FM phonons and the mode-wide energy differences will become larger and larger. This growing energy difference will enhance the energy transfer from E_{LM}/E_{TM} to E_{FM} , which leads to a smaller nominal temperature gradient for the E_{LM} and E_{TM} , as is shown in Figs. 5.7(c) and (d). It is worth noting that when energy overlap happens among the in-plane and out-of-plane phonons, the bi-directional heat conduction does not exist over the entire length and only exists in the energy separation regions. In other words, mode-wide energy separation is a necessary condition for the bi-directional heat conduction. Energy separation among phonon modes is a very important phenomenon in graphene, even under normal heat conduction conditions. More detailed analysis about energy separation, including the effect of temperature jump/drop from heating/cooling regions to the normal heat conduction region will be elaborated in our near-future publications since this work is focused on the bi-directional heat conduction and the apparent thermal conductivity (κ_{app}).

5.2.4. Single-end bi-directional heat conduction and the length effect

To further explore the thermal behavior of graphene under bi-directional heat conduction, a single-end heating and cooling method is applied to the $2.0 \times 50.1 \text{ nm}^2$

($x \times y$) GNR system. This time, only the left end of the GNR is used to apply the FM phonon heating and LM/TM phonon cooling.

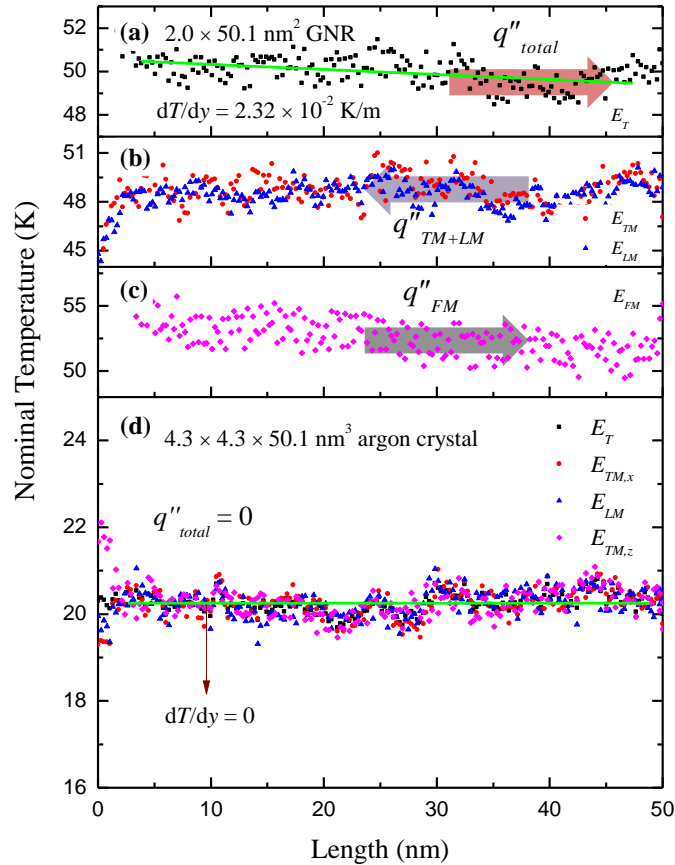


Figure 5.8. Nominal temperature distributions for the bi-directional heat transfer in GNR and solid argon with one-end heating/cooling. The net heat flux equals zero for both cases. For the GNR system, the nominal temperature gradient is 0.0232 K/m, which indicates an apparent zero value κ_{app} according to Fourier's law of heat conduction. While for the solid argon system at temperature 20 K, the temperature gradient is calculated at zero.

The same method is also applied to a $4.3 \times 4.3 \times 50.1$ ($x \times z \times y$) nm^3 solid argon system for comparison. After the GNR system reaches thermal equilibrium at

temperature 50 K, $\Delta\dot{E}_{k,FM}$ of value 1.96×10^{-8} W is added to the left end and $\Delta\dot{E}_{k,TM} + \Delta\dot{E}_{k,LM}$ ($\Delta\dot{E}_{k,TM} = \Delta\dot{E}_{k,LM}$) of the same value is subtracted from the same region for 400 ps. Another 50 ps is calculated for the data collection and average. The results are shown in Figs 5.8(a), (b) and (c). The nominal temperature distributions show that the thermal energy is carried by the FM phonons from left to right and then carried back by the LM/TM phonons from right to left. Since the kinetic energy added/subtracted has the same amount at the left end, the net heat flux of the system is zero. However, a nominal temperature gradient 0.025 K/m is observed from the profile of E_T , which indicates that κ_{app} of graphene is zero. As for the solid argon system, after it reaches thermal equilibrium at temperature 20 K, bi-directional heating and cooling is applied on the left end for 2 ns and the thermal energy added/subtracted equals 1.16×10^{-8} W. The nominal temperature distributions are shown in Fig 5.8(d). It is found that the nominal temperature gradient is zero, which satisfies the Fourier's heat conduction equation. For argon, only in a very small region (~ 1.0 nm) next to the left end that we found energy separation between $\Delta\dot{E}_{k,TMz}$ and $\Delta\dot{E}_{k,LM} / \Delta\dot{E}_{k,TMx}$, meaning the bi-directional heat conduction does not penetrate deep to the system.

The calculated high thermal conductivity values of graphene suggest that the mean free path in GNR is long even at room temperature. This may result in a strong length dependence of GNR's thermal conductivity. Therefore, the traditionally defined thermal conductivity is no longer an intrinsic property of GNR. Instead, it changes with

the length. Thus it is necessary to explore the length effect on the bi-directional heat conduction of GNR and observe the κ_{app} change with length. A $2.0 \times 100.0 \text{ nm}^2$ ($x \times y$) GNR is built to compare with the former $2.0 \times 50.1 \text{ nm}^2$ case. When $\mu = 0.45$, κ_{app} of 100.0 nm GNR is calculated at 487 W/m·K, which is 16% larger than that of 50.1 nm (408 W/m·K). When $\mu = 1.14$, the calculated κ_{app} of 100.0 nm GNR is $-605 \text{ W/m}\cdot\text{K}$, which is 34% larger than that of 50.1 nm ($-451 \text{ W/m}\cdot\text{K}$). By comparing the results above, it is ready to conclude that the κ_{app} values of GNR will increase with length while preserving the signs.

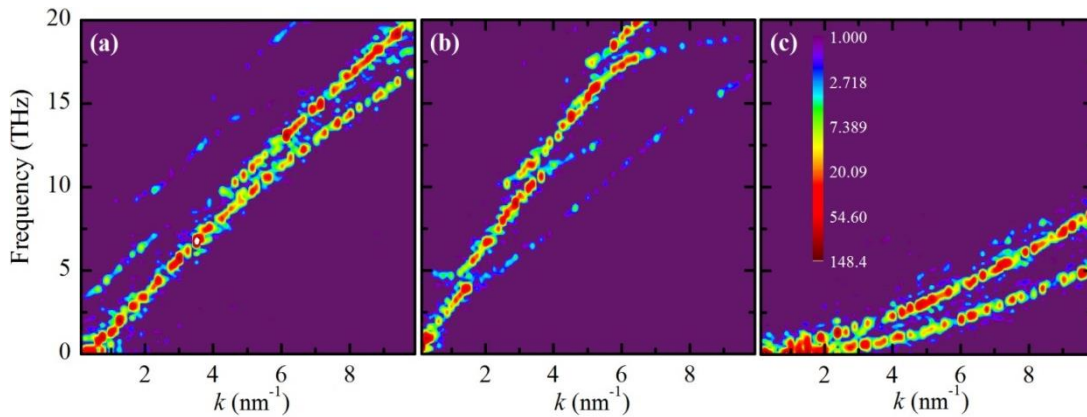


Figure 5.9. Dispersion relations for the $2.0 \times 50.1 \text{ nm}^2$ GNR system. (a), (b), (c) represent transverse, longitudinal and flexural modes phonon, respectively.

To better analyze the thermal conductivity in the graphene system, mean free paths for individual phonon modes are calculated and the results are shown in Fig. 5.10. The phonon behavior in graphene can be well understood from its dispersion relations in the k -space. The dispersion relations are computed by taking the two-dimensional

Fourier transform of atomic vibration in the space and the energy density in (ω, k) space is expressed as:[99]

$$\psi = \left| \frac{1}{N} \int v_{\alpha} \exp(iky - i\omega t) dt dy \right| \quad (\alpha = x, y, z), \quad (5-2)$$

where N is the number of atoms in the system and y is the heat conduction direction. The velocity vector is projected to the x , y and z directions to calculate the phonon energy density for transverse mode (TM), longitudinal mode (LM) and flexural mode (FM) phonons respectively. Similar method has been used to analyze individual phonon properties for various material systems.[100-105] It has been proved that Eq. (5-2) is a linear superposition of Lorentzian functions with centers at phonon frequency ω_0 :[106, 107]

$$\psi = \frac{C}{\sqrt{[2\tau(\omega - \omega_0)]^2 + 1}}, \quad (5-3)$$

where C is the combination of coefficients in the Lorentzian function and τ is the phonon relaxation time. By fitting the phonon frequencies calculated from Eq. (5-2), the phonon relaxation time can be calculated for different k values. Differentiation is then performed on the dispersion relation profiles to find out corresponding phonon propagating speed v for each τ . It is worth noting that since k and ω are highly correlated in the reciprocal space, the phonon mean free path (l) can be directly calculated using the above method as ψ also centers at wave vector k_0 as $\psi = C_k / \sqrt{[2l(k - k_0)]^2 + 1}$. However, not all k values are available in the calculation of dispersion relation. The minimum increment of k depends on the size of the graphene system. Therefore, a large simulation domain is

needed to achieve k grid with reasonable resolution, which dramatically increases the computation time.

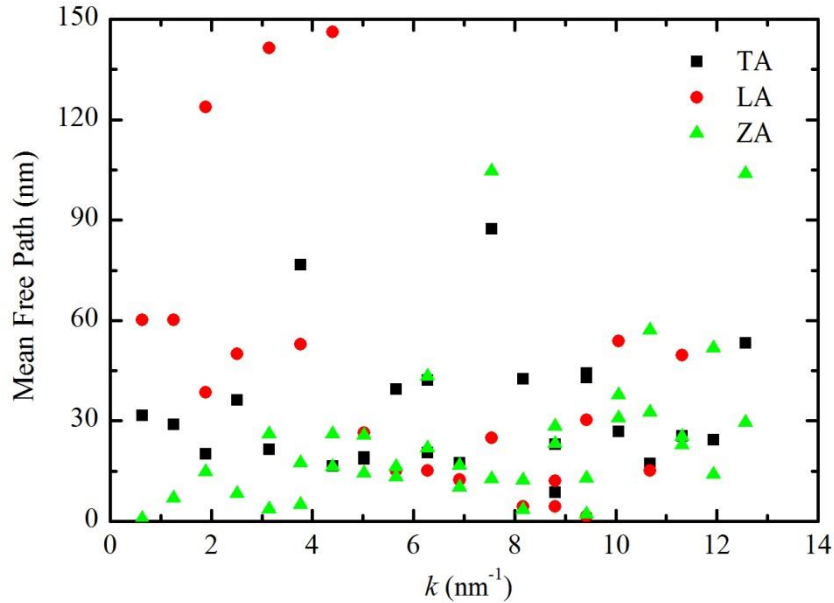


Figure 5.10. Mean free path of TA, LA and ZA mode phonons in k -space.

In this work, a time range of 10 ps is used in the calculation of graphene's dispersion relation, corresponding to a resolution of 0.2π THz in the ω -space. Since the thermal transport in graphene is dominant by acoustical phonon modes,[11, 67, 87, 98, 108] only low frequency (0-20 THz) phonon spectrums are calculated. Dispersion relations for the $2.0 \times 50.1 \text{ nm}^2$ GNR system are shown in Fig. 5.9. The calculated results have sound agreement with previous studies.[58] Phonon mean free paths are calculated accordingly and the results are shown in Fig. 5.10. It can be seen that the phonon mean free path is distributed within the range 0-150 nm, smaller than previous

reported value (775 nm)[109] due to the confined dimension of graphene used in this study. Qiu *et al.*[110] also calculated the phonon mean free path of suspended GNR with dimensions of $4.4 \times 4.3 \text{ nm}^2$ and their results are in the same range with those reported in our work.

CHAPTER 6. THERMAL TRANSPORT ACROSS GRAPHENE-SILICON INTERFACE

The limited internal phonon coupling and transfer within graphene in the out-of-plane direction significantly affects graphene-substrate interfacial phonon coupling and scattering, and leads to unique interfacial thermal transport phenomena. A very high interfacial thermal resistance of $5.30_{-0.46}^{+0.46} \times 10^{-5} \text{ K}\cdot\text{m}^2/\text{W}$ is observed by using a Raman frequency method under surface Joule heating.[76] The thermal contact resistance between graphene and SiO_2 was measured at $5.6 \times 10^{-9} - 1.2 \times 10^{-8} \text{ K}\cdot\text{m}^2/\text{W}$ using a differential 3ω method.[111] Using nonequilibrium molecular dynamics (NEMD) simulation, Wei *et al.*[112] calculated the interfacial thermal resistance between two neighboring graphene layers at $\sim 4 \times 10^{-9} \text{ K}\cdot\text{m}^2/\text{W}$. Understanding and control of the interfacial thermal resistance is crucial to the development and performance of high performance graphene-based devices.[113] The thermal resistance is a major limiting factor for the related nanoscale thermal engineering. Addressing the thermal resistance at the contact is, therefore, an important aspect of microelectronics and thermal management structures.

In this work, the thermal transport across the interface of graphene and silicon substrate is explored by performing MD simulations. The dynamic response of graphene to a thermal impulse is investigated and the interfacial thermal resistance between graphene and Si is evaluated. A transient pump-probe method is designed for interfacial thermal resistance characterization. Compared to the traditional NEMD method, this

pump-probe technique is focused on the dynamic thermal response of the system and can greatly reduce the computation time. Energy evolution in transient simulation is tracked and discussed for the supported graphene. The silicon substrate is chosen here because its vast applications in nanoelectronics.[114-117]

6.1. Methodology

6.1.1. Molecular dynamics simulation design

The second generation of Brenner potential:[29] reactive empirical bond-order (REBO), based on the Tersoff potential[34, 63] with interactions between C-C bonds is employed to model the graphene system. The Tersoff potential[34, 63] with interactions between Si-Si bonds is used to model the silicon system. The REBO potential is chosen because its functions and parameters are known to give reasonable predictions for the thermal properties of graphene,[76] whereas the adaptive intermolecular reactive empirical bond-order (AIREBO) was reported to underestimate the dispersion of ZA phonons in graphene.[118] It has been proposed that the interactions between carbon atoms and the substrate are primarily short-range van der Waals type (vdW).[119, 120] Therefore, the C-Si couplings is modeled as vdW interactions using the Lennard-Jones (LJ) potential $V(r) = 4\varepsilon[(\sigma/r)^{12} - (\sigma/r)^6]$, where σ is the distance parameter, ε the energy parameter and r is the interatomic distance. The ε parameter determines the strength of the specific interactions between graphene and silicon. In this work, ε and σ are set as 8.909 meV and 3.326 Å respectively.[121] To save computational time, the LJ

potential is truncated at the cut-off distance of $r_c = 3.5\sigma$. The initial velocities in each direction are extracted from the Gaussian distribution for the given temperature 300 K. At the start of simulation, the position of the GNR is located 3.7 Å above the upper layer of the Si bulk. Configuration of the system is shown in Fig. 6.1. Periodic boundary conditions are applied to the x and y directions and free boundary condition is applied to the z direction. Dimensions of the GNR are smaller than those of the silicon to avoid boundary interactions through the periodic boundaries. The step for time integration is 0.5 fs (1 fs = 10^{-15} s). All MD simulations are performed using the large-scale atomic/molecular massively parallel simulator (LAMMPS) package.[122]

6.1.2. Physics of the pump-probe method

The pump-probe transient thermoreflectance method has been widely used to study the thermal transport in bulk materials and thin films.[123] The Kapitza resistance and heat flow across material interfaces can also be measured using this optical technique.[124] In this work, a pump-probe method is developed using MD simulation to calculate the interfacial thermal resistance between graphene nanoribbons and silicon crystal. As shown in Fig. 6.1(a), after the MD system reaches thermal equilibrium, an ultrafast heat impulse is imposed on the supported GNR. In the heating process, non-translational kinetic energy is evenly added to the GNR system in each direction by rescaling velocities of atoms. When the excitation is released, the temperature of the GNR (T_{GNR}) will increase dramatically and then gradually reduce during the thermal relaxation process. In our work, three layers of silicon atoms beneath the supported GNR

are grouped to calculate the surface temperature of the silicon bulk (T_{Si}) as shown in Fig. 6.1(a). The T_{GNR} , T_{Si} and GNR system energy (E_t) are recorded each time step during the thermal relaxation. In the MD simulation, the energy decay of the GNR is only caused by its thermal energy loss to the silicon system. Therefore, given the energy and temperature evolution of the graphene system, the interfacial thermal resistance (R) between the supported GNR and silicon substrate can be calculated using the equation

$$\frac{\partial E_t}{\partial t} = \frac{T_{GNR} - T_{Si}}{R / A}, \quad (6-1)$$

where E_t is the system energy of the supported GNR and A is GNR's area. Instant R results can be calculated at each time step according to the local energy changing rate and corresponding temperature difference. We have tried this method and found it subject to the noise in the energy decay and the calculated interface thermal resistance has very large uncertainty. If R has little variation within the temperature range during thermal relaxation, a constant R value can be substituted into Eq. (6-1) to predict the E_t profiles. Under such scenario, the interfacial thermal resistance can be calculated by best fitting the E_t profile using the least square method using an integral form of Eq. (6-1) as detailed in next section.

6.2. Results and discussion

6.2.1. Thermal resistance evaluation

To understand the thermal transport across graphene and substrate interface, a silicon crystal with dimensions of $5.8 \times 40.0 \times 5.4 \text{ nm}^3$ ($x \times y \times z$) is built. The size of the

supported GNR is $4.1 \times 38.5 \text{ nm}^2$ ($x \times y$).

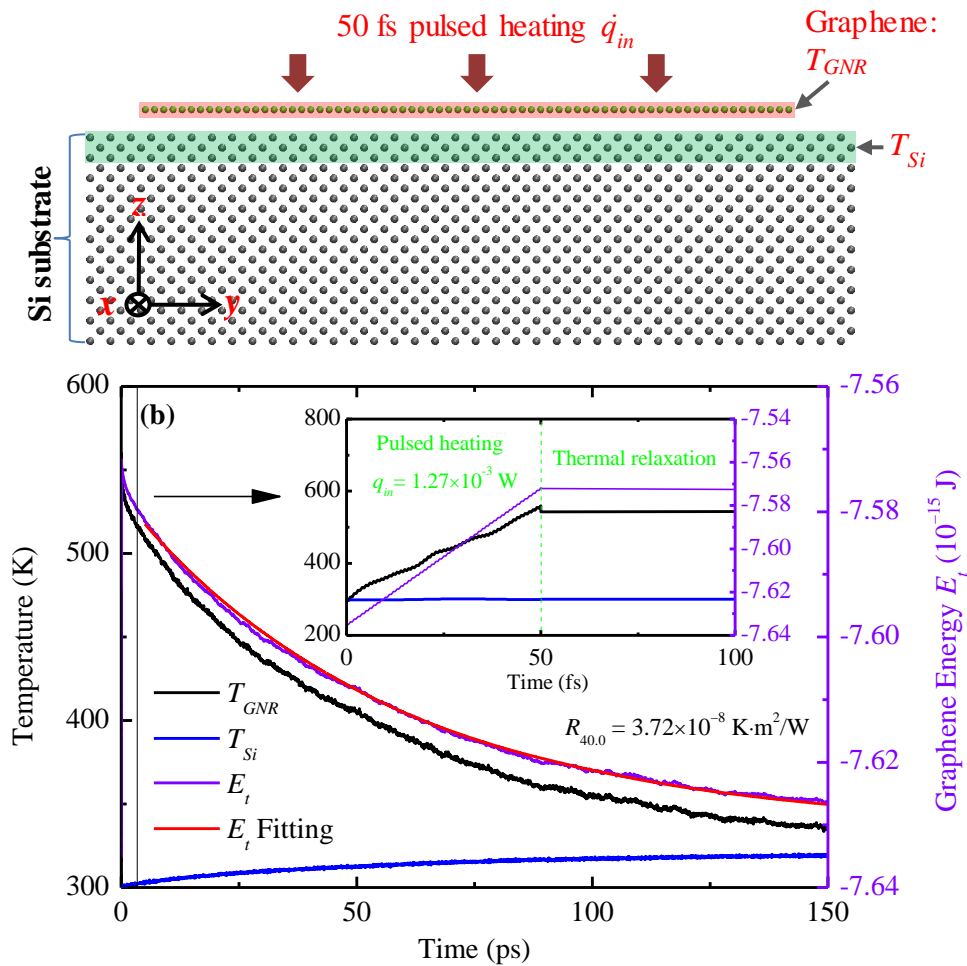


Figure 6.1. (a) Atomic configuration of the GNR and silicon system. Periodic boundary conditions are applied to the x and y directions and free boundary condition to the z direction. A thermal impulse \dot{q}_{in} is imposed on the supported GNR after thermal equilibrium calculation and the top three layers of silicon atoms are grouped to calculate the surface temperature of the silicon substrate. (b) Temperature evolutions (left y axis) of GNR and Si for 50 fs pulsed thermal excitation and 150 ps thermal relaxation. The overall energy and fitting for the supported GNR system are shown in the right y axis. The calculated thermal resistance from this overall fitting method equals $3.72 \times 10^{-8} \text{ K}\cdot\text{m}^2/\text{W}$. The fitting profile calculated from a single R value soundly matches the MD simulation results.

After 300 ps canonical ensemble (NVT) and 100 ps microcanonical ensemble (NVE) calculation, the whole system reaches thermal equilibrium at 300 K. Then the GNR is exposed to a thermal impulse $\dot{q}_{in}=1.27\times 10^{-3}$ W for 50 fs. After the excitation, T_{GNR} increases to 559.7 K and the adjacent silicon surface temperature T_{Si} is 299.4 K as shown in Fig. 6.1(a). In the following 150 ps thermal relaxation process, energy dissipation from graphene to the silicon substrate is recorded and the interfacial thermal resistance is calculated. The equilibrium distance between graphene and Si-substrate surface is 3.2 Å based on the modeling. Energy and temperature results are averaged by 100 in the calculation to suppress data noise. Temperature evolutions and energy fitting results are shown in Fig. 6.1(b). It is observed that after the 50 fs thermal excitation is released, the energy of the graphene goes down quickly due to the energy transfer to the Si-substrate. At the same time, the graphene temperature also goes down accordingly and a slight temperature rise is observed for the silicon atoms adjacent to the interface. The energy decay fitting in Fig. 6.1(b) is performed based on Eq. (6-1) and takes the integral form as $E_t = E_0 + (R/A) \cdot \int_0^t (T_{GNR} - T_{Si}) dt$. Here R is treated as a constant, and such assumption will be discussed and validated later. E_0 is graphene's initial energy.

The calculated thermal resistance $R_{40,0}$ equals 3.72×10^{-8} K·m²/W, which is in the same magnitude with previous studies of graphene on 6H-SiC and SiO₂. [111, 125] At the beginning part of the thermal relaxation process, a faster decay in GNR's total energy is observed. This is caused by the strong energy disturbance induced by the thermal impulse to the system. During that period, the potential and kinetic energies

have not yet reached equilibrium. Therefore, the initial part (5 ps) of the thermal relaxation profile is strongly dominated by the energy transfer from kinetic to potential energy in graphene, and is excluded from the fitting process. It can be observed from Fig. 6.1(b) that the fitting curves soundly matches the energy profiles using a constant $R_{40,0}$. This leads to a strong point that the interfacial thermal resistance between GNR and Si does not have large changes over the relaxation temperature 300K-500 K.

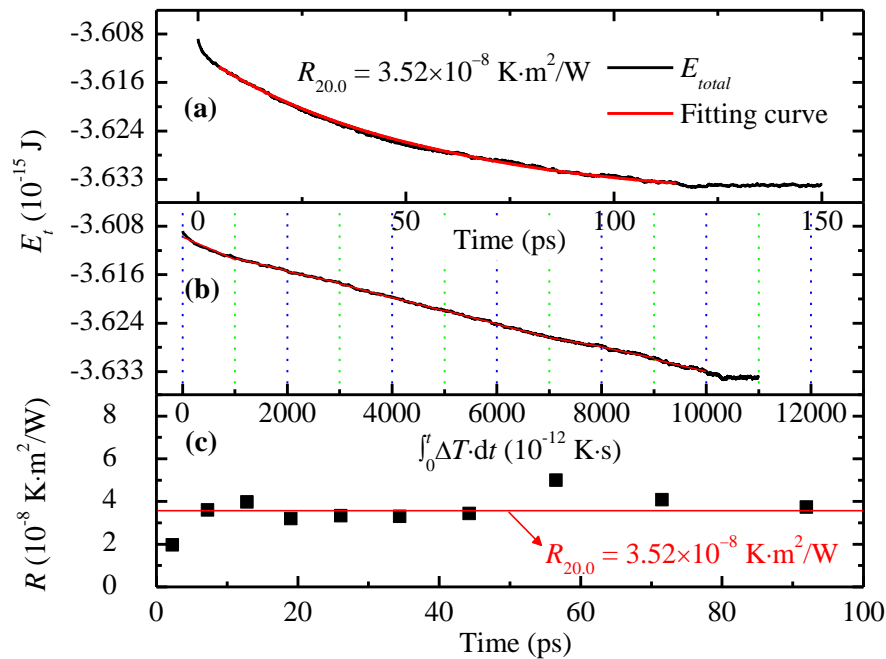


Figure 6.2. Comparisons of the overall fitting result and instant R calculation results. Size of the GNR is $4.1 \times 18.3 \text{ nm}^2$ ($x \times y$). By integrating the temperature differences between T_{GNR} and T_{Si} , the energy relaxation profile of GNR can be correlated to $\Delta T dt$ directly and slope of the profile can be linearly fitted to calculate the segment interfacial thermal resistance values, which is around the overall fitting results.

To further assess the validity of the overall fitting method with a constant R , a new case with GNR's dimensions of 4.1×18.3 ($x \times y$) nm^2 is built. The silicon substrate used is $5.8 \times 20.0 \times 5.4$ nm^3 ($x \times y \times z$). In this case, the heating rate \dot{q}_{in} equals 6.04×10^{-4} W and both overall and instant R values are calculated and compared. The overall fitting results using integration is shown in Fig. 6.2(a) and R is calculated at 3.52×10^{-8} $\text{K} \cdot \text{m}^2/\text{W}$. As the energy decay is driven by the temperature difference $\Delta T = T_{GNR} - T_{Si}$, in Fig. 6.2(b), we plot out how the graphene energy changes against $\int_0^t \Delta T dt$. It is observed that the E_t profile has a linear relation with $\int_0^t \Delta T dt$, which further proves the fact that the thermal resistance R is nearly constant during the relaxation process.

In fact, we can use this profile to determine the interfacial thermal resistance. The E_t profile is divided to many segments as shown in Fig. 6.2(b). For each segment (t_1 to t_2), R can be treated constant, and can be determined by linear fitting of the curve in Fig. 6.2(b). The determined slope equals A/R , and can be used to determine R . The calculated results are shown in Fig. 6.2(c). It is observed that instant R values vary around the overall fitting results $R_{20,0}$. From the above discussions, it is safe to conclude that the overall integration fitting method is accurate enough to be used in the pump-probe method.

6.2.2. Phonon mode energy decay and thermal rectification discussion

In the preceding discussions, it has been mentioned that the presence of a

substrate will significantly affect the thermal transport in graphene due to the damping of ZA phonons. The thermal conductivity of supported graphene is suppressed due to the strong phonon coupling at the interface.

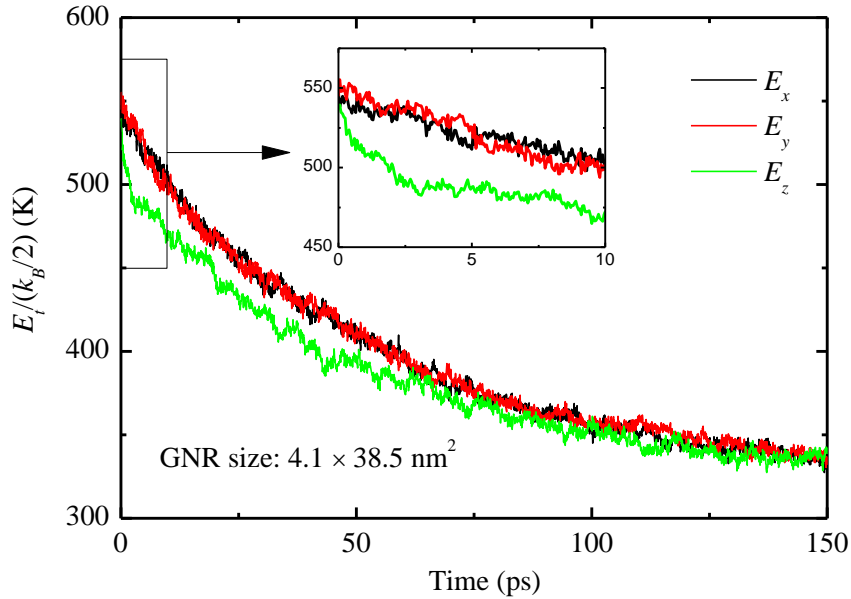


Figure 6.3. Phonon energy evolutions in the supported GNR system. It is observed that E_z decreases faster than E_x and E_y in the early stage, indicating a much stronger exchange between kinetic and potential energies for ZA phonons in graphene than the LA and TA phonons.

To obtain an insightful understanding of this problem, the decomposed energies for each phonon mode is evaluated for a $4.1 \times 38.5 \text{ nm}^2$ supported GNR. The energy is normalized to a nominal temperature defined as $E_i / (1/2)k_B$ with unit K is used to present the energy values in each direction. Here E_i is the kinetic energy in direction i ($i=x, y$ or z) and k_B is Boltzmann constant. Energy evolutions for the thermal relaxation process are shown in Fig. 6.3. Nominal temperatures of the three phonon modes are around the same

value 550 K at the beginning point ($t = 0$) of the thermal relaxation process (inset of Fig. 6.3). However, it is noticed that there is a quick drop of E_z when the thermal excitation is released. This is largely caused by the stronger coupling between the kinetic energy and potential energy for out-of-plane movements. Due to the strong energy decay in the ZA phonons, the in-plane longitudinal (LA) and transverse (TA) phonons will keep transferring thermal energies to ZA phonons until the energy difference is gone. This can be seen from the decreasing energy gaps between E_x , E_y and E_z along the relaxation time. The energy coupling rates among different phonons modes have been discussed in our previous study on energy inversion in graphene.[126]

Thermal rectification has been found in asymmetric graphene nanoribbons with different chirality.[16, 127-130] However, up to date, the thermal rectification between supported graphene and its substrate has not yet been studied. To explore this important thermal phenomenon, a silicon substrate with dimensions of $5.8 \times 10.2 \times 5.4 \text{ nm}^3$ ($x \times y \times z$) is built and the supported GNR is $4.1 \times 8.6 \text{ nm}^2$ ($x \times y$). After the system reaches thermal equilibrium at temperature 300 K, a heat impulse $\dot{q}_{in} = 2.84 \times 10^{-4} \text{ W}$ is imposed on the GNR system and by fitting the GNR's energy relaxation profile, the interfacial thermal resistance is calculated at $3.31 \times 10^{-8} \text{ K} \cdot \text{m}^2/\text{W}$. In this process, the energy is transferred from the heated graphene to the silicon substrate. To investigate the thermal rectification across the graphene-Si interface, two more cases are calculated with different initial system temperatures. The equilibrium temperature for the first case is 400 K. After thermal equilibrium calculation, thermal energy is removed from the GNR system for 50

fs with a cooling rate $\dot{q}_{out}=-2.48\times 10^{-4}$ W and T_{GNR} drops to 175 K at the end of the cooling process. The interfacial thermal resistance (R) is calculated at 3.20×10^{-8} K·m²/W based on global data fitting of the cooling process. This R value is only 3% lower than that of the heating case with $T_{GNR}>T_{Si}$. For the second case, the initial system temperature is set at 350 K. And after cooling the supported GNR with $\dot{q}_{out}=1.24\times 10^{-4}$ W for 50 fs, T_{GNR} decreases to 250 K. Following the same calculation procedure, the interfacial thermal resistance is calculated at 3.62×10^{-8} K·m²/W, which is 9% higher than that of the heating case ($T_{GNR}>T_{Si}$). It has been observed in the above discussions that the thermal resistance between graphene and Si-substrate do not have substantial changes against temperature, indicating that the thermal resistance for the cooling cases will be around the same values as above two cases. Considering the calculation uncertainty, the difference between the heating ($T_{GNR}>T_{Si}$) and cooling cases ($T_{GNR}<T_{Si}$) are very small. It is safe to conclude that there is no thermal rectification phenomenon in thermal transport across the graphene and silicon interface.

6.2.3. Effects of graphene dimension on interface energy transport

The size dependence of thermal conductivity has been reported in various low dimensional nanomaterials.[131-135] As a novel two dimensional material, it is found that the thermal conductivity of suspended graphene and graphene nanoribbons is also size dependent.[136, 137] The length effect on the thermal conductivity of graphene is due to its intrinsically long phonon mean free path, which is up to 775 nm at room temperature.[109] The confined dimension in the lateral directions of supported

graphene will greatly affect the phonon behaviors at graphene-substrate interface. Therefore, it is of great interest to investigate the effects of dimension on the interfacial thermal resistance between graphene and silicon.

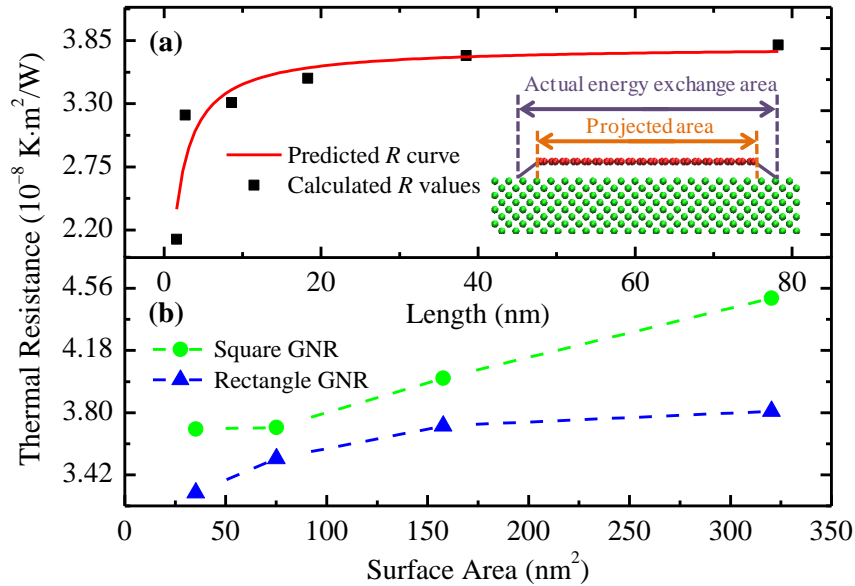


Figure 6.4. Effect of graphene dimension on the interfacial thermal resistance between GNR and Si. (a) When the length of the supported GNR becomes longer, the interfacial thermal resistance becomes larger due to the reduced edge. (b) Square shaped GNR has larger thermal resistance values than the rectangle shaped GNR ones.

To study the size effect on the interfacial thermal resistance, we fix the GNR's width at 4.1 nm and substrate thickness at 5.4 nm. Aside from the 8.6, 18.3 and 38.5 nm length cases calculated above, supported GNRs with lengths of 1.6, 2.7 and 78.2 nm cases are built and studied. The thermal resistance results calculated by the pump-probe method are shown in Fig. 6.4(a). It can be observed from Fig. 6.4(a) that the length of the supported GNR has significant impact on the interfacial thermal resistance between

GNR and Si at short length scales from 0 to 40 nm. When the length is larger than 40 nm, the calculated R tends to converge to a constant value. To elucidate this length effect, the actual energy exchange area on Si-substrate is explored. It has been mentioned in above discussions that the cut-off distance between carbon and silicon atoms are set as 3.5σ , which is 11.641 Å in all cases. The equilibrium distance between GNR and Si-substrate surface is ~ 3.2 Å. This indicates that the actual surface areas involved in the thermal transport process are larger than the projected GNR areas on the Si-substrate, which are used in the overall fitting method to calculate the interfacial thermal resistance. This phenomenon is explained in the inset in Fig. 6.4(a). The relation between the thermal resistance (R) calculated by the overall fitting method and the ideal one without the edge effect (R_{real}) is expressed as

$$R = \frac{R_{real} \cdot W \cdot L}{(W + \xi)(L + \xi)}, \quad (6-2)$$

where W and L are the width and length of the supported GNR respectively and ξ is the effective distance extended from the edge of the projected area, as is shown in the inset of Fig. 6.4(a). Such area extension is caused by the long-range vdW interaction. The interatomic forces in the extended areas are much weaker compared to those in the projected areas, yet these contributions cannot be neglected when the surface area of the supported GNR is small. Given the calculated thermal resistance values, we use Eq. (6-2) to fit the results shown in Fig. 6.4(a) to determine R_{real} and ξ . The ideal interfacial thermal resistance without the edge effect is determined at 4.68×10^{-8} K·m²/W and ξ is determined at 9.5 Å. The ξ value determined here is close to, and a little smaller than the

cut-off distance used in the calculation (11.641 Å), confirming that the size effect observed in Fig. 6.4(a) is largely induced by the extended graphene-Si interaction area from the projected area of graphene.

In the above calculations, the supported GNRs are all rectangle-shaped. To compare the effects of GNR's formation on the interfacial thermal resistance, square-shaped GNRs with the same surface areas are built and the results are shown in Fig. 6.4(b). It is evident that the interfacial thermal resistances of rectangle-shaped GNRs are smaller than those of square-shaped. It is ready to prove that under the same surface area, the rectangle formations have larger perimeters than the square formations. Therefore, both the phonon boundary scatterings and the effective thermal contact areas in the rectangle-shaped GNRs will be larger than those in the square-shaped GNRs, which will increase the phonon energy decay rate and lead to a smaller thermal resistance. We calculated that the extended distance ξ from the edges of supported GNR is 9.5 Å. Therefore, the effective thermal contact areas for both shapes can be calculated and the thermal resistance for the square-shaped GNRs can be predicted. Take the $4.1 \times 38.5 \text{ nm}^2$ GNR as an example, its interfacial thermal resistance is $3.72 \times 10^{-8} \text{ K} \cdot \text{m}^2/\text{s}$. The square-shaped GNR with the same surface area has a dimension $12.59 \times 12.59 \text{ nm}^2$. After adding ξ to the width and length calculation, their effective thermal contact areas ratio $A_{\text{eff},\text{rec}}/A_{\text{eff},\text{squ}}$ is calculated at 1.09. Based on this ratio, the thermal resistance for the square-shaped GNR can be predicted at $4.04 \times 10^{-8} \text{ K} \cdot \text{m}^2/\text{s}$. This prediction is very close to the calculated result $4.01 \times 10^{-8} \text{ K} \cdot \text{m}^2/\text{s}$ by direct MD simulation, which further proves

the validity of the effective surface area analysis. One argument would arise that the size of the supported graphene will affect the phonon mean free path, which then will affect the phonon coupling between graphene and Si. We expect this speculation would hold and be more visible for larger size graphenes. In our calculation, the graphene size is very small, (4.1 nm width for the rectangular one), so the phonon mean free path in graphene is significantly suppressed, and does not have strong/visible effect on the phonon coupling between graphene and Si.

6.2.4. Effects of surface roughness

Graphene is considered a promising nanomaterial with applications in nanoelectronics and nanocircuits. Our previous research has revealed that when graphene nanoribbons are bent to fit the substrate structures, a thermal resistance will emerge in the bending area due to local phonon reflection and scattering.[138] Aside from the bending structures in these applications, the substrate surfaces are often dented in pattern to achieve maximum thermal radiation and realize various electrical functions. In spite of the vast applications of graphene in nanoelectronics, however, to our best knowledge, the effects of surface roughness on the thermal transport across graphene-substrate interface have not been studied. In this section, the interfacial thermal resistance between graphene and rough silicon substrate of well-defined roughness is studied.

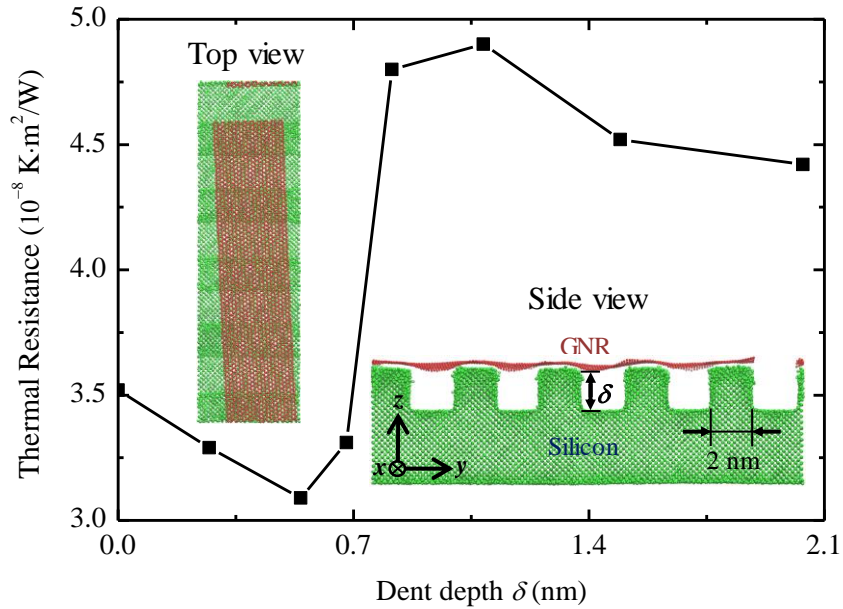


Figure 6.5. Interfacial thermal resistance variations with surface roughness. Atomic configuration is depicted in the insets for the case of $\delta=2.0$ nm.

A silicon substrate with dimensions of $5.8 \times 20.0 \times 5.4$ ($x \times y \times z$) nm^3 is built and the size of the supported GNR is 4.1×18.3 ($x \times y$) nm^2 . There are millions combinations of roughness patterns on the surface of the Si-substrate and it is impossible to calculate all of them. To simplify this study, only one of the patterns is used in this work and variations are made by changing the dent depth δ . The grooves are made in x direction of the Si-substrate and the width for each groove is ~ 2.0 nm, which is the same as the separation distance for the neighboring grooves. Atomic configurations of the system after thermal equilibrium are shown in the insets of Fig. 6.5. Periodic boundary conditions are applied to the x and y directions and free boundary condition is applied to the z direction. Take the $\delta = 2.0$ nm case as an example, after 300 ps NVT and 100 ps

NVE calculations, the whole system reaches thermal equilibrium at 300 K. Then a thermal impulse of $\dot{q}_{in} = 6.0 \times 10^{-4} \text{ W}$ is applied to the supported GNR for 50 fs. The whole system is then left for thermal relaxation under NVE calculations for another 150 ps. The calculated thermal resistance $R_{\delta=2.0 \text{ nm}}$ is $4.42 \times 10^{-8} \text{ K}\cdot\text{m}^2/\text{W}$, which is 26% larger than the flat surface case under the same conditions.

To further investigate the interfacial thermal resistance relations with surface roughness, variations have been made on the groove depth δ and cases of 0.27, 0.54, 0.68, 0.81, 1.09 and 1.49 nm cases are studied. Groove depth larger than 2.0 nm is not studied because the cut-off distance for the 12-6 LJ potential is only 1.16 nm. Therefore it is safe to speculate that the thermal resistance values will not change substantially for $\delta > 2.0 \text{ nm}$. The calculated thermal resistance values are shown in Fig. 6.5. It is very surprising and interesting to observe that the interfacial thermal resistance decreases when δ becomes larger when the groove depth is smaller than 7 Å. R reaches the lowest value as $R_{\delta=0.54 \text{ nm}} = 3.09 \times 10^{-8} \text{ K}\cdot\text{m}^2/\text{W}$. This is contrary to the traditional thought that a rough surface should always give a larger interfacial thermal resistance. To explain this novel phenomenon, the interatomic force between graphene and silicon are calculated for the $\delta = 0.54 \text{ nm}$ case and the results are shown in Fig. 6.6(a). The supported and suspended areas are cross-adjacent and each region has a width of 2.0 nm. Due to the roughness of the silicon surface, the interatomic forces are not evenly distributed in the supported graphene. The gap between the surface dent and suspended graphene causes net attractive forces on the local graphene. When the groove depth is small, this

attractive force is strong enough to bent the graphene to fit the silicon surface. As a result, net repulsive forces on the supported areas arise. For example, at the location 4~6 nm in the length direction of the GNR, the graphene is supported and the net interatomic force is calculated at $+1.17 \text{ eV/\AA}$. The positive sign indicates a repulsive force. This force gives a pressure of 228 MPa for the supported graphene. Such very high pressure will significantly reduce the local interfacial thermal resistance. At the location of 10~12 nm, the graphene is suspended. The net force is -2.36 eV/\AA and the negative sign indicates an attractive force. The contact pressure between the graphene and Si-substrate is increased significantly in the supported graphene region due to the increased repulsive interatomic forces, thus leads to a decreased thermal resistance between graphene and silicon. This thermal resistance decrease offsets the thermal resistance increase in the suspended region, giving an overall thermal resistance decrease.

From the above discussions, it is realized that the graphene is kind of stretched by the attractive force in the suspended region and repulsive force in the supported region. Such stretching could be reflected by the structure of the graphene. Radial distribution functions (RDF) for the supported GNRs are calculated and the results are shown in Fig. 6.6(b).

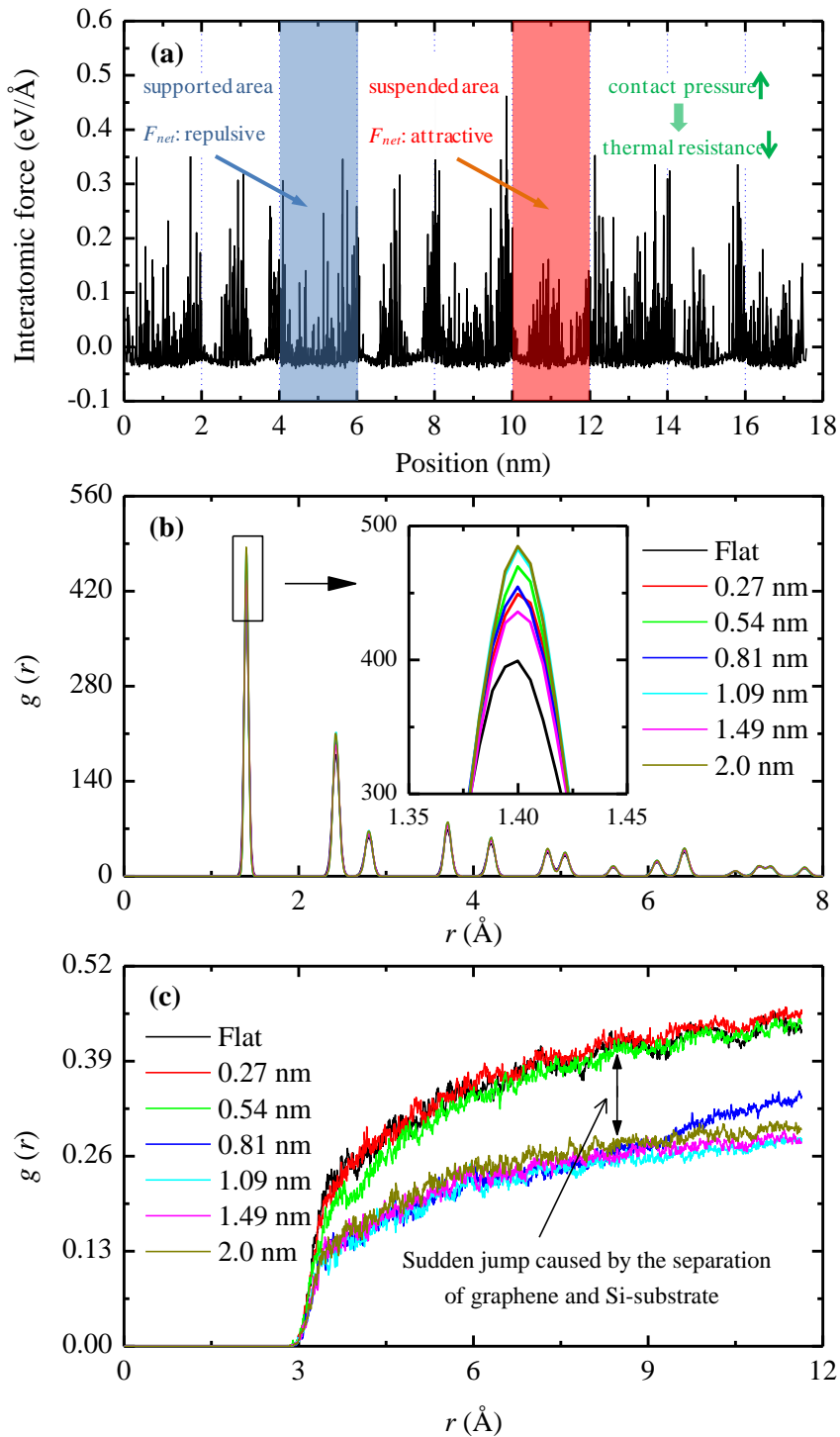


Figure 6.6. (a) Interatomic forces between supported GNR and $\delta = 0.54$ nm dented silicon substrate. The blue and red shaded areas indicate the supported and suspended GNR regions respectively. (b) Radial distribution functions for the

supported GNRs. The peaks are sharper for the dented Si cases, indicating stretching forces in graphene. (c) Radial distribution functions between graphene and Si-substrate. The $g(r)$ values drop to significant lower levels when the groove depth δ becomes larger than 0.81 nm, which explains the thermal resistance increase observed in Fig. 6.5.

Since all the supported GNRs share the same structure, their RDFs give the same formation for all cases. However, at the peak locations, the spike becomes sharper when GNRs are supported on the dented Si-substrate. Also a slight shift of the first peak location to larger atomic-separation is observed. This demonstrates that the structures of the supported GNRs are stretched due to the dented Si surface. When δ becomes larger, in the suspended region, a lot of graphene atoms have very weak or zero interaction with Si atoms. To elucidate this phenomenon, radial distribution functions between graphene and silicon are calculated and the results are shown in Fig. 6.6(c). It is observed that the $g(r)$ values are evidently larger at small dent depth and drop to lower levels when δ becomes larger than 0.81 nm. This is corresponding to the jump of the interfacial thermal resistance from $\delta=0.54$ nm to $\delta=0.81$ nm observed in Fig. 6.5. This again proves the fact that when the groove depth is small, the supported graphene will stay closely with the dented Si surface. When graphene in the suspended region completely separates from Si (lose coupling), the thermal resistance will suddenly jump. At the same time, the repulsive force in the supported area becomes smaller, and the local thermal resistance increases due to the reduced localized pressure. Therefore the graphene will be hanged over the dent gaps and the corresponding thermal resistance increases due to significant reduction in thermal contact area.

CHAPTER 7. CONCLUSIONS AND FUTURE WORK

7.1. Conclusions for dynamic response of graphene to thermal impulse

A fast transient technique was developed to characterize the thermophysical properties of GNRs using MD simulation. A Debye model for two-dimensional GNR was derived for temperature's quantum correction. The specific heat of GNRs was calculated by MD simulation and the results are 1528 J/kg·K and 827 J/kg·K at 692.3 K and 300.6 K. These values are very close to those of graphite, and suggest that the unique 2D structure of graphene has little effect on its ability to store thermal energy. Based on obtained thermal conductivity data at different lengths, the thermal conductivity for infinite length GNRs were calculated at 149 W/m·K (692.3 K) and 317 W/m·K (300.6 K). These values are much smaller than some data reported in literatures for GNRs of similar width. It reflects the fact that the quantum correction of temperature is critical for thermal transport study of graphene. The calculated thermal conductivity is reduced by boundary scattering and other property changes due to the restriction of small width (1.99 nm). Non-Fourier heat conduction was observed to be significant in 14.9 nm long GNR and wavelike heat flux is observed in transient heating of GNR system. A thermal wave was only observed for the ZA phonon, suggesting that thermal transport by ZA phonons is faster than that by the TA and LA modes. It is conclusive that the ZA mode is dominant for GNR's thermal conduction. Also the energy transfer among ZA phonons is much faster than that between ZA and LA/TA phonons. The observed

propagation speed ($c = 4.6$ km/s) of the thermal wave follows the relation of $c = v_g / \sqrt{2}$ where v_g is the ZA phonon group velocity (7.0 km/s from our calculation).

7.2. Conclusions for thermal transport in bended graphene nanoribbons

Phonon thermal transport in bended GNR systems was studied systematically and three new phenomena were observed. In the 3D right-angle bended GNR systems, energy separation emerged between the in-plane and out-of-plane phonon modes. To further exploit the energy separation phenomenon, flat GNR systems of different lengths: 25.0 nm, 50.1 nm, 75.0 nm and 100.0 nm with fixed width 2.0 nm were built, and energy separations were observed in all structures after a steady state heat flux flow was added. Strong thermal transport capability of the ZM phonons was proved to be the reason for such energy separation. The observed distance for energy separation was ~50 nm for flat GNR systems. An energy barrier was observed in the right-angle bended GNR, which was caused mainly by two factors: one is the phonon energy scattering and reflection at the bending structure, and the other one is that the compressive strain in the bending area that could increase the local phonon scattering and reduce thermal conductivity. The bending resistance (R) for the 2.0×25.0 nm² right-angle bended GNR was calculated at 1.48×10^{-11} and 3.93×10^{-11} K·m²/W before and after quantum correction. When the phonon packages passed through the bending structure, instead of keeping the vibrating directions, they preserved their vibrating modes, i.e. the ZM phonon branch will always vibrate in the out-of-plane direction, and TM and LM

phonon branches will always vibrate perpendicular and parallel to the phonon propagating direction. No obvious bending resistance was observed in the 135° bended GNR structure.

7.3. Conclusions for phonon energy inversion in graphene

Energy inversion in a GNR system during transient thermal transport was observed. The observed energy inversion requires localized phonon excitation (single mode or mode-wide) and can hold for about 50 ps. There are two main factors that contribute to the energy inversion in GNR. One is the much higher thermal conductivity of FM phonons than that of TM/LM phonons. The other one is that the energy coupling between FM and TM/LM phonons is not constant against their energy level: the coupling becomes stronger when the phonon energy is higher. Under the influence of a moving or static localized heat source, the FM phonons conduct heat much faster than the LM/TM phonons. Consequently thermal energy continuously transfers from LM/TM phonons to FM phonons in the heat source region while in the cold region the energy flow-back is much slower. We conducted prediction of energy inversion and the results agreed very well with the MD observation. With an increasing layer number of graphene, the energy inversion was weakened due to a decreasing thermal conductivity of FM phonons. Our observation points out a novel way for temporal energy storage in FM phonons, and energy conversion from LM/TM to FM mode (energy separation and isolation).

7.4. Conclusions for co-existing heat currents in opposite directions in GNRs

In this work, phonon thermal transport in GNR was investigated under different FM and TM/LM phonon heating and cooling. It was observed that over a very long distance (up to 100 nm), unprecedented bi-directional heat currents emerged: FM and TM+LM phonons carried heat currents in opposite directions at the same time. The very weak energy coupling between FM and TM+LM phonons played a critical role in this bi-directional heat conduction. Both positive and negative κ_{app} were observed under steady state bi-directional heat conduction in GNR. The calculated negative κ_{app} does not violate the second law of thermodynamics because for each phonon mode, the heat current still flows from higher energy level to lower one, meaning its thermal conductivity is still positive. The negative κ_{app} originated from two factors: the very weak coupling between the FM and LM+TM phonons, and the much larger thermal conductivity sustained by FM phonons than that by LM+TM phonons. It was proved that thermal equilibrium was established for each phonon mode during steady state heat conduction. The mode-wide energy difference became greater when the heat current was dominated by FM phonons. The topology of κ_{app} for GNR was calculated with different μ values. When μ was within the range 1.05 to 1.38, κ_{app} was negative. Zero and infinite κ_{app} values were also observed during the steady state bi-directional heat transfer in GNR. The length effect on the bi-directional heat conduction was also explored and the results showed that if the length of the GNR increases, κ_{app} will also increase while its sign remains unchanged.

7.5. Conclusions for thermal transport across graphene-silicon interface

In this work, the thermal transport across graphene-silicon interface is studied using MD simulations. A pump-probe method focusing on the transient thermal transport processes is developed to characterize the interfacial thermal resistances. By segmentally fitting the energy relaxation profiles of the supported GNR, it is proved that thermal resistance values between graphene and silicon substrate do not have substantially changes with temperature. An averaged thermal resistance value is accurate enough to be used in the overall fitting process. Thermal rectification across the graphene-silicon interface is studied and the thermal resistance values do not have substantial changes under different heating directions. Effects of dimensions on the interfacial thermal resistances are investigated and it is found that the thermal resistance values increase with length. Also, due to the difference between effective and projected heating areas, the square-shaped supported GNRs have larger thermal resistance values than the rectangle-shaped GNRs. At last, the effects of surface roughness on the interfacial thermal resistances are studied. It is proved that the thermal resistance decreases at small dent depth and converges to a larger value when the dent depth is larger than the cut-off distance of the LJ potential.

REFERENCES

- [1] A.K. Geim, K.S. Novoselov, *Nat Mater*, 6 (2007) 183-191.
- [2] Y.W. Son, M.L. Cohen, S.G. Louie, *Nature*, 444 (2006) 347-349.
- [3] K.S. Novoselov, A.K. Geim, S.V. Morozov, D. Jiang, Y. Zhang, S.V. Dubonos, I.V. Grigorieva, A.A. Firsov, *Science*, 306 (2004) 666-669.
- [4] J.S. Bunch, A.M. van der Zande, S.S. Verbridge, I.W. Frank, D.M. Tanenbaum, J.M. Parpia, H.G. Craighead, P.L. McEuen, *Science*, 315 (2007) 490-493.
- [5] Y. Yue, J. Zhang, X. Wang, *Small*, (2011).
- [6] T. Kawai, M. Hino, T. Ebisawa, S. Tasaki, D. Yamazaki, Y. Otake, G. Shirouzu, N. Achiwa, *Physica B*, 276 (2000) 977-978.
- [7] A. Rycerz, J. Tworzydło, C.W.J. Beenakker, *Nat Phys*, 3 (2007) 172-175.
- [8] K. Wakabayashi, Y. Takane, M. Sigrist, *Phys Rev Lett*, 99 (2007) 10-15.
- [9] T. Yamamoto, S. Watanabe, K. Watanabe, *Phys Rev Lett*, 92 (2004) -.
- [10] Z.X. Guo, D. Zhang, X.G. Gong, *Appl Phys Lett*, 95 (2009) -.
- [11] A.A. Balandin, S. Ghosh, W.Z. Bao, I. Calizo, D. Teweldebrhan, F. Miao, C.N. Lau, *Nano Lett*, 8 (2008) 902-907.
- [12] S. Ghosh, I. Calizo, D. Teweldebrhan, E.P. Pokatilov, D.L. Nika, A.A. Balandin, W. Bao, F. Miao, C.N. Lau, *Appl Phys Lett*, 92 (2008) -.
- [13] T. Ouyang, Y.P. Chen, K.K. Yang, J.X. Zhong, *Epl*, 88 (2009) -.
- [14] D.L. Nika, E.P. Pokatilov, A.S. Askerov, A.A. Balandin, *Physical Review B*, 79 (2009) -.
- [15] B.D. Kong, S. Paul, M.B. Nardelli, K.W. Kim, *Physical Review B*, 80 (2009) -.

- [16] J.N. Hu, X.L. Ruan, Y.P. Chen, *Nano Lett*, 9 (2009) 2730-2735.
- [17] N. Mingo, D.A. Broido, *Phys Rev Lett*, 95 (2005) 096105.
- [18] Y. Xu, X.B. Chen, B.L. Gu, W.H. Duan, *Appl Phys Lett*, 95 (2009) -.
- [19] D.L. Nika, E.P. Pokatilov, A.S. Askerov, A.A. Balandin, *Physical Review B*, 79 (2009) 155413.
- [20] D.L. Nika, S. Ghosh, E.P. Pokatilov, A.A. Balandin, *Appl Phys Lett*, 94 (2009) 203103.
- [21] P.G. Klemens, *Int J Thermophys*, 22 (2001) 265-275.
- [22] P.G. Klemens, *Journal of Wide Bandgap Materials*, 7 (2000) 332-339.
- [23] K. Saito, J. Nakamura, A. Natori, *Physical Review B*, 76 (2007) 115409.
- [24] J.H. Seol, I. Jo, A.L. Moore, L. Lindsay, Z.H. Aitken, M.T. Pettes, X.S. Li, Z. Yao, R. Huang, D. Broido, N. Mingo, R.S. Ruoff, L. Shi, *Science*, 328 (2010) 213-216.
- [25] R. Prasher, *Science*, 328 (2010) 185-186.
- [26] L. Lindsay, D.A. Broido, N. Mingo, *Physical Review B*, 82 (2010) 115427.
- [27] L. Lindsay, D.A. Broido, N. Mingo, *Physical Review B*, 83 (2011) 235428.
- [28] J.C. Zhang, X.P. Huang, Y.N. Yue, J.M. Wang, X.W. Wang, *Physical Review B*, 84 (2011) 235416.
- [29] D.W. Brenner, O.A. Shenderova, J.A. Harrison, S.J. Stuart, B. Ni, S.B. Sinnott, *J Phys-Condens Mat*, 14 (2002) 783-802.
- [30] P.K. Schelling, S.R. Phillpot, P. Keblinski, *Physical Review B*, 65 (2002) -.
- [31] S. Berber, Y.K. Kwon, D. Tomanek, *Phys Rev Lett*, 84 (2000) 4613-4616.

- [32] J.Q. Guo, X.W. Wang, D.B. Geohegan, G. Eres, *Functional Materials Letters*, 1 (2008) 71-76.
- [33] J.Q. Guo, X.W. Wang, D.B. Geohegan, G. Eres, C. Vincent, *J Appl Phys*, 103 (2008) -.
- [34] B.W. Dodson, *Physical Review B*, 35 (1987) 2795-2798.
- [35] J. Tersoff, *Phys Rev Lett*, 61 (1988) 2879.
- [36] N. Yang, G. Zhang, B.W. Li, *Nano Lett*, 8 (2008) 276-280.
- [37] X.P. Huang, X.L. Huai, S.Q. Liang, X.W. Wang, *J Phys D Appl Phys*, 42 (2009) -.
- [38] F.P. Incropera, *Fundamentals of heat and mass transfer*, 6th ed., John Wiley, Hoboken, NJ, 2007.
- [39] E. Munoz, J.X. Lu, B.I. Yakobson, *Nano Lett*, 10 (2010) 1652-1656.
- [40] J.C. Lambropoulos, M.R. Jolly, C.A. Amsden, S.E. Gilman, M.J. Sinicropi, D. Diakomihalis, S.D. Jacobs, *J Appl Phys*, 66 (1989) 4230-4242.
- [41] S.R. Mirmira, L.S. Fletcher, *Journal of Thermophysics and Heat Transfer*, 12 (1998) 121-131.
- [42] D.G. Cahill, *Microscale Thermophysical Engineering*, 1 (1997) 85-109.
- [43] J.M. Ziman, *Philosophical Magazine*, 5 (1960) 757-758.
- [44] S. Volz, J.B. Saulnier, M. Lallemand, B. Perrin, P. Depondt, M. Mareschal, *Physical Review B*, 54 (1996) 340-347.
- [45] M.G. Holland, *Phys Rev*, 132 (1963) 2461-&.
- [46] A. Majumdar, *Journal of Heat Transfer-Transactions of the Asme*, 115 (1993) 7-16.
- [47] W. Evans, *Appl Phys Lett*, 96 (2010) 203112.

- [48] D.D. Joseph, L. Preziosi, *Reviews of Modern Physics*, 61 (1989) 41-73.
- [49] M.N. Ozisik, D.Y. Tzou, *Journal of Heat Transfer-Transactions of the Asme*, 116 (1994) 526-535.
- [50] P. Vernotte, *Comptes Rendus Hebdomadaires Des Seances De L Academie Des Sciences*, 246 (1958) 3154-3155.
- [51] C. Cattaneo, *Comptes Rendus Hebdomadaires Des Seances De L Academie Des Sciences*, 247 (1958) 431-433.
- [52] D.W. Tang, N. Araki, *Materials Science and Engineering a-Structural Materials Properties Microstructure and Processing*, 292 (2000) 173-178.
- [53] A.A. Balandin, D.L. Nika, S. Ghosh, E.P. Pokatilov, *Appl Phys Lett*, 94 (2009).
- [54] L. Lindsay, D.A. Broido, N. Mingo, *Physical Review B*, 83 (2011).
- [55] L. Lindsay, D.A. Broido, N. Mingo, *Phys Rev B*, 82 (2010).
- [56] B.W. Li, Z.Q. Wang, R.G. Xie, C.T. Bui, D. Liu, X.X. Ni, J.T.L. Thong, *Nano Lett*, 11 (2011) 113-118.
- [57] L. Shi, J.H. Seol, I. Jo, A.L. Moore, L. Lindsay, Z.H. Aitken, M.T. Pettes, X.S. Li, Z. Yao, R. Huang, D. Broido, N. Mingo, R.S. Ruoff, *Science*, 328 (2010) 213-216.
- [58] L. Wirtz, A. Rubio, *Solid State Commun*, 131 (2004) 141-152.
- [59] O. Dubay, G. Kresse, *Physical Review B*, 67 (2003) 035401.
- [60] J. Maultzsch, S. Reich, C. Thomsen, H. Requardt, P. Ordejon, *Phys Rev Lett*, 92 (2004).
- [61] M. Chester, *Phys Rev*, 131 (1963) 2013.

- [62] X. Xu, X. Wang, *Applied Physics a-Materials Science & Processing*, 73 (2001) 107-114.
- [63] J. Tersoff, *Phys Rev Lett*, 61 (1988) 2879-2882.
- [64] A.A. Balandin, *Nat Mater*, 10 (2011) 569-581.
- [65] W.W. Cai, A.L. Moore, Y.W. Zhu, X.S. Li, S.S. Chen, L. Shi, R.S. Ruoff, *Nano Lett*, 10 (2010) 1645-1651.
- [66] W.J. Evans, L. Hu, P. Keblinski, *Appl Phys Lett*, 96 (2010) 203112.
- [67] S. Ghosh, I. Calizo, D. Teweldebrhan, E.P. Pokatilov, D.L. Nika, A.A. Balandin, W. Bao, F. Miao, C.N. Lau, *Appl Phys Lett*, 92 (2008) 151911.
- [68] P. Kim, L. Shi, A. Majumdar, P.L. McEuen, *Phys Rev Lett*, 87 (2001) 215502.
- [69] J. Hone, M. Whitney, C. Piskoti, A. Zettl, *Physical Review B*, 59 (1999) R2514-R2516.
- [70] A. Cao, *J Appl Phys*, 111 (2012) 083528.
- [71] Z.X. Guo, D. Zhang, X.G. Gong, *Appl Phys Lett*, 95 (2009) 163103.
- [72] J.N. Hu, S. Schiffl, A. Vallabhaneni, X.L. Ruan, Y.P. Chen, *Appl Phys Lett*, 97 (2010) 133107.
- [73] D.K. Efetov, P. Kim, *Phys Rev Lett*, 105 (2010) 256805.
- [74] J.U. Lee, D. Yoon, H. Kim, S.W. Lee, H. Cheong, *Physical Review B*, 83 (2011) 081419.
- [75] J.N. Hu, X.L. Ruan, Z.G. Jiang, Y.P. Chen, *Aip Conf Proc*, 1173 (2009) 135-138 398.
- [76] Y.N. Yue, J.C. Zhang, X.W. Wang, *Small*, 7 (2011) 3324-3333.

- [77] Z. Chen, W. Jang, W. Bao, C.N. Lau, C. Dames, *Appl Phys Lett*, 95 (2009) 161910.
- [78] X.B. Li, K. Maute, M.L. Dunn, R.G. Yang, *Physical Review B*, 81 (2010) 245318.
- [79] S. Bhowmick, V.B. Shenoy, *J Chem Phys*, 125 (2006) 164513.
- [80] C. Liang, K. Satish, *J Appl Phys*, 112 (2012) 043502.
- [81] W.G. Hoover, *Phys Rev A*, 31 (1985) 1695-1697.
- [82] S. Nose, *Mol Phys*, 52 (1984) 255-268.
- [83] P. Hunenberger, *Adv Polym Sci*, 173 (2005) 105-147.
- [84] J.N. Hu, Y. Wang, A. Vallabhaneni, X.L. Ruan, Y.P. Chen, *Appl Phys Lett*, 99 (2011) 113101.
- [85] B.W. Li, L. Wang, G. Casati, *Appl Phys Lett*, 88 (2006) 143501.
- [86] E. Pereira, *Phys Rev E*, 82 (2010) 040101.
- [87] N. Yang, N. Li, L. Wang, B. Li, *Physical Review B*, 76 (2007) 020301.
- [88] D.H. He, S. Buyukdagli, B. Hu, *Physical Review B*, 80 (2009) 104302.
- [89] J. Zhang, X. Wang, H. Xie, *Phys Lett A*, 377 (2013) 721-726.
- [90] G. Eda, G. Fanchini, M. Chhowalla, *Nat Nanotechnol*, 3 (2008) 270-274.
- [91] R.S. Pantelic, J.W. Suk, C.W. Magnuson, J.C. Meyer, P. Wachsmuth, U. Kaiser, R.S. Ruoff, H. Stahlberg, *J Struct Biol*, 174 (2011) 234-238.
- [92] J.Q. Broughton, G.H. Gilmer, *J Chem Phys*, 79 (1983) 5095-5104.
- [93] D.K. Christen, G.L. Pollack, *Physical Review B*, 12 (1975) 3380-3391.
- [94] H. Kaburaki, J. Li, S. Yip, H. Kimizuka, *J Appl Phys*, 102 (2007) 043514.
- [95] K.V. Tretiakov, S. Scandolo, *J Chem Phys*, 120 (2004) 3765-3769.
- [96] I.J. Gupta, S.K. Trikha, *Phys Status Solidi B*, 84 (1977) K95-K99.

- [97] G.K. White, S.B. Woods, *Nature*, 177 (1956) 851-852.
- [98] Z.R. Zhong, X.W. Wang, J. Xu, *Numer Heat Tr B-Fund*, 46 (2004) 429-446.
- [99] J. Shiomi, S. Maruyama, *Physical Review B*, 73 (2006).
- [100] A.J.C. Ladd, B. Moran, W.G. Hoover, *Physical Review B*, 34 (1986) 5058-5064.
- [101] A.J.H. McGaughey, M. Kaviani, *Physical Review B*, 69 (2004) 094303.
- [102] J.E. Turney, E.S. Landry, A.J.H. McGaughey, C.H. Amon, *Physical Review B*, 79 (2009) 064301.
- [103] A.S. Henry, G. Chen, *J Comput Theor Nanos*, 5 (2008) 141-152.
- [104] N. de Koker, *Phys Rev Lett*, 103 (2009) 125902.
- [105] J. Shiomi, S. Maruyama, *Physical Review B*, 73 (2006) 205420.
- [106] B. Qiu, H. Bao, G.Q. Zhang, Y. Wu, X.L. Ruan, *Comp Mater Sci*, 53 (2012) 278-285.
- [107] J.E. Turney, E.S. Landry, A.J.H. McGaughey, C.H. Amon, *Physical Review B*, 79 (2009).
- [108] H.J. Zhang, G. Lee, A.F. Fonseca, T.L. Borders, K. Cho, *J Nanomater*, (2010).
- [109] S. Ghosh, I. Calizo, D. Teweldebrhan, E.P. Pokatilov, D.L. Nika, A.A. Balandin, W. Bao, F. Miao, C.N. Lau, *Appl Phys Lett*, 92 (2008).
- [110] B. Qiu, X.L. Ruan, *Appl Phys Lett*, 100 (2012).
- [111] Z. Chen, W. Jang, W. Bao, C.N. Lau, C. Dames, *Appl Phys Lett*, 95 (2009).
- [112] Z.Y. Wei, Z.H. Ni, K.D. Bi, M.H. Chen, Y.F. Chen, *Phys Lett A*, 375 (2011) 1195-1199.
- [113] A. Venugopal, L. Colombo, E.M. Vogel, *Appl Phys Lett*, 96 (2010).

- [114] M. Halbwx, T. Sarnet, P. Delaporte, A. Sentis, H. Etienne, F. Torregrosa, V. Vervisch, I. Perichaud, S. Martinuzzi, *Thin Solid Films*, 516 (2008) 6791-6795.
- [115] R.I. Bahar, D. Hammerstrom, J. Harlow, W.H. Joyner, C. Lau, D. Marculescu, A. Orailoglu, M. Pedram, *Computer*, 40 (2007) 25-+.
- [116] C.M. Hu, *Nanotechnology*, 10 (1999) 113-116.
- [117] L.A. Jauregui, Y.N. Yue, A.N. Sidorov, J.N. Hu, Q.K. Yu, G. Lopez, R. Jalilian, D.K. Benjamin, D.A. Delk, W. Wu, Z.H. Liu, X.W. Wang, Z.G. Jiang, X.L. Ruan, J.M. Bao, S.S. Pei, Y.P. Chen, *Ecs Transactions*, 28 (2010) 73-83.
- [118] L. Lindsay, D.A. Broido, *Physical Review B*, 81 (2010).
- [119] T. Hertel, R.E. Walkup, P. Avouris, *Physical Review B*, 58 (1998) 13870-13873.
- [120] J.L. Xiao, S. Dunham, P. Liu, Y.W. Zhang, C. Kocabas, L. Moh, Y.G. Huang, K.C. Hwang, C. Lu, W. Huang, J.A. Rogers, *Nano Lett*, 9 (2009) 4311-4319.
- [121] Z.Y. Ong, E. Pop, *Physical Review B*, 81 (2010).
- [122] S. Plimpton, *J Comput Phys*, 117 (1995) 1-19.
- [123] A.J. Schmidt, X.Y. Chen, G. Chen, *Rev Sci Instrum*, 79 (2008).
- [124] B.C. Gundrum, D.G. Cahill, R.S. Averback, *Physical Review B*, 72 (2005).
- [125] Z.P. Xu, M.J. Buehler, *J Phys-Condens Mat*, 24 (2012).
- [126] J.C. Zhang, X.W. Wang, H.Q. Xie, *Phys Lett A*, 377 (2013) 721-726.
- [127] N. Yang, G. Zhang, B.W. Li, *Appl Phys Lett*, 95 (2009).
- [128] J. Cheh, H. Zhao, *J Stat Mech-Theory E*, (2012).
- [129] G. Zhang, H.S. Zhang, *Nanoscale*, 3 (2011) 4604-4607.

- [130] K.G.S.H. Gunawardana, K. Mullen, J.N. Hu, Y.P. Chen, X.L. Ruan, *Physical Review B*, 85 (2012).
- [131] C.W. Chang, D. Okawa, H. Garcia, A. Majumdar, A. Zettl, *Phys Rev Lett*, 99 (2007).
- [132] S. Maruyama, *Physica B*, 323 (2002) 193-195.
- [133] N. Yang, G. Zhang, B.W. Li, *Nano Today*, 5 (2010) 85-90.
- [134] G. Zhang, B.W. Li, *J Chem Phys*, 123 (2005).
- [135] J. Chen, G. Zhang, B.W. Li, *Nanoscale*, 5 (2013) 532-536.
- [136] Z.X. Guo, D. Zhang, X.G. Gong, *Appl Phys Lett*, 95 (2009).
- [137] D.L. Nika, A.S. Askerov, A.A. Balandin, *Nano Lett*, 12 (2012) 3238-3244.
- [138] J.C. Zhang, X.W. Wang, *Nanoscale*, 5 (2013) 734-743.